THEORETICAL AND EXPERIMENTAL ANALYSIS OF MACHINABILITY AND SURFACE INTEGRITY OF BULK METALLIC GLASS IN ULTRA-PRECISION DIAMOND CUTTING

CHAU SAU YEE

PhD

The Hong Kong Polytechnic University

2020

The Hong Kong Polytechnic University

Department of Industrial and Systems Engineering

Theoretical and Experimental Analysis of Machinability and Surface Integrity of Bulk Metallic Glass in Ultra-Precision Diamond Cutting

CHAU SAU YEE

A thesis submitted in partial fulfillment of the requirements for the degree of Doctor of Philosophy

February 2019

CERTIFICATE OF ORIGINALITY

I hereby declare that this thesis is my own work and that, to the best of my knowledge and belief, it reproduces no material previously published or written, nor material that has been accepted for the award of any other degree or diploma, except where due acknowledgement has been made in the text.

_____(Signed)

_____Chau Sau Yee_____(Name of student)

Abstract

Single point diamond turning (SPDT) is a cutting technique which can produce optical-quality components with submicron form accuracy and surface roughness within a few tens of nanometers with the use of mono-crystal diamond tools. The mechanism in ultra-precision cutting is different from conventional cutting as the depth of cut in ultra-precision cutting lies in the sub-micrometric to a few tens of micrometric region, which is smaller than the average grain diameter of the work materials. It is 100 times smaller than the depth of cut used in conventional cutting, so the material behavior plays an important role on the dimensional accuracy and stability of the machined surface. Most previous research on the effect of metallurgical properties on SPDT was mainly focused on crystalline materials, and little attention has been paid to the cutting mechanics and surface generation of diamond turned amorphous metals. Therefore, a systematic study of the machinability and surface integrity in ultra-precision diamond cutting of bulk metallic glasses (BMGs) was been conducted though experimental and theoretical analysis.

The machinability of a material is well-known for being affected by the cutting conditions, cutting tools and material properties. The main contributions of the theoretical and experimental studies described in this report are shown below:

Abstract

(1) The cutting characteristics of BMGs in single point diamond cutting were studied by experimental investigation. The obtained results showed that the machined surface roughness is sensitive to the cutting speed and depth of cut. A finer surface can be obtained by employing a small depth of cut and slow cutting speed in the diamond cutting process. The built-up material formed on the tool edge was observed after diamond cutting BMG, and continuous serrated chips were formed. In contrast with conventional machining of BMG, as reported in the literature, the amorphous microstructure remained unchanged after the diamond turning process.

(2) The shear band morphology has been investigated under various cutting speeds for exploring the effects of cutting speed on the surface generation in the micro-cutting process. This study investigates the formation of multiple shear bands in the micro-cutting of zirconium-based bulk metallic glass in where classic models have not been studied. A series of slip-steps were observed in various cutting directions which were significantly affected by cutting speed. Electron microscopy studies further confirmed the mechanism of the formation of nanocrystals with the formation of shear bands within the primary deformation zone (PDZ) in the micro-cutting process under various cutting speeds.

(3) Experimental and theoretical investigations into chip formation in diamond cutting of BMG were successfully conducted. The generation of twinned-serrated chips

(TSCs) in ultra-precision micro-cutting (UPMC) of BMG was studied. The intrinsic cause was due to BMG exhibiting a strongly adiabatic effect, which was confirmed by a proposed finite element model. A series of UPMC tests have been carried out to verify the results of simulation, revealing the effect of rake angle on the BMG cutting process. The simulation and experimental results of chip formation proved that the adiabatic effect is the key factor leading to serrated chips in the UPMC of BMG. In addition, a comparison of the simulation and experimental results under different tool rake angles showed that the serrated chips and cutting force are sensitive to the rake angle of the tool.

The originality and significance of this study can be summarized as (i) providing a comprehensive understanding of the cutting characteristic in SPDT of BMG; (ii) the mechanism of multiple shear bands formation and propagation in SPDT of BMG is revealed by the experimental analysis; (iii) finite element analysis (FEA) modelling of the chip formation in SPDT of BMG is realized for the first time, revealing the mechanism of generating twinned-serrated chips in SPDT of BMG.

Publication arising from this study

Journal papers

1. **Chau, S.Y.**, To, S., Wu, H., & Sun Z., Twinned-serrated chip formation with minor shear bands in ultra-precision micro-cutting of bulk metallic glasss. The International Journal of Advanced Manufacturing Technology, Vol. 107, pp.4437–4448 (2020).
2. **Chau, S.Y.**, To, S., Wang, H., Yip, W.S., Chan, K.C. & Cheung, C.F. Effect of cutting speed on surface integrity and chip formation in micro-cutting of Zr-based bulk metallic glass. The International Journal of Advanced Manufacturing Technology (Under review).

Conference paper

1. **Chau, S.Y.**, To, S., Chan, K.C. & Cheung, C.F. Cutting characteristics of zirconium based bulk metallic glasses in ultra-precision diamond turning. In Proceedings of the 4th International Conference on Nanomanufacturing, NanoMan 2014, Bremen, Germany

Acknowledgements

I would like to express my special gratitude to my chief supervisor, Prof. Sandy To, for her inspirational and valuable advice on my research. My most sincere thanks are also extended to my co-supervisors Prof. K.C. Chan and Prof. C.F. Cheung for their support and encouragement. I would like to thank Dr. C.Y. Chan for his constant guidance.

I would like to thank Dr. Victor Wang for all the inspiring discussions with him about detail guiding on the data collection method and analysis direction. My thanks also include all the staff in the Advanced Optics Manufacturing Centre (AOMC) and State Key Laboratory in Ultra-precision Machining Technology, The Hong Kong Polytechnic University.

Finally, I would like to send my thanks to my father, mother, sister and friends for their support, understanding, patience, encouragement and love.

Table of contents

Table of contents

Table of contents

Table of contents

List of figures

List of figures

List of figures

List of figures

List of figures

List of tables

List of acronyms

AFM = Atomic force microscopy

BMG = Bulk metallic glass

BUE = Built up edge

CFR = Cutting force ratio

FEA = Finite element analysis

FEM = Finite element modeling

FFT = Fast Fourier transform

HRTEM = High-resolution transmission electron microscopy

MDS = Molecular Dynamics Simulation

PDZ = Primary deformation zone

SAD = Selected area diffraction

SLR = Supercooled liquid region

SEM = Scanning electron microscopy

SPDT = Single point diamond turning

TSCs = Twinned-serrated chips

UPMC = Ultra-precision micro-cutting

XTEM = Cross-sectional transmission electron microscopy

XRD = X-ray diffraction

Chapter 1 Introduction

1.1 Motivation

Ultra-precision diamond cutting can be defined as a cutting technique which produces optical- quality components with submicron form accuracy and surface roughness to within a few tens of nanometers with the use of mono-crystal diamond tools. The technique is based on a high degree of tool profile duplication and relative tool work motion (Taniguchi, 1983). It makes use of a mono-crystalline diamond cutting tool which possesses nano-metric edge sharpness, form reproducibility in the sub-micrometer range and wear resistance. Ultra-precision machining (UPM) technology is commonly used in the manufacture of high tolerance components and parts for particular systems in a number of advanced scientific and aerospace applications. In addition, the demands for high tolerance products has increased in the market, so the demands for UPM technology will be further increased.

The theories for conventional machining cannot be directly applied in the study of ultra-precision machining. The mechanism in ultra-precision cutting is different from conventional cutting as the depth of cut in ultra-precision cutting lies in the sub-micrometric to a few tens of micrometric region which is smaller than the average grain diameter of the work materials. Compared to conventional cutting with a depth of cut

of hundreds of micrometres, the material behavior plays an important role on the dimensional accuracy and stability of the machined surface.

Several earlier studies on the effect of metallurgical properties on the cutting mechanics and surface integrity focused on the shear bands formation, surface generation and micro-cutting force (Lee et al., 2000; Cheung et al., 2003). It has been reported that the crystallographic effects on surface generation in single point diamond turning have been investigated by micro-cutting single crystals (Lee et al., 2000; Liang et al., 1994). The non-random distribution of the crystalline material has significant predictable effects on the surface generation. However, there have been few studies on the cutting mechanics and surface generation of diamond turning amorphous metals. An amorphous metal also known as a metallic glass, and is a metal alloy with a non-ordered atomic structure, so that metallic glasses are non-crystalline metals. The non-crystalline structure leads to stronger mechanical properties because there are no internal boundaries that can create weak regions or break points. As a result, all theories related to dislocation motion in describing atomic behavior are not applicable for metallic glasses.

Metallic glasses are widely applied into different fields in engineering due to outstanding mechanical properties, superior corrosion resistance and excellent biocompatibility (Martienssen and Warlimont, 2005). In addition, the glass nature

provides a supercooled liquid region which leads brittle-to-ductile transition behavior at high temperature during machining (Chen, 1968). The brittle-to-ductile transition behavior means that the plasticity will increase with temperature increase. Therefore, it is important to complete and integrate the study of the cutting mechanics in ultra-precision machining by developing a theory and model for the material removal behavior in ultra-precision diamond cutting of amorphous metals though experimental and physical analysis.

In this research, the machinability in the SPDT of BMG is studied from the viewpoint of surface generation, shear bands and chip formation. In addition, the nanocrystallization of metallic glasses under diamond cutting conditions has been observed by a high-resolution transmission electron microscopy (HRTEM) study. The effect of tool rake angle on chip formation in diamond cutting BMG was explored through an experimental and simulation approach.

1.2 Research objectives

The research aims to investigate the machinability and surface integrity of bulk metallic glass in ultra-precision diamond cutting with the following aims:

i. To study the cutting characteristic of BMGs in ultra-precision diamond turning.

For investigating the cutting characteristic of BMG in SPDT, a series of experiments would be conducted in this study. The effect of machined surface quality, diamond tool wear and the microstructure changes on the bulk metallic glasses in diamond turning under different cutting parameter would be investigated in this study.

ii. To study the shear band morphology and nanocrystallization in diamond cutting of bulk metallic glass.

For understanding the material removal mechanics and crystallographic effect in diamond cutting of BMG, the morphological feature of the primary deformation zone and the effect on the machined surface roughness in the diamond cutting of Zr-based BMG is investigated experimentally through the orthogonal cutting process, and the crystallographic change induced by the micro-cutting process is characterized through a HRTEM study.

iii. To investigate the effect of machining parameters on chip formation and material removal mechanism in diamond cutting of bulk metallic glass.

This study focuses on an experimental and theoretical investigation into chip formation in UPMC of BMG. A series of UPMC tests have been carried out to verify the results of simulation and reveal the effect of rake angle on the cutting process of BMG.

1.3 Organization of the thesis

This report is presented in five chapters. A brief introduction on the motivation and objectives is described in chapter 1. In chapter 2, an in-depth literature review is conducted on the background of BMGs, the deformation behavior of amorphous metals, an overview of ultra-precision machining, and various machining theories with particular emphasis on the machining at SPDT process are addressed.

Chapter 3 reports on the machinability of BMG under various cutting parameters in SPDT. The experimental investigation in term of surface roughness, cutting force, diamond tool wear and the crystallographic effect are given in this chapter.

Chapter 4 reports the morphological features of the PDZ in diamond cutting BMGs. The multi-shear bands and nanocrystals occur in the PDZ which is unusual in cutting crystal material. Further, the effect of cutting speed on shear band formation in diamond cutting BMG is reported in this chapter.

Chapter 5 reports the effect of the tool rake angle on chip formation in diamond cutting of bulk metallic glass. Finite element simulation is used to demonstrate and analyze the chip formation in the diamond cutting of BMG. A comparison of simulation and experimental results under different tool rake angles is reported in this chapter, showing that the serrated chips and cutting force are sensitive to the tool rake angle.

Chapter 6 discusses the conclusions to the research work in this thesis. The

contributions of the work to the existing ultra-precision machining area are discussed in this chapter. In addition, future work on the built-up edge (BUE) formation mechanism is proposed.

Chapter 2 Literature review

Bulk metallic glass is a novel engineering material developed in the last 50 years, and an in-depth review on the material properties of BMG is given in this chapter. The mechanism, theory and shear banding in single point diamond turning is also discussed in this chapter. In addition, reviews on the modelling and simulation of the machining process have conducted. A short summary on existing research gaps is given at the end of the chapter.

2.1 Background of bulk metallic glasses

For a very long time, metallic materials were commonly considered crystalline with atoms regularly arranged in a periodic way. Pol Duwez and his coworkers (1960) firstly discovered a mixture of silicon and gold alloy with an amorphous structure. A rapid solidification processing method was used by Pol Duwez in the discovery of metallic glasses and the cooling rate was about 10^5 – 10^6 K/s. This rapid cooling rate caused the melt to kinetically bypass the crystallization stage through limited atomic mobility, thereby freezing the system into a meta-stable configuration with no long-range order.

To fulfill the requirement of a high cooling rate, the sample had to be extremely thin. At the beginning, the thickness was less than 0.1 mm. To make metallic glasses

more applicable, a larger size was needed which means that the cooling rate is expected to be lower. Metallic glass $Pd_{40}Ni_{40}P_{20}$ with a minimum dimension over 6μm was fabricated by Kui et al. (1984) with a cooling rate of only 1K/s. It has been accepted that metallic glasses with any dimensional size larger than 1mm are called bulk metallic glasses (Suryanarayana and Inoue, 2011). The maximum achievable diameter of the BMGs in the latest fabrication technology is 80mm, the diameter of a Pd-Cu-Ni-P system (Inoue et al., 2011). Although Pd – based BMGs have excellent glass forming ability, the high cost of Pd inhibits wide utilization. A breakthrough was made in the late 80s when Inoue and Masumoto (1989) made a $La_{55}Al_{25}Ni_{20}$ BMG rod, 1.2mm in diameter. In recent decades, more and more BMGs without noble metals have been fabricated, such as Zr – based (Zhang et al., 1991; Peker and Johnson, 1993), La – based (Inoue et al., 1990; Inoue et al., 1993), Mg – based (Inoue et al., 1992), Ni – based (Yi et al., 2000a; Yi et al., 2000b ;Choi et al., 2003), Gd – based (Li et al., 2005), Fe – based (Shen et al., 2002), Ti – based (Kim et al., 2003; He et al., 2002) and Cu – based BMGs (Kim et al., 2002; Kim at al., 2003 ;Wang et al., 2003). A summary of the properties and applications of BMGs is shown in table 1.

A lot of attention has been paid to BMGs due to their outstanding properties compared to the conventional materials, for example, physical properties, corrosion behavior, mechanical behavior and magnetic properties.

For physical properties, it has been well accepted that the densities of BMGs made from rapid cooling processing are about 2% - 3% less than those of their crystalline counterparts (Chen, 1980). The coefficient of thermal expansion of BMGs is usually larger than that of the pure metal on which they are based, except for the Cu – based BMGs (Martienssen and Warlimont, 2005). Because of the disordered structure, the electrical resistivity of BMGs is about two orders of magnitude higher than their crystalline counterparts (Suryanarayana and Inoue, 2011).

The corrosion resistance behavior of BMGs pays an important role in engineering applications, especially when the working environment is hostile, for example, under high temperatures, and in oxidizing and corrosive atmospheres. The corrosion resistance of BMGs is generally better than that of their counterparts. The corrosion behavior is mainly affected by two factors, composition and environment. Among those different types of BMGs, Mg – based BMGs may suffer the most from corrosion while Ti – based and Zr – based BMGs exhibit very high corrosion resistance (Suryanarayana and Inoue 2011).

Due to the amorphous structure, no dislocation will exist in BMGs. As a result, the strength of BMGs is much higher than that of their counterparts. In most cases, the strength of BMGs can exceed 1 GPa and the typical elongation at yielding is around 2%. For $[(Fe_{0.6}Co_{0.4})_{0.75}B_{0.2}Si_{0.05}]_{96}Nb_4$ metallic glass, the yield strength can reach as

high as 4.1 GPa. In contrast, the yield strength of some common materials is much lower, for example, the yield strengths of 300M steel and Ti-6Al-4V are about 1.6GPa and 1GPa respectively (Inoue et al., 2003). However, differing from crystals, BMGs usually exhibit a relatively low ductility.

The magnetic properties of BMGs are important for many industrial applications. One of the most important applications is for transformer core laminations. Recently, magnetic refrigeration has also attracted a lot of attention due to its promising characteristics (Warburg, 1881; Gschneidner, 2005). Gd – based BMGs have already been used for low temperature refrigeration. Current research has focused on investigating the magnetocaloric effect and refrigeration capacity of Fe – based and Gd – based BMGs. Since the Fe – based and Gd – based BMGs consist of a large glass-forming ability and near room temperature magnetocaloric effect which provides a candidate for use as s near room temperature magnetic refrigerant.

The outstanding properties of BMGs mentioned above show that BMGs are the ideal materials to achieve a better performance than that of the conventional materials. These outstanding mechanical properties of BMGs provide great potential for the ultra-precision machining industry, for example, the excellent strength properties in Zr-based BMGs can be used to fabricate precision optical lens mould inserts to enhance the working life.

Table 1 Summarizes the key properties of some common types of BMG summarizes the key properties of some common types of BMGs

BMGs	Properties	Examples
Zr – based BMGs	Excellent mechanical properties such as high strength, large elastic elongation limit and large glass forming ability	$Zr_{63.4}Ni_{16.2}Cu_{15.4}Al_5$ (Strength=1.7GPa, Elastic rate=2%)
La – based BMGs	Low glass transition temperature, high thermal stability, large glass forming ability	$La_{62}Al_{14}(Cu_{5/6}Ag_{1/6})_{14}(Ni_{1/2}Co_{1/2})_{10}$(Glass transition temperature=418K, Supercooled region=73K)
Mg – based BMGs	Good mechanical properties, biocompatibility, biodegradation property, poor corrosion resistance	$Mg_{58}Cu_{28.5}Gd_{11}Ag_{2.5}$(Yield strength=1.7GPa, Hardness=330Hv)
Ni – based BMGs	High wear resistance under rolling – wear conditions, high corrosion resistance and high hardness	$(Ni_8Nb_5)_{99.8}Sb_{0.2}$(Passive in HCl, Hardness=810Hv)
Gd – based BMGs	Large magnetocaloric effect, expensive, large glass forming ability, large coercivity, low Curie temperature	$Gd_{55}Ni_{25}Al_{20}$(Refrigeration capacity=640J/kg under 5T, Curie temperature=78K)
Fe – based BMGs	Brittle, inexpensive, good corrosion resistance, high permeability, low coercivity, small magnetocaloric effect, high Curie temperature	$Fe_{70}B_5C_5Si_3Al_5Ga_2P_{10}$ Glassy ribbon (Refrigeration capacity=74J/kg under 1.5T, Curie temperature=488K
Ti – based BMGs	high hardness, low density, excellent biocompatibility and corrosion resistance	$Ti_{43}Zr_{25}Nb_7Cu_6Be_{19}$(Hardness=420Hv)
Cu – based BMGs	High corrosion resistance and excellent mechanical properties	$(Cu_{0.6}Hf_{0.25}Ti_{0.15})_{90}Nb_{10}$(Passive in acid and chloride-ion-containing solutions, Yield strength=2073MPa)

2.1.1 Deformation behavior of bulk metallic glasses

Bulk metallic glasses have unique superior properties over their crystalline counterparts due to the non-order of the atomic structure. BMGs are stronger because they do not include internal boundaries causing weak regions or break points, as shown in figure 2.1. Therefore, all theories to describe the dislocation motion behavior are inapplicable in BMGs due to the absence of the long-range order of atomic arrangement. Plastic deformation in bulk metallic glasses can be described by the ideas of free volume and shear transformation, proposed by Spaepen (1977) and Argon (1979) based on the atomic motion.

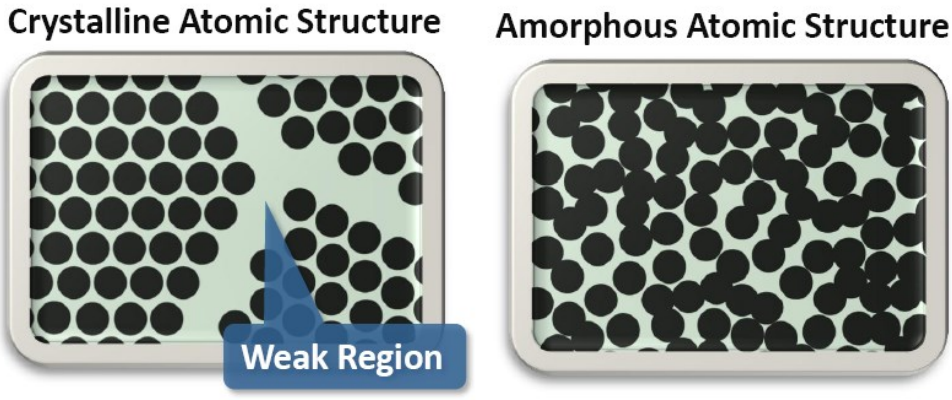

Figure 2.1 Graphical illustrations of the internal boundaries in crystalline and amorphous atomic structures (Daniel, 2019)

2.1.2 Free volume model

In the free volume model (Spaepen, 1977), it is assumed that the macroscopic flow in an amorphous metal occurs as the sum of individual atomic jumps, as illustrated in figure 2.2(a.) The total volume of the metallic glasses is the sum of the atoms of various sizes and “holes”. The free volume concept is related to the “holes”, which play an important role in a diffusive arrangement of the atoms. In order for an atom to jump, an open volume is required in nearest neighbor environment (holes) which can provide sufficient space to contain the jumped atom. So, the feasibility of the atomic jumps is dependent on the size of the atom and adjacent “hole”. In order to create an atom jump, sufficient energy is required to overcome the activation energy. If there is no external stress applied, the number of atoms that jump across the activation barrier is the same in the forward and backward directions, since the energy for a jump is provided by the thermal fluctuation, as shown in Figure 2.2(b). This is the basic microscopic mechanism for diffusion. When an external stress is applied, i.e. a shear stress is applied, the atomic jumps are biased along with the stress applied direction since the activation energy for jumping along the stress direction is lower (shown in figure 2.2(c)), and the direction of the atomic jumps moves forward to the stress direction. This flow can describe the shear flow in amorphous metal.

The free volume can be related to one or more than one atom, when more than one atomic jump from the original site to its nearest neighbor cage occurs, and the accumulated motion will lead to a shear flow (Elliott,1984). Turnbull and Cohen (1964) developed a free volume theory, which can calculate the fraction of potential jump sites. According to Cohen and Turnbull's theory (Turnbull and Cohen ,1964), the probability to find a free volume between υ and υ + dυ is given by:

$$p(v)dv = \frac{\eta}{v_f}\exp\left(-\frac{\eta v^*}{v_f}\right)dv \qquad (2\text{-}1)$$

where η is a geometrical factor between 1 and 0.5; υ_f is the average free volume per atom; and υ^* is the critical value of the free volume which is large enough to accommodate an atom and is able to achieve an atomic jump.

The shear flow rate can be expressed as follows (Spaepen, 1977):

$$\dot{\gamma} = 2\Delta f J exp(-\frac{\lambda v^*}{v_f})\sinh(\frac{\tau\Omega}{2kT})\exp(\frac{v_f}{kT}) \qquad (2\text{-}2)$$

where Δf is the fraction of the sample volume in which potential jump sites can be found, Ω is the atomic volume, k is the Boltzmann constant, J is the Debye frequency (frequency of atomic vibration), T is the absolute temperature, ΔG^m is the activation energy, and τ is the applied stress. The excess free volume can be created by the external shear stress (τ) that squeezes an atom with the effective hard-sphere size of the atom (υ^*), into an adjacent "hole" which was a smaller volume (υ). When the applied stress

provides energy higher than the activation energy (ΔG^m), motion can occur. The dilatation and decreases the viscosity in the shear band are expected due to the larger amount of free volume induced by the shear stress, which leads to strain softening and strong shear localization. The free volume concept has been further verified by the observation by Dehey and his coworkers (Dehey et. al., 1997). A large strain softening in $Pd_{40}Ni_{40}P_{20}$ has been observed under the deformation below its glass transition temperature. Dehey and his coworkers applied the differential scanning calorimetry (DSC) technique to measure the free volume, and the measurement revealed that the strain softening is caused by the creation of additional free volume during deformation.

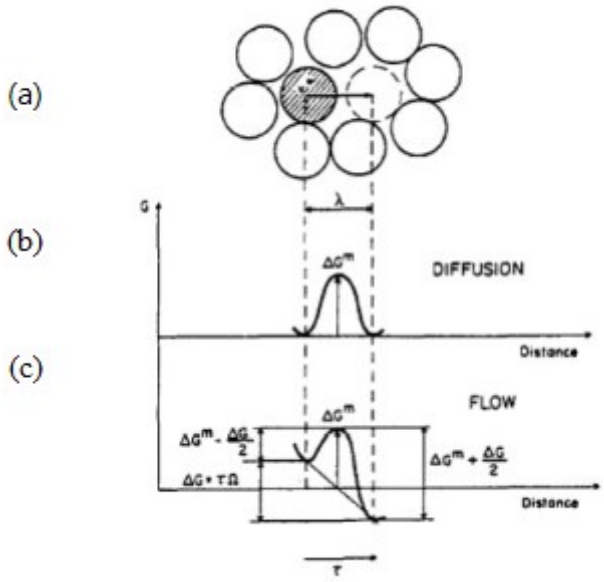

Figure 2.2 Illustration of (a)the creation of free volume by individual atomic jump; (b) the activation energy for atoms to jump forward and backward are provided by the thermal fluctuation; (c) the activation energy for atoms to jump along stress direction with by applying external shear stress (Spaepen, 1977)

2.1.3 Shear transformation model

In 1979, Argon proposed another model to describe the plastic deformation mechanism of metallic glasses. This is based on an atomic-analog bubble-raft model, which explains the shear transformation as the spontaneous and cooperative reorganization of a local cluster of randomly close-packed atoms, as illustrated in figure 2.3. The shear transformation zone is a local cluster of atoms that undergoes an inelastic shear distortion from a low activated configuration to a higher activated energy configuration, hence the stress and strain can be redistribution around the shear transformation zone (Argon, 1979). According to the model, local shear transformation can lead the strain softening due to the local dilatation by the shear transformation.

The quantitative expression for the strain rate, according to the theory is as follow:

$$\dot{\gamma} = \alpha_0 v_0 \gamma_0 \exp\left(-\frac{\Delta F_0}{kT}\right) \sinh\left(\frac{\tau \gamma_0 \Omega_0}{kT}\right) \tag{2.3}$$

where α_0 is the volume fraction of potential shear transformation zones, v_0 is the natural frequency of the shear transformation zones, γ_0 and Ω_0 are the shear strains and the volume of an individual shear transformation zone, ΔF_0 is the activation barrier for the shear transformation zone and it can expressed as:

$$\Delta F_0 = \left[\frac{7-5v}{30(1-v)} + \frac{2(1+v)}{9(1-v)}\beta^2 + \frac{1}{2\gamma_0}\frac{\tau_0}{\mu(T)}\right]\mu(T)\gamma_0^2\Omega_0 \tag{2-4}$$

where $\mu(T)$ is the temperature-dependent shear modulus, v is Poisson's ratio of the glass, τ_0 is the shear resistance of a shear transformation zone, β is the dilatancy factor.

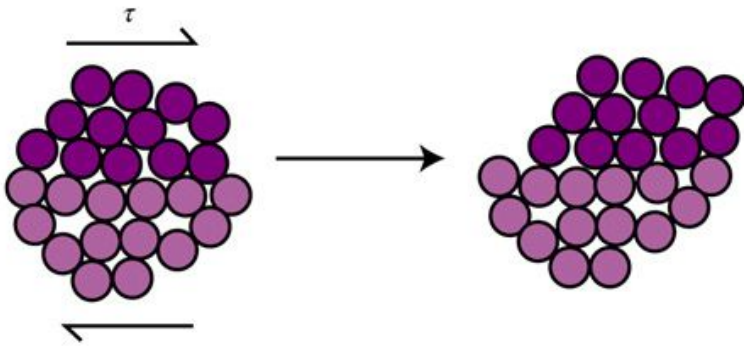

Figure 2.3 Graphical illustration on deformation mechanism in shear transformation zone

2.1.4 Strain rate and temperature effect on deformation behavior

Generally, the deformation of BMGs can be divided into two different modes, homogeneous and inhomogeneous deformation (Spaepen, 1977). Inhomogeneous deformation occurs at high stresses and low temperatures, where the strain localizes in multiple shear bands. On the contrary, homogeneous deformation usually takes place at low stresses and low temperatures within the glass transition temperature (T_g) and the onset temperature of crystallization (T_x), especially in the supercooled liquid region (SLR). In these conditions, the deformation of BMGs often behaves in a viscous manner and exhibits significant plasticity under external loading. More researchers focus on

this homogeneous deformation characteristic because it enables net shaping and the forming of complex-shaped properties for BMGs (Nieh and Wadsworth, 2006). In the present study, a Zr-based BMG was chosen for the investigation of deformation behavior in the supercooled liquid region so as to explore the deformation mechanism of BMG in the SLR. Lu and his coworkers (2003) investigated the effect of temperature and strain rate on the uniaxial stress-strain behavior of $Zr_{41.2}Ti_{13.8}Cu1_{2.5}Ni_{10}Be_{22}$ bulk metallic glass. The results of the deformation behavior of the Zr-based BMG is highly related to the strain rate and working temperature (shown in figure 2.4). The yield stress in uniaxial compression testing is reduced significantly when the working temperature rises to the range between glass transition temperature and crystallization temperature.

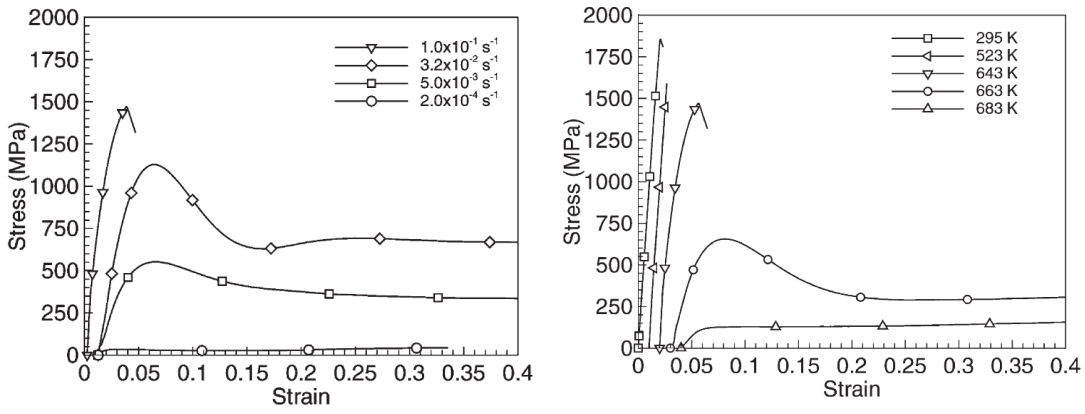

(a) (b)

Figure 2.4 Effect of (a) the temperature on the uniaxial stress-strain behavior under constant strain rate at $1x10^{-1}$ s^{-1}; (b) the strain rate on the uniaxial stress-strain behavior at transition temperature (643K) for $Zr_{41.2}Ti_{13.8}Cu1_{2.5}Ni_{10}Be_{22.5}$

2.1.5 Machining amorphous metal

Ueda et al (1992) investigated the chip formation mechanism in the micro-cutting of a $Fe_{78}B_{13}Si_9$ amorphous metal through SEM observation and rigid-plastic finite element modeling (FEM) simulation. The homogenous deformation structure was confirmed by the existence of typical lamellar structure chips during the micro-cutting of a $Fe_{78}B_{13}Si_9$ amorphous metal, and the lamella spacing was increased proportionally to the increase depth of cut. However, the study did not investigate the surface generated during the micro-cutting of an amorphous metal.

Bakkal (2004c) used a near-infrared spectrometer to capture the light emission from the tool-chip interfaces during machining $Zr_{41.25}Ti_{13.75}Cu_{12.5}Be_{22.5}Ni_{10}$ BMG. The light emission is associated with the adiabatic flash temperatures in the range of 2400K-2700K. The BMG chips were oxidized and crystalized in the outside layer during high speed cutting due to the light emission during machining. It can be avoided by low speed cutting.

The influences of tool material, nose radius, depth of cut and cutting speed on the cutting characteristics of the $Zr_{65}Cu_{15}Ni_{10}Al_{10}$ and $Pd_{40}Cu_{30}Ni_{10}P_{20}$ BMGs were studied by Fujita et al. (2005). The study showed that the principal cutting force of BMGs is due to the cutting speed and is independent of the material's strength. The surface

roughness achievement of both Zr-based and Pd-BMGs was about 0.2 μm (shown in figure 2.5).

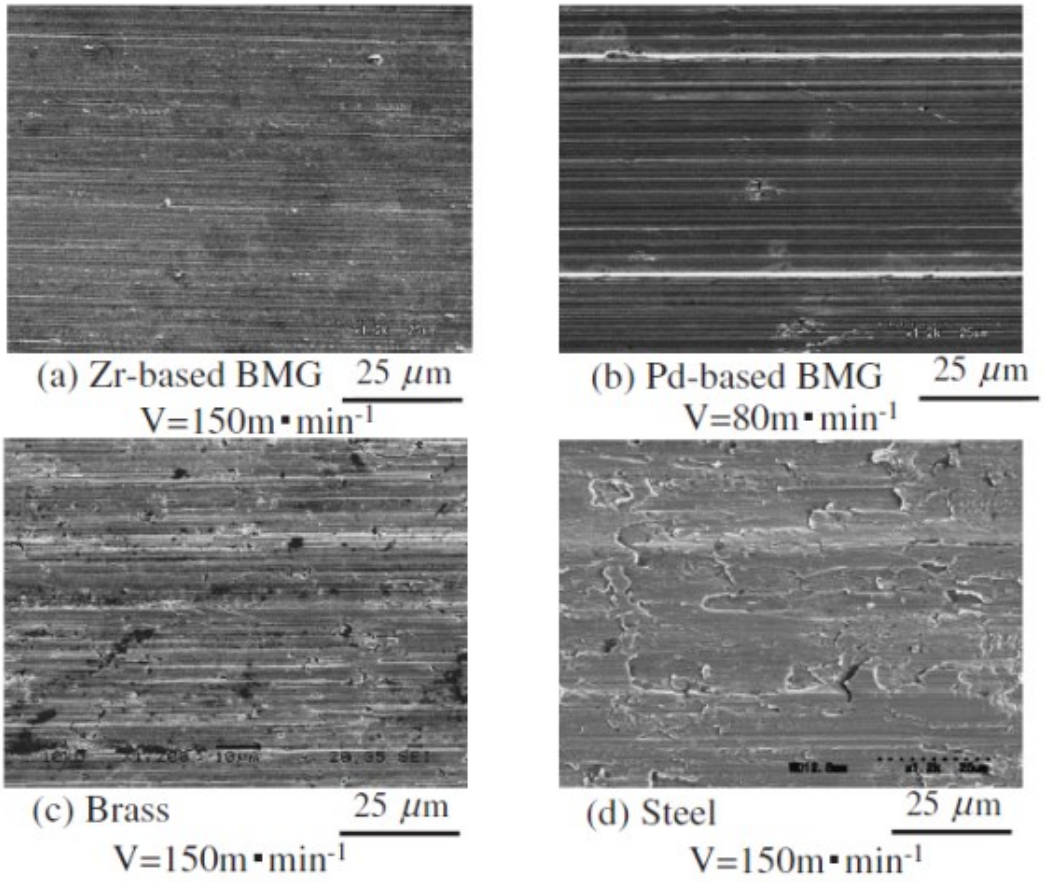

Figure 2.5 Micrographs of the morphology of the machine surface of the BMGs and crystalline alloys using cermet tool tip (Fujita et al., 2005)

2.2 Background of ultra-precision machining

Ultra-precision machining has a higher achieved tolerance compared with the traditional conventional and precision machining (shown in figure 2.6) (Trent and Wright, 2000). The technique is based on a high degree of tool profile duplication and

relative tool work motion (Taniguchi, 1983). Ultra-precision machining technology is commonly used in the manufacture of high tolerance components and parts for various systems in a number of advanced scientific and aerospace applications. In addition, the demands for high tolerance products are increasing in the market, so the demands for UPM technology will also increase.

Single Point Diamond Turning was firstly introduced in the 1960s and is one of the key technologies in the category of ultra-precision machining for super finished components. It makes use of a mono-crystalline diamond cutting tool which possesses nano-metric edge sharpness, form reproducibility in the sub-micrometer range and wear resistance. Compared to conventional machining processes, the depth of cut in SPDT is in the range of micrometers to sub-micrometers. This enables SPDT technology to produce components which can achieve a micrometre to sub-micrometre form accuracy and a nanometer range surface roughness. A comparison of conventional and ultra-precision machining is given in table 2 (Cheung et al., 2003). It can be seen that the machining accuracy of UPM is about 100 times better than that of conventional machining, and the surface roughness is about 1000 times smaller.

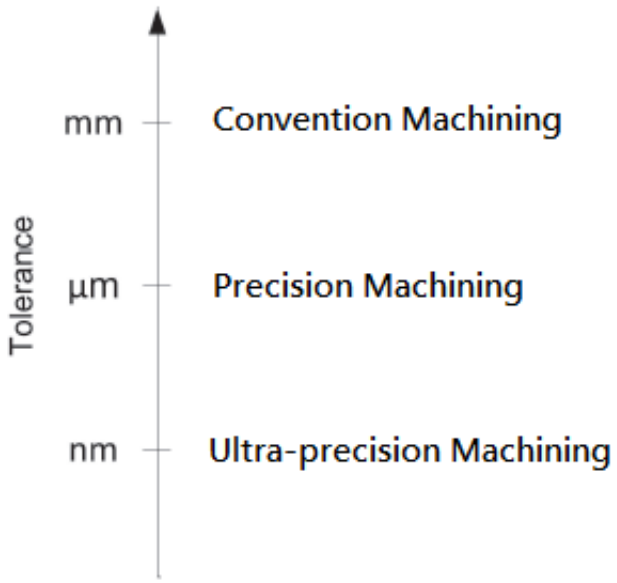

Figure 2.6 Dimensional tolerance for three groups of machining processes

Table 2 Comparison between conventional and ultra-precision machining

Type of process		Conventional machining		Ultra-precision machining	
		Rough cut	Finish cut	Rough cut	Finish cut
Cutting conditions	Feed rate (mm/rev)	0.1-1	0.01-0.05	0.01-0.05	0.005-0.001
	Spindle speed(r/min)	100-300	200-300	1000-2000	2000-3000
	Depth of cut	0.1 mm-1 mm	0.01 mm-0.1 mm	10 μm-50 μm	1μm-5 μm
	Tooling	High speed steel tool Carbide tool Ceramic tool Industrial diamond tool		Single crystal diamond tool Industrial diamond tool	
Machining part	Roughness	10 μm-100 μm	1 μm-10 μm	0.02 μm-0.03 μm (20 nm-30 nm)	Less than 0.01 μm (10 nm)
Machining quality	Form accuracy	1 mm-0.5 mm	0.01 mm-0.05 mm	1 μm-2 μm	0.3 μm-0.5 μm

2.2.1 Work materials in single point diamond turning

The material properties play an important role in the material removal process, and only a few materials with good machinability in SPDT can achieve a nano-metric surface finish (Evans, 1991; Fukukawa and Moronuki**,** 1988; Okuda et al., 1989). The machinability is defined by the difficulty with which the metal can be machined to an acceptable surface finish with lower tool wear rate (Degarmo et al., 2003). In fact, only non-ferrous work materials like aluminium, copper, nickel copper alloy and acrylic plastic material can be directly machined to optical quality, as excessive chemical tool wear occurs in the machining of ferrous alloys due to the chemical reactions between the carbon of the diamond tool and the iron of the workpiece. The machinability of a material in ultra-precision diamond turning can be assessed by the achievable surface roughness, tool wear rate and chip formation.

2.2.2 Mechanics in micro-machining

The mechanics in micro-cutting are different than in traditional conventional cutting due to the depth of cut in micro-cutting being 100 times less than in conventional cutting. Merchant (1945) developed fundamental cutting theory, and most research work on the mechanics in micro-cutting are based on the assumptions made by Merchant (Ueda et al., 1986; Okuda et al., 1997). The assumptions made in Merchant's

analysis are (Burnbam, 1976):

i. The tool tip is shaped and no rubbing or plowing exists;

ii. The deformation lies in the cutting direction and normal to the machined surface, and no side flow occurs in the deformation component;

iii. The shear stresses are uniformly distributed on the shear plane;

iv. The magnitude of the resultant force (F_R) on the shear plane and the rake face are equal and in opposite directions, hence the moment can be ignored.

In Merchant's analysis, Merchant's Circle, as shown in figure 2.7, is used to define the force components in orthogonal cutting and its geometric relationship between the tool and shear plane. The shear angle (ϕ) can be determined by equation 2.5 which is a function of the tool rake angle (α) and friction angle (β). The friction angle can be calculated by equation 2.6;

$$\phi = \frac{\pi}{4} - \frac{1}{2}(\beta - \alpha) \tag{2.5}$$

$$\beta = \tan^{-1}\left(\frac{F_t + F_m \tan\alpha}{F_m - F_t \tan\alpha}\right) \tag{2.6}$$

where ϕ is the shear angle, α is the tool rake angle, β is the friction angle, F_t is the thrust force, F_m is the main cutting force.

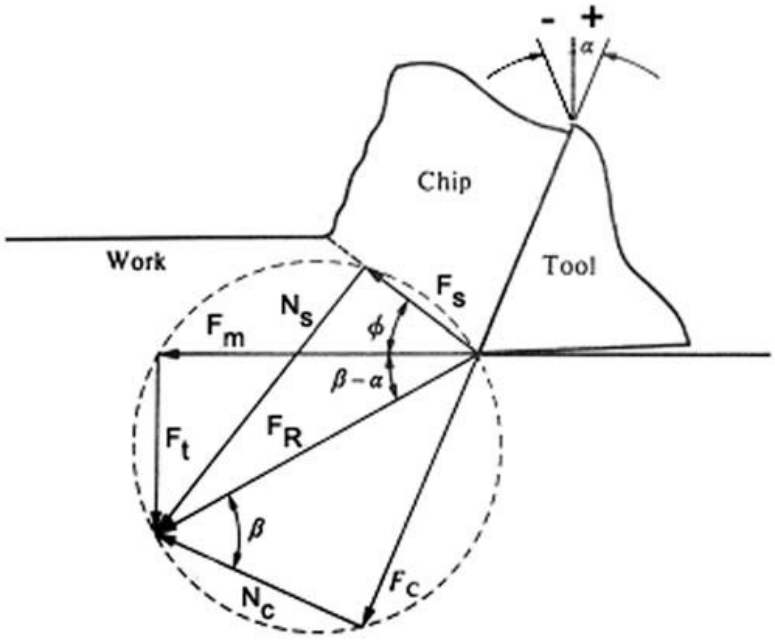

Figure2.7 Merchant's circle of orthogonal cutting (Shaw, 1954)

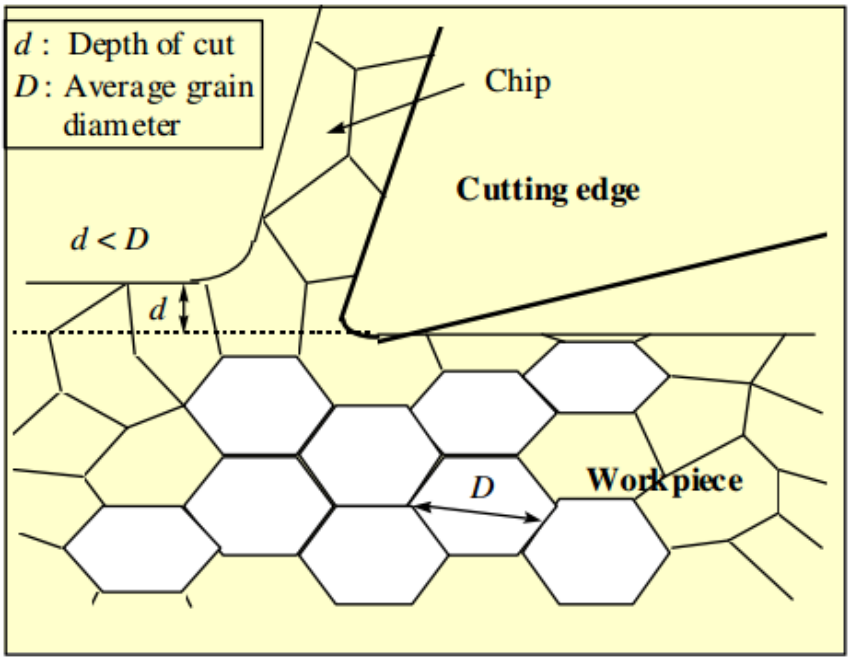

Figure 2.8 Orthogonal cutting of polycrystalline material in SPDT (Cheung and Lee, 2000)

Anisotropic materials properties are involved in the micro-cutting process as the depth of cut used in micro-cutting is smaller than the average grain size, as shown in figure 2.8, and the grain orientation near each grain being cut is different when the tool passes over the material surface. The quality of the surface finish for the machined surface is highly dependent on the workpiece material properties in SPDT. A number of studies revealed that the effect of crystallographic orientation on surface roughness, cutting force, shear angle and chip formation (Cheung et al., 2002; Lee and Zhou, 1993; To et al.,1997). Therefore, the effect of the material microstructure cannot be neglected in the micro-cutting process.

2.2.3 Surface quality in single point diamond turning

The surface quality plays an important role in the functional performance of optical products. Different studies have been performed to investigate the factors influencing the surface generation in micro-cutting processes. Surface generation is one of the important factors in the machinability of a specific material. Sata et al. (1985) indicated through fast fourier transform (FFT) analysis that the machined surface quality is influenced by the feed rate, tool geometry, swelling effect of different materials, rotational error of the spindle and the relative displacement between the tool and the workpiece by vibration. Furthermore, Mitsui et al. (1978) argued that the effect of the

tool-work vibration on the surface finishing was equivalent to the whole amplitude of vibration. This argument was questioned using experimental results which showed a finer surface than a whole amplitude is often obtained in SPDT (Tai et al., 1979).

Cheung et al. (2000) investigated the factors affecting surface generation in ultra-precision machining, and divided these factors into two categories: material and process factors, as shown as figure 2.9. The research work showed that the peak-to-valley height and arithmetic roughness would decrease with the increasing spindle speed used in diamond cutting. The effect of cutting parameters on the theoretical roughness can be determined through equation 2.7 in SPDT (Cheung and Lee, 2000]. The previous reviews show that the most important factor affecting the surface roughness is the cutting speed. The feed rate and spindle speed are directly related to the cutting speed during SPDT, and a higher cutting speed will induce a higher cutting temperature which may affect the material swelling effect, due to the BMG's superplastic deformation property under a higher temperature.

$$\text{The Mean surface Roughness (Ra)} = \frac{0.032 f^2}{r V^2} \qquad (2.7)$$

where f is feed rate, V is spindle speed and r is tool nose radius

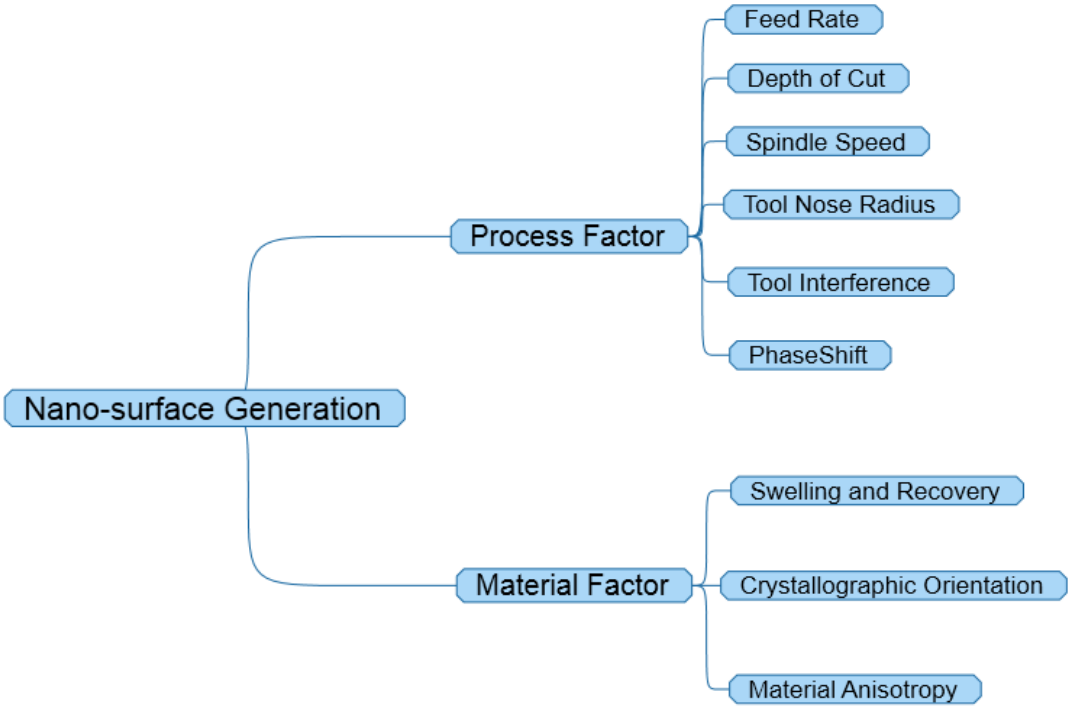

Figure 2.9 Factors affecting nano-surface generation in SPDT (Cheung et al. 2000)

2.2.4 Tool wear mechanisms and tool life

Tool wear is defined as a process of gradual tool failure in a regular cutting process. Tool wear is a time dependent process, and the wear increases with operation time in cutting. The occurrence of tool wear in a cutting process will lead a several effects on the cutting force and cutting temperature, which will lower the surface finishing and the decrease the dimensional accuracy. So studying the tool wear mechanics was being a major area for determining the material's machinability. The four types of tool wear are illustrated in figure 2.10, and the types of tool wear can be distinguished as follows:

i. Flank wear. It occurs on the tool flank as a result of friction between the

machined surface of the workpiece and the tool flank. The cutting forces increase significantly with flank wear. If the amount of flank wear exceeds some critical value, the excessive cutting force may cause tool failure

ii. Crater wear. A concave section on the tool face is formed by the action of the chip sliding on the surface. Crater wear affects the mechanics of the process, increasing the actual rake angle of the cutting tool and consequently making cutting easier. At the same time, the crater wear weakens the tool wedge and increases the possibility of tool breakage.

iii. Edge wear. It occurs on the tool corner, and can be considered as a part of the wear and respectively flank wear since there is no distinguishing boundary between the corner wear and flank wear land. We consider corner wear as a separate wear type because of its importance in precision machining.

iv. Built-up edge. It forms on the rake face of the cutting tool. The built-up edge is a semi stable body of the workpiece materials, which usually overhangs the cutting edge and periodically fractures away and adheres to the machined surface and chip.

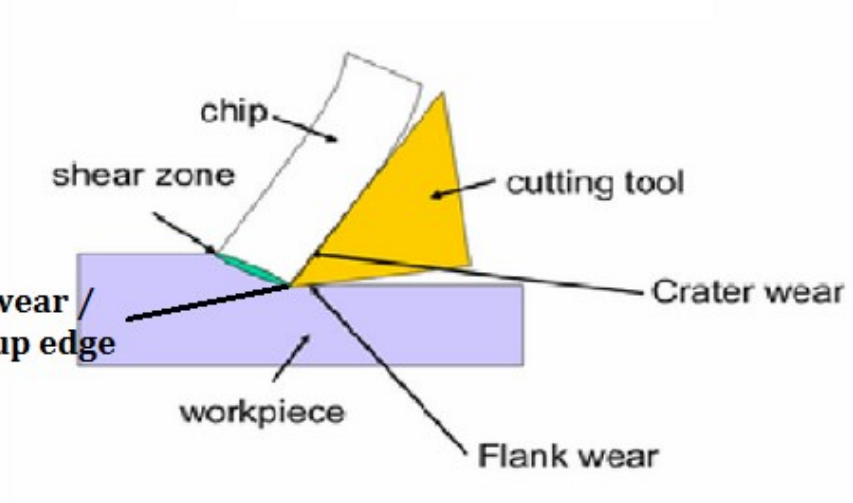

Figure 2.10 Types of tool wear

The factors that affect the rate of tool wear are the cutting condition, tool geometry and properties of the work material. Of these parameters, cutting speed is the most important factor affecting tool wear. A rapid increase in the rate of tool wear occurs under a higher cutting speed, because the rate of tool wear strongly depends on the cutting temperature.

The method for monitoring the tool wear can be divided into two categories: direct and indirect approach.

For the direct method, it is related to image capturing and comparing. The method involves using an industrial camera or optical microscope to capture the image of the tool profile without disassembling the cutting tool from the original process position, so the captured images can be analyzed by digital processing. If the tool wear exists, the area of the tool will be deceased, so the tool wear can be determined by comparing

the number of pixel reduction for the tool in the captured image.

The indirect method allows monitoring of the tool wear status online without stopping the machining process. This method captures the signal generated in the cutting process, including cutting force signals, current consuming, acoustic emission, vibration etc. to reflect the cutting tool status. Many signal processing methods have been developed to process the captured signal to reflect the cutting tool status. For example, Fourier transform, singular spectrum analysis, wavelets transform. These processing methods can be classified into two categories: the first is the signal decomposing method, and it is usually used to decompose the signals to particular sub-signals and then find the sub-signal which is related to the diamond tool wear. The second method is the FFT, which transforms the signal into the frequency domain and finds the feature frequency which is thought to be related to the diamond tool wear.

2.2.5 Investigation of shear band and chip formation

Shear band and chip formation investigations are the core aspects in studying the cutting mechanism. In the micro-cutting process, there is rich experimental evidence that shows the fluctuation in cutting force is caused by variation of the chip thickness and shear angle of the work material (Black, 1971; Satao et al., 1978). The formation of the shear bands and the shear direction are some of the major factors that affect the

surface integrity in SPDT.

Research work on investigating the shear band and chip formation in cutting is focused on the modelling of the cutting process and the formation of shear bands through developing material constitutive equations which are applied in FEM to improve the simulation results of the chip morphology.

In earlier work, Recht (1964; 1985) proposed a model for the adiabatic shear theory of saw-tooth chip formation to explain the dynamic plastic deformation of materials under the thermo-instability condition. This study considered the shear bands arising in cutting with the material properties. The assumption made in this model was that thermoplastic instability occurs and extends the tool tip up towards the free surface. However, the model could not explain why the shear bands could be initiated at the free surface

A slip-line model for machining with a round-edge was been developed by Fang (2003a, 2003b). In the model, a set of analytical equations were used to predict the thickness and shear strain rate in the primary shear zone. The model need the assumption of orthogonal cutting with continuous chips and a rigid plastic material under plane-strain compression. The limitation for the model was that it didn't consider the effect of the elastic strain stored in the material during cutting.

In order to explain the shear band initiation, propagation and forming during

cutting by considering the material behavior, Wand et al. (2010) proposed a model for the elastic strain induced shear bands in the micro-cutting process. The FEM model suggested that the shear bands were initiated in a region around the tool tip and were then propagated outwards to the free edge of the chip. Figure 2.11 shows the simulation results on the elastic strain inducted shear bands in the micro-cutting process. However, the model was limited to ductile materials and the initial stage of the shear band, and didn't consider the propagation of the elastic strain during the cutting process.

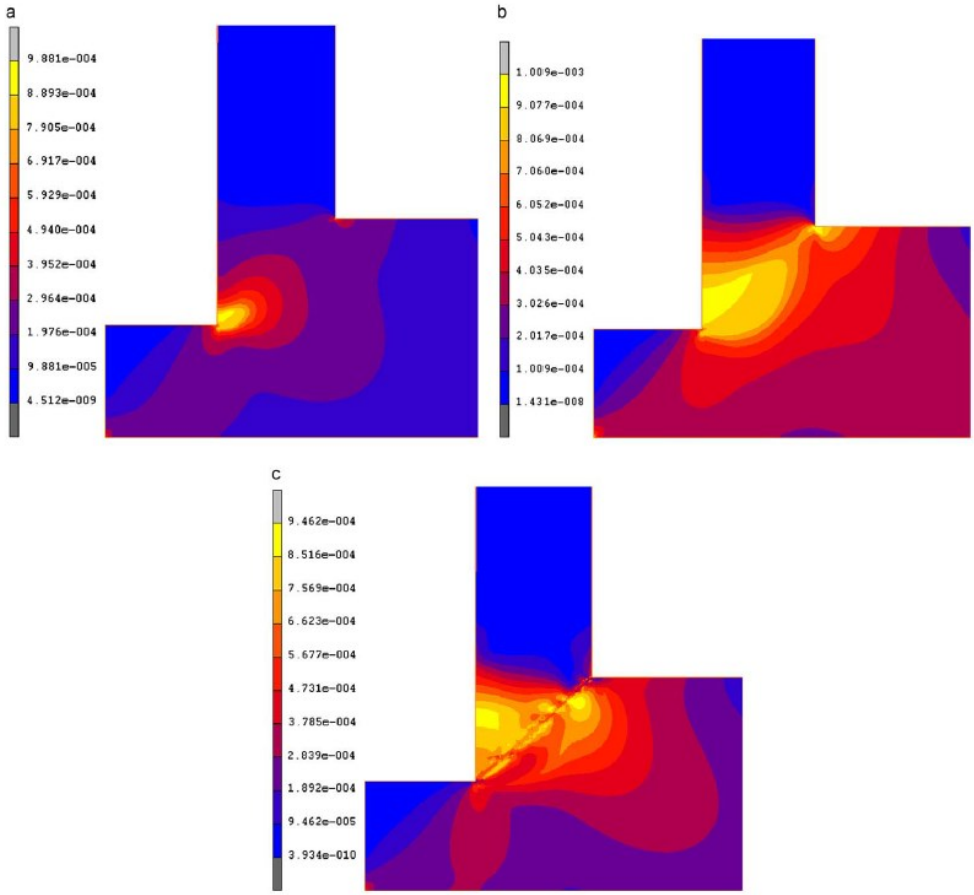

Figure 2.11 Evolution of equivalent elastic strain

Muhammad and his co-workers (2013) proposed a model to predict the critical

underformed chip thickness for ductile-brittle transition in the nano-machining of brittle materials. The model predicts the chip thickness for ultra-precision machining of silicon under different tool geometries and process parameters in terms of the specific energy in the process. The model is limited to brittle materials and ignores the material deformation behavior due to the machining temperature.

2.3 Modelling and simulation techniques for machining

2.3.1 Slip-line field modelling of machining

The stresses and forces during the material deformation can be studied using slip-line field modeling; the working principle for the model is in analyzing the maximum shear stress during cutting. So, slip-line field models are always applied to metal cutting processes for investigating the plastic deformation. One of the assumptions is that rigid-plasticity is adopted in various slip-line field models of the machining process, where the elastic behavior is not taken into consideration. The model assumed that the plane strain is perfectly plastic and there is constant friction shear stress, etc. (Fang 2003a, 2003b; Fang and Dewhurst, 2005; Toropov and Ko, 2003) As explained by Fang (2003a), the well-received Merchant's model (Merchant 1945a) based on cutting forces can be derived from Fang's model. The eight special cases mentioned are shown in figure 2.12.

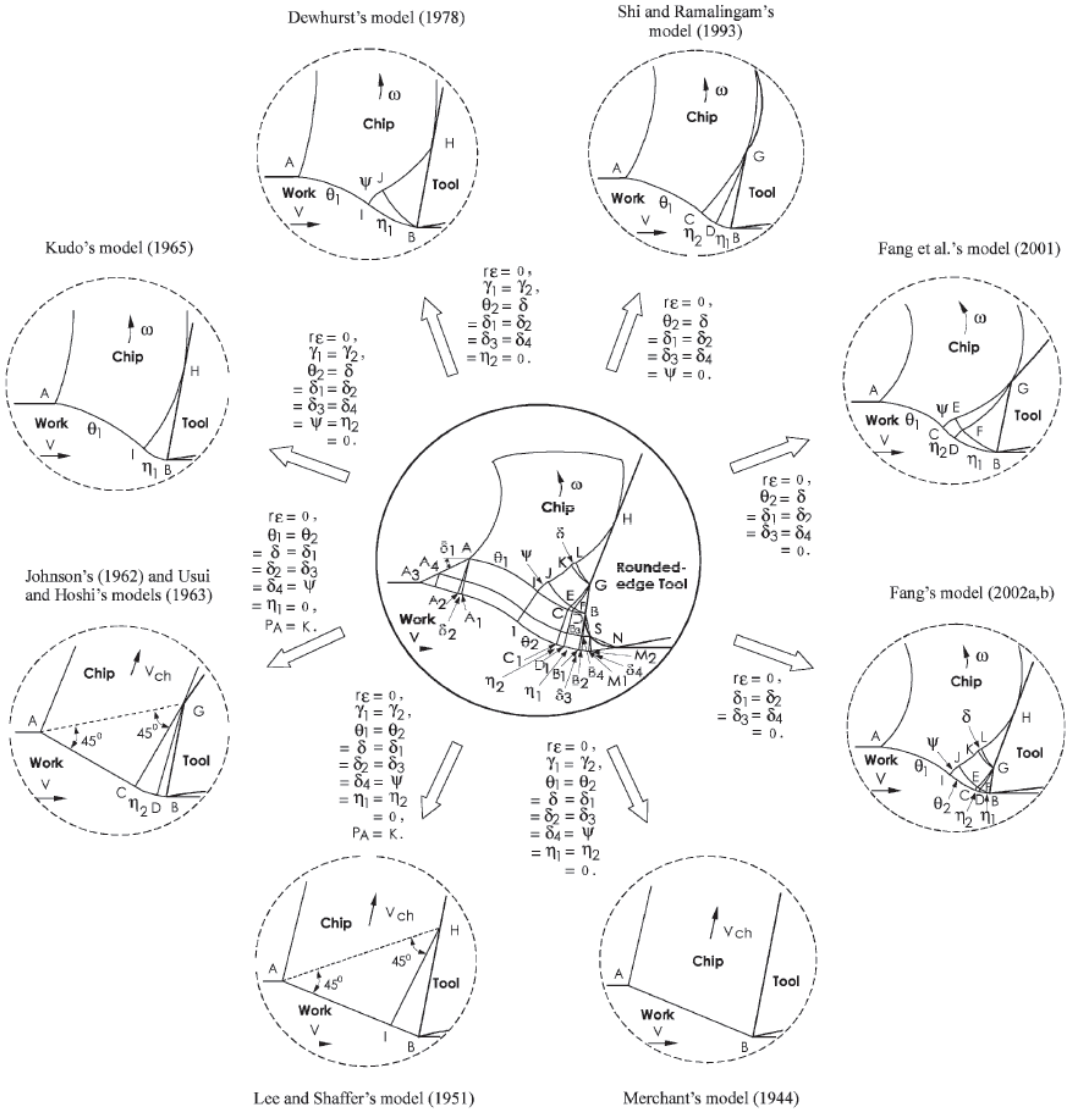

Figure 2.12 Eight special case of Fang's slip-line model (Fang, 2003a)

2.3.2 Molecular dynamics simulation of machining

Molecular dynamics simulation (MDS) is a computer simulation method which demonstrates the interaction between atoms and molecules over a period of time by approximations of known physics. MDS has been applied in the modelling and simulation of nano-indentation testing, scratching testing and nano-machining, etc

(Tresoff, 1986; Lin and Huang, 2004; Fang et al., 2005, 2007; Shimada et al., 1993; Inamura et al., 1997). In addition, MDS has succeeded in simulating tool wear in the nano-cutting process (Konmanduri et al., 1998; Komanduri et al., 2000). A graphical illustration for simulating the nano-cutting process is shown in figure 2.13.

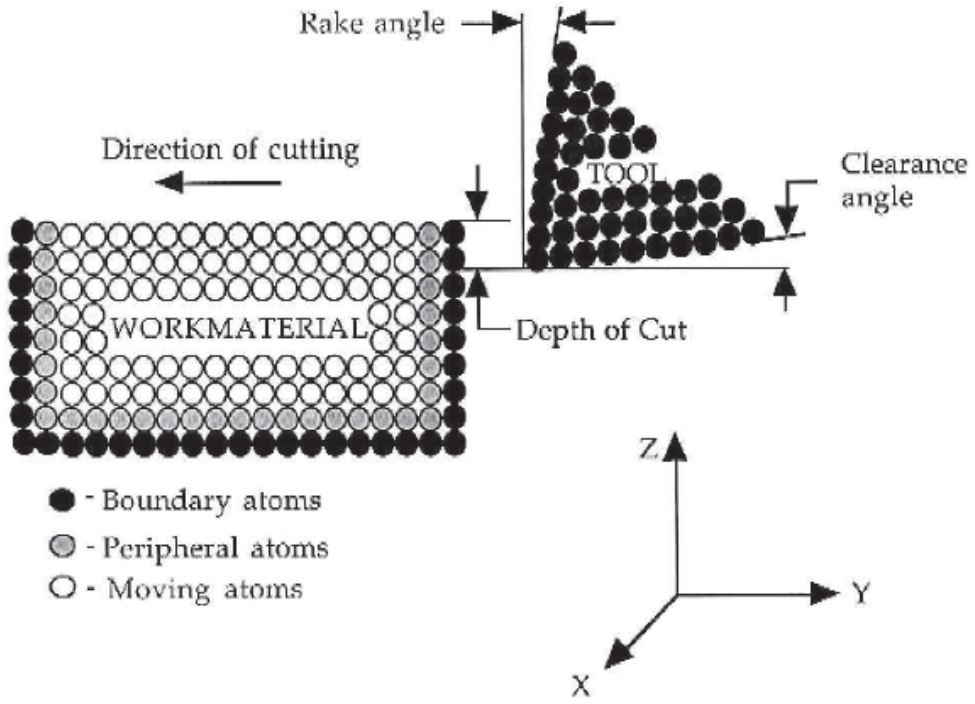

Figure 2.13 MDS of nanometric cutting (Komanduri et al., 2000)

The MDS model can define the anisotropy of a single crystal material as an intrinsic property during simulation of nano-cutting. The MDS is a more appropriate method simulate to the micro-, meso- and macro- scales than the finite element method. Although these simulation works require huge calculations, the model had been

successfully adapted to a deformation layer of less than tens of nanometres due to the high computation intensity. Fang et al. (2007) developed a model for uncut chip thicknesses smaller than 3mm, with a time step of 39 fs. A constraint for MDS is that the results are difficult to verify, because the depth of cut used in the micro-cutting process is much higher than the uncut chip thickness used in MDS.

2.3.3 Finite element modelling

The first finite element model was developed by Zienkiewicz (1971) and Kakino (1971) and used to study chip formation and simulate the loading of a tool against a pre-formed chip without modelling large-volume flows of the work material. The model ignored the friction between the chip and tool, effect on the strain rate and temperature are ignored. Five year later, Shirakashi and Usui (1976) proposed a model to consider extra factors in the simulation. They developed an iterative approach in changing the shape of the preform until the simulated plastic flow was consistent with the designated shape. The model also included the realistic tool-chip friction conditions, a temperature calculation and material flow stress variations with strain etc. In 1984, Iwata et al. proposed a steady state rigid-plastic model within a Eulerian framework to determine the material and frictional properties in the orthogonal cutting process.

For chip formation simulation, a remeshing software to adapt both the rigid-plastic

(Sekhon and Chenot, 1993; Ceretti et al., 1996) and elastic-plastic (Marusich and Ortiz, 1995) has been developed. In addition, the arbitrary lagrangian-eulerian (ALE) methods in which the mesh is neither fixed in space nor in the workpiece, are implemented in the commercial FEM software, such as ABAQUS, DEFORM, etc. The ALE methods have been adopted by many researchers, such as Rakotomolala et al. (1993).

The constitutive equations are the equations to determine the simulation results and the related factors that can be considered in the models to achieve a better simulation results. Analysis for the thermal-stress is required when the stress distribution is a function of the temperature distribution. A number of finite element studies (Liu and Melkote, 2004; Kim et al., 1999; Guo, 2004; Shi and Liu, 2004) used the empirical flow stress equations in combining strain hardening, strain-rate effects and thermal softening - the most popular model to combine above factors is that of Johnson and Cook (1985). In addition, based on the notion of geometrically necessary dislocations in dislocation mechanics, strain gradient plasticity theories have been proposed where the strain gradient dependence of the flow stress is introduced into the material constitutive model (Fleck et al., 1994; Fleck and Hutchinson, 1993; Gao et al., 1999; Acharya and Bassani, 2000).

2.4 Limitation of current theories and models

Many theoretical and experimental studies have focused on the surface generation and the formation of shear bands in the micro-cutting of crystalline or diamond machinable materials. Recent research on the surface integrity in single point diamond turning focused on the crystallographic effect. So far, limit research has been applied to amorphous metal alloys in ultra-precision machining for the study of machinability, surface integrity, and cutting mechanic. The material removal behavior in the supercooled liquid region has not been investigated in previous research work. The characterization of the microstructure change due to the micro-cutting process has not been addressed in the literature. In addition, models for the shear bands and prediction of shear angles focus on crystalized materials and ignore the shear transformation in the primary deformation zone.

Due to insufficient understanding of the cutting mechanics and shear bands in the precision cutting of metal glasses, more work will be done on studying the cutting mechanics and surface integrity in the diamond cutting of BMGs through theoretical and experimental analyses. Studies on the shear band and chip formation mechanism in diamond cutting of BMGs, with various cutting parameters, are required to investigate the material removal behavior of BMG in the micro-cutting process.

2.5 Summary

A review of the research background of bulk metallic glasses, the deformation behavior of BMG, ultra-precision machining, surface generation, tool wear, shear bands and chip formation is given in this chapter. Two classical models for describing the plastics deformation behavior of bulk metallic glasses have been reviewed, which are free volume model and shear transformation modal. The modeling techniques on micro-cutting process have been reviewed, including the slip-line field modeling, molecular dynamics simulation, and finite element method. The advantages and constraints of each modeling method have been discussed.

The limitations of existing research have been identified through an in-depth literature study. The limitations of current theories are summarized as: (i) there has been limited research work on the cutting characteristic of amorphous alloys with various cutting parameters; (ii) the shear band formation an propagation in the micro-cutting of amorphous alloys has not been fully covered by the classic model in ultra-precision diamond cutting; (iii) limited work on modelling the chip formation in the micro-cutting of amorphous alloys; (iv) the microstructure change due to the micro-machining of BMGs has not been recognized.

Chapter 3 Machinability of bulk metallic glasses in ultra-precision diamond cutting

3.1 Introduction

Bulk metallic glasses are alloys possessing an “amorphous” atomic structure, which results in the absence of crystallites, grain boundaries and dislocations. The amorphous structure provides unique properties including superior mechanical strain and hardness, excellent corrosion and wear resistance, which leads a potentially wide range of functional and high precision applications. Although metallic glasses are suitable for making precise micro-components by micro injection molding due to macroscopically homogenous and superplastic deformation ability (viscous flow) in the super-cooled liquid region (temperature in the range of the glass transition temperature, T_x, to the crystallization temperature, T_g) (Yu and et al.,2012), the micro-forming method cannot handle high complex-shape geometries and the metallic glasses cannot fully fill deep-cavity shapes during molding process due to the capillary force effect (Kumar and Tang, 2009). Ultra-precision diamond cutting can complement the limitation on the micro-forming process based on the capability of arbitrary shape forming, high form accuracy and ultra-fine surface finishing.

The machinability of bulk metallic glasses was investigated by Bakkal et al.

(2004; 2005) in the macro-machining process. Light emission occurred in the machining process with a high cutting temperature of about 2500K, which induced oxidation and crystallization on the chips, and tool wear. This phenomenon occurs in the machining experiments, the bulk metallic glass can be characterized as a different-to-cut material due to the unique mechanical properties, high elastic modulus, high strength and low thermal conductivity. Although the machinability of bulk metallic glasses was studied, the machining characteristic is still not clear in micro-machining due to the material properties on the macro scale being much different than on the micro scale. The proposed study experimentally addressed the machinability of Zr-based bulk metallic glass with the composite $Zr_{55}Cu_{30}Al_{10}Ni_5$ in single point diamond cutting. Zr-based bulk metallic glasses are promising amorphous alloys with superior mechanical properties and high glass forming ability, and can be used in high level precision components. The proposed investigation included the machined surface quality, cutting force, diamond tool wear and the microstructure changes on the bulk metallic glasses by micro-machining.

3.2 Experimental setup

The bulk metallic glass workpieces were round bars of $Zr_{55}Cu_{30}Al_{10}Ni_5$ alloy, 5mm in diameter, fabricated using the extrusion method in an arc-melting furnace with

copper mold suction casting under a high purity argon atmosphere. The mechanical and physical properties of the material as shown in table 3

The face turning experiments were carried out on a Nanotech 350FG (4-axisultra-precision diamond turning machine). Four variables were controlled in the turning experiment were: (1) two tool nose radii (0.4 mm and 1.5 mm) with -5° rake angle. (2) four spindle speeds (4000 rpm, 3000 rpm, 2000 rpm and 1000 rpm), (3) three depths of cut (1 μm, 2 μm, 3 μm and 4 μm) and (4) four feed rates (1 mm/min, 5 mm/min, 10mm/min and 15 mm/min). The experimental parameters for studying the effect of cutting conditions on surface generation are shown in table 4. In total, 18 cutting tests were conducted, using the cooling oil Clairsol 330. The experimental set up is shown in figure 3.1.

Table 3 Mechanical and physical properties of workpiece

Material	Yield Stress (MPa)	Thermal Conductivity ($Wm^{-1}K^{-1}$)	T_g (K)	T_x (K)
$Zr_{55}Cu_{30}Al_{10}Ni_5$	1860	5.02	663	716

Table 4 Cutting conditions

<table>
<tr><th>Depth of Cut (μm)</th><th>Spindle Speed (rpm)</th><th>Feed Rate (mm/min)</th><th colspan="2">Tool Nose Radii (mm)</th><th>Rake Angle (°)</th></tr>
<tr><td colspan="3">Spindle Speed</td><td rowspan="12">1.5</td><td rowspan="12">0.4</td><td rowspan="12">-5</td></tr>
<tr><td rowspan="4">1</td><td>1000</td><td rowspan="4">5</td></tr>
<tr><td>2000</td></tr>
<tr><td>3000</td></tr>
<tr><td>4000</td></tr>
<tr><td colspan="3">Feed Rate</td></tr>
<tr><td rowspan="3">1</td><td rowspan="3">1000</td><td>15</td></tr>
<tr><td>10</td></tr>
<tr><td>1</td></tr>
<tr><td colspan="3">Depth of Cut</td></tr>
<tr><td>2</td><td rowspan="3">1000</td><td rowspan="3">5</td></tr>
<tr><td>3</td></tr>
<tr><td>4</td></tr>
</table>

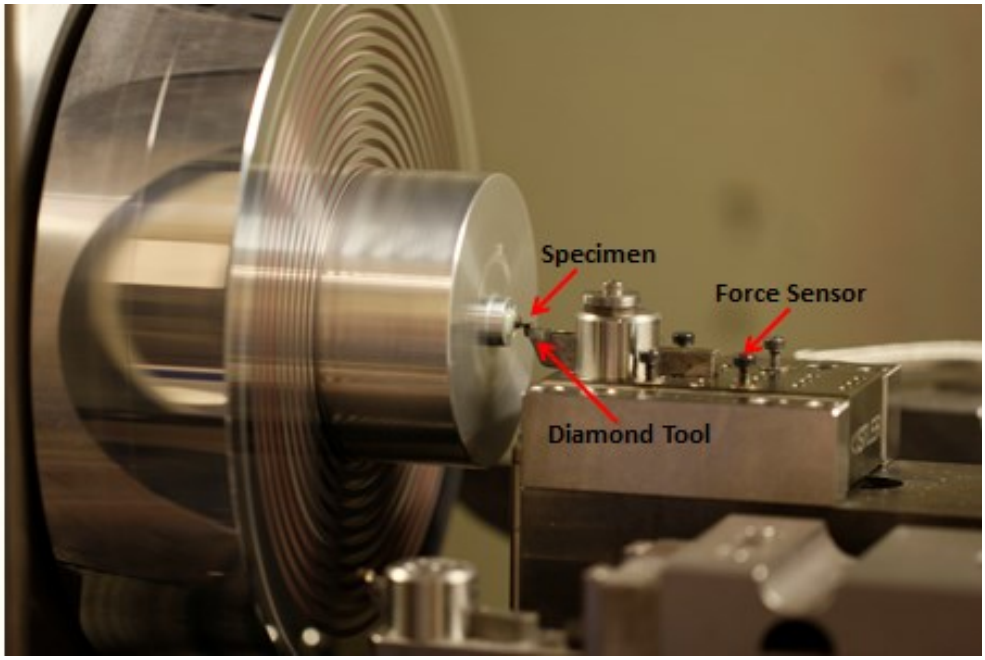

Figure 3.1 Experimental set up

3.3 Characterization method

The arithmetic mean surface roughness (R_a) of each machined surface was measured by an optical profiling system (Wyko NT8000). The diamond tool was examined by scanning electron microscopy (Hitachi Tabletop Microscope TM3000). A Kistller 9252A piezoelectric force transducer mounted under the tool holder was used to capture the cutting force (F_c) and thrust force (F_t) in the cutting process. The crystal structure of the cast and diamond turned BMG specimens were characterized by an X-ray Diffraction (RigakuSmart Lab). The phase ID testing was conducted by an X-ray diffraction (XRD) with nick-filtered CuKα.

3.4 Characterization of the crystal structure in diamond cutting BMG

The XRD phase ID test results are shown in figure 3.2, the red broadened and obtuse diffraction peak of the XRD phase ID test result shows the amorphous structure for the cast Zr-based BMG, and the blue peak shows that the amorphous microstructure remains unchanged after diamond turning. This indicates two possibilities: one is that the cutting temperature did not reached to T_x during the diamond cutting process, and the other is that the cutting temperature could not be transited from the cutting edge to the sub-surface layer of the machined surface due to the low thermal conductivity of BMG.

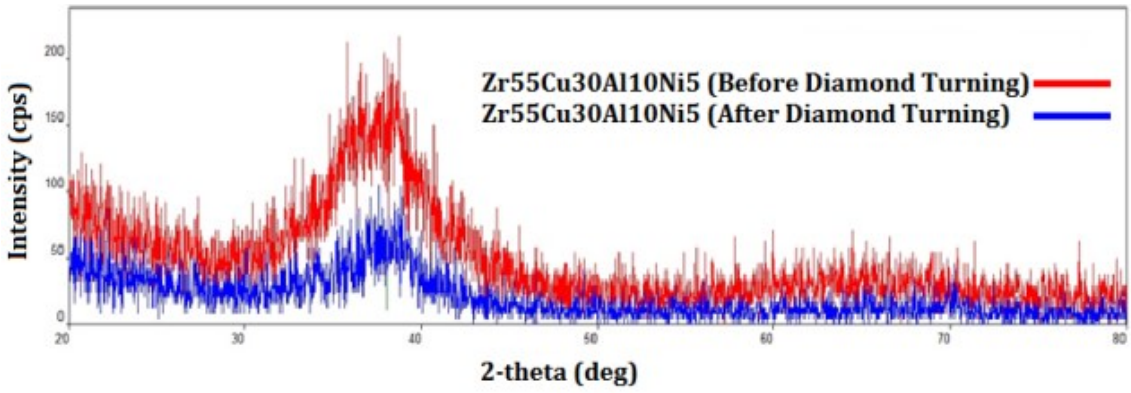

Figure 3.2 XRD phase ID test results for Zr-based BMG specimens before and after diamond turning

3.5 Surface roughness and surface texture

Under the cutting process in theoretical condition, the surface roughness profile is formed by the repetition of the tool tip profile at intervals of feed per revolution, which is determined by the spindle speed and feed rate. The theoretical relation between the surface average roughness R_a and cutting conditions can be expressed as follows (Cheung and Lee, 2000):

$$\text{The Mean Surface Roughness (Ra)} = \frac{0.032f^2}{rV^2} \quad (3.1)$$

where f is the feed rate and r is the tool nose radius. In general, this theoretical equation cannot estimate the R_a value accurately due to the material factors, for example, the deformation mechanics and material recovery of the workpiece. The results in the surface generation can be divided into 4 parts; the effect of the spindle speed, feed rate, depth of cut on surface roughness and cutting force analysis.

3.5.1 Effect of spindle speed

The effect of spindle speed on the arithmetic roughness for different tool nose radii is shown in figure 3.3. The arithmetic roughness values shown in figure 3.3 to 3.5 were the average value of three specimens. In figure 3.3, it was found that the arithmetic roughness increases with increasing spindle speed. When the spindle speed increased

from 1000 rpm to 4000 rpm for the tool nose radii in 1.5 mm, the R_a value increased from 7.5 nm to 26.3 nm. The experimental results show that the roughness of BMG is sensitive to the spindle speed, a different trend to the predicted surface roughness by equation 3.1. The discrepancy between the predicted and measured roughness can be explained by the material swelling effect, built-up edge (BUE) on diamond tool and crack formation at high cutting speed.

An adiabatic system occurs in the shear deformation zone due to the lower thermal conductivity of Zr-based BMGs (5.02 W/mK). The temperature increases due to the plastic deformation within the shear deformation zone, the temperate rise at the shear band have been estimated as ranging from less than 0.1 Kelvin to a few thousand Kelvin (Bengus et al., 1993). Based on the molecular dynamic simulation conducted by Zhu and his coworkers (2014), the temperature in nanoscale cutting of the $Zr_{-50}Cu_{30}$ metallic glasses can reach to 600-700 K which is higher than the glass transition temperature of the workpiece material. The higher spindle speed will induce a higher temperature due to the higher rate of plastic work, which leads to a thermal softening effect on the BMGs. A supercooled liquid region exists when the working temperature is raised to the BMG's glass transition temperature, which increases the plasticity of the BMG and the swelling occurred. The material swelling distorted the tool mark formed on the machined surface. As a result, the machined surface roughness value increases with increasing the spindle

speed due to the swelling effect.

As the cutting temperature increased with increasing the spindle speed. The workpiece became softer when the cutting temperature is rasies to the glasses transition temperature, the workpiece were adhered on the cutting tool and formed BUE. The BUE on diamond tool was adverse for the surface quality.

Besides, the effect of strain rate on the compressive failure strength was reported to decrease with increasing strain rate (Li et al., 2003). The literature reported that the plasticity of BMG enhanced by the formation of disordered multiple shear bands in the process of quasi-static uniaxial compression testing (Liu et al., 2005). However, the higher spindle speed inhibited the initiation and propagation of shear bands, and the sufficient time for releasing the built-up stress is not sufficient. The high rate of load led the crack formation in the micro-cutting BMG due to the inhomogeneous deformation. As a result, the R_a value increased with increasing the spindle speed due to the crack formation.

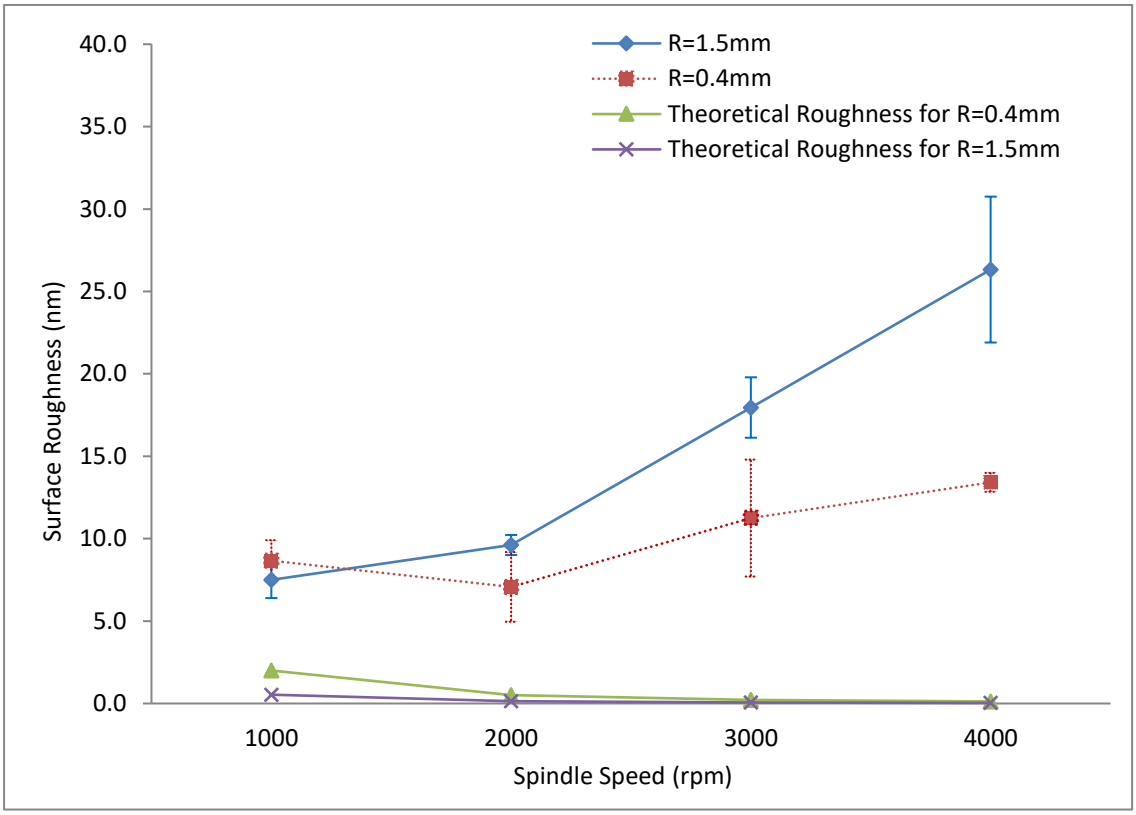

Figure 3.3 Effect of spindle speed on arithmetic roughness for tool nose radii of 0.4mm and 1.5mm (Depth of cut at 1 μm and feed rate at 5mm/min)

3.5.2 Effect of feed rate

The effects of feed rate on the arithmetic roughness for different tool nose radii are shown in figure 3.4. The R_a values are found to increase from 8.0 nm to 25.1 nm when increasing the feed rate from 10 mm/min to 15 mm/min in the tool nose radii in 1.5 mm. The experimental result shows a similar trend between the measured roughness and the predicted surface roughness by equation 3.1 that the R_a value decreases with increasing feed rate from 10 mm/min to 15 mm/min. A large variation in R_a values

being found when applying tool nose radii in 1.5 mm at a feed rate of 15 mm/min. The thermal softening occurred in the micro-cutting of BMG due to the low thermal conductivity. The cutting temperature increased with increasing the feed rate, material swelling occurred when the cutting temperature raised to glass transition temperature. Therefore, the tool mark formed on the machined surface shown an irregular pattern which resulted a large variation in R_a value in a feed rate of 15 mm/min.

There is a large variation in the R_a value being found at a feed rate in 1mm/min. The BUE formed on the cutting tool induced additional surface roughness to the machined surface at the low feed rate. The BUE damaged the machined surface by scratching. The contact area between the tooltip and workpiece increased by reducing the feed rate under constant spindle speed due to the tool path. Therefore, the chance for the BUE scratch the machined surface at a lower feed rate is higher than in a higher feed rate, so the R_a value is high at feed rate in 1mm/min. There is a larger discrepancy on the Ra value between the tool nose radii in 0.4 mm and 1.5 mm. Since the BUE area formed on the diamond tool increases with increasing tool nose radii. As a result, the R_a value increased with increasing the tool nose radii at feed rate in 1 mm/min.

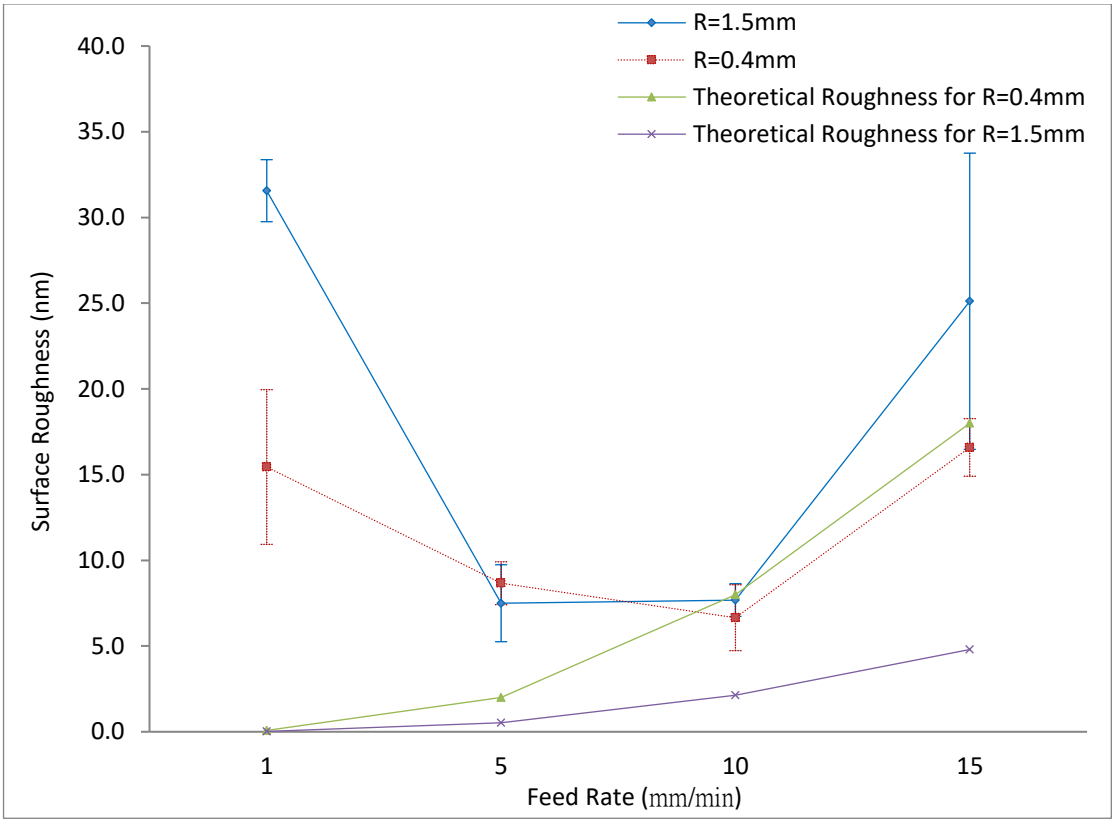

Figure 3.4 Effect of feed rate on arithmetic roughness for tool nose radii 0.4mm and 1.5mm (Depth of cut at 1 μm and spindle speed at 1000 rpm)

3.5.3 Effect of depth of cut

Figure 3.5 shows the effect of depth of cut on the surface roughness for different tool nose radii. The surface roughness increases when increasing the depth of cut from 1 μm to 3 μm. The R_a values are found to increase from 7.6 nm to 35.1 nm when increasing the depth of cut from 1 μm to 3 μm in the tool nose radii in 1.5 mm. The effect of depth of cut on the surface roughness are significant by increasing the depth of cut from 1 μm to 3 μm when the tool nose radii in 1.5 mm. As mentioned in the

previous section, swelling effects occur more readily during cutting due to the lower thermal conductivity of the Zr-based BMG. A greater depth of cut will lead to a higher temperature in cutting which leads to a thermal softening effect on the BMGs. So the surface roughness increases by increasing the depth of cut in the range of 1 μm to 3 μm due to the swelling.

The Ra value reduced when the depth of cut increased from 3 μm to 4 μm. The cutting edge was not being considered as a sharp edge due to the small depth of cut applied in the micro-cutting process, and the tool edge radii are comparable in size to the uncut chip thickness. The actual effective rake angle became negative in the micro-cutting process (Fang, 2003b). An elastic-plastic deformation of the workpiece and the elastic recovery at the clearance face occurred in the micro-cutting process. As the elastic limit of BMGs is 10 times larger than the crystallize metal, the elastic recovery behind the cutting edge enhanced the swelling effect in the depth of cut from1 μm to 3 μm. When the depth of cut increased from 3 μm to 4 μm, the effect of the elastic recovery on the tool mark formed on the machined surface was minimized. As a result, the R_a value reduced in the depth of cut at 4 μm.

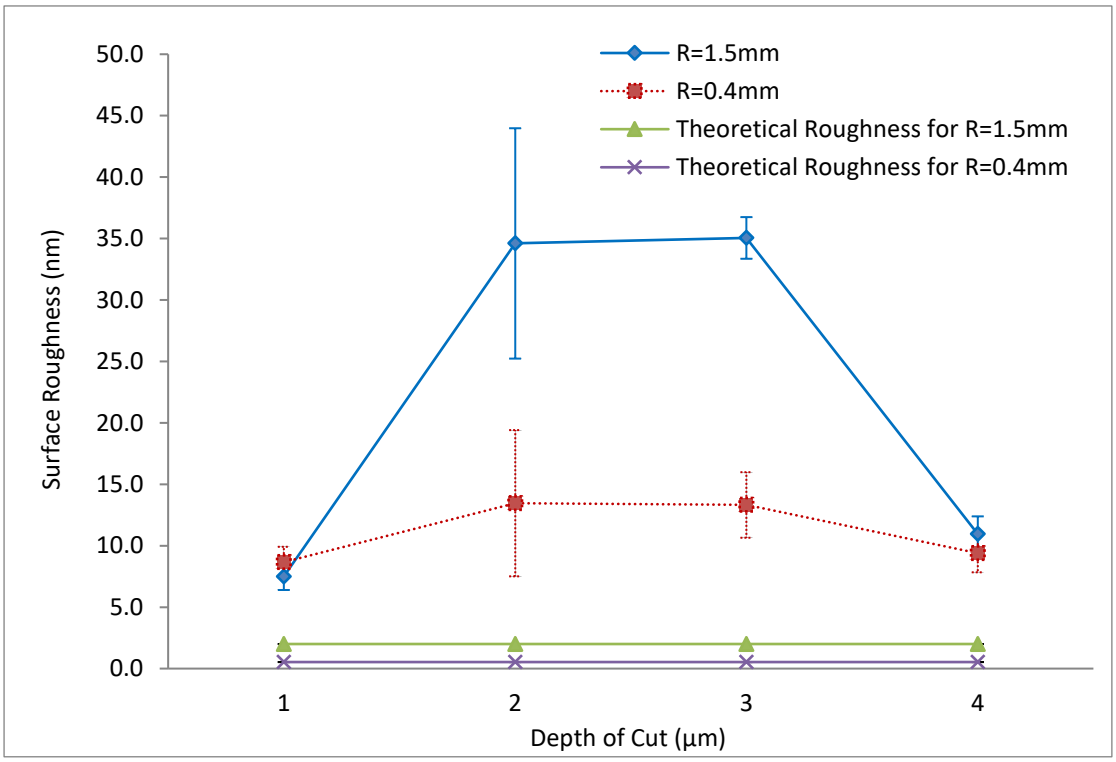

Figure 3.5 Effect of depth of cut on arithmetic roughness for tool nose radii 0.4mm and 1.5mm (Spindle speed at 1000 rpm and feed rate at 5mm/min)

3.5.4 Cutting force and thrust force

Tables 5 and 6 show the results of the cutting force and thrust force in various cutting conditions. The experimental results show the cutting forces for a tool nose radius of 1.5 mm are larger than for a tool nose radius of 0.4 mm. Also, a finer surface is associated with a lower cutting force.

The cutting force in SPDT of BMG is increased by increasing the spindle speed and depth of cut. The cutting force ratio (CFR) is used to study the relative magnitude of the force components for different cutting parameters. The CFR results show that

there is no significant correlation between cutting force, thrust force and the surface roughness. There is a high variation of CFR on the cutting parameters at a spindle speed of 1000 rpm, feed rate of 10 mm/min, 1 µm depth of cut and 0.4 mm tool nose radius, but the CFR at the same cutting condition for a 1.5 mm tool nose radius is low, providing evidence that the variation is not caused by the change in cutting conditions, and is possibly due to a material defect.

Table 5 CFR and surface roughness result in various cutting parameters on tool nose radii of 0.4mm

Cutting Parameter				Force		
Depth of Cut (µm)	Spindle Speed (rpm)	Feed Rate (mm/min)	Ra(nm)	Cutting Force (mN)	Thrust Force (mN)	CFR (Ft/Fc)
1	1000	5	8.7	145.64	324.82	2.23
1	2000	5	7.1	198.18	426.95	2.15
1	3000	5	22.6	400.84	637.65	1.59
1	4000	5	25.5	435.30	942.00	2.16
1	1000	15	16.6	513.34	1082.78	2.11
1	1000	10	10.1	440.23	9302.48	21.13
1	1000	1	15.4	443.39	755.64	1.70
2	1000	5	13.5	450.92	927.11	2.06
3	1000	5	13.3	601.34	1238.48	2.06
4	1000	5	9.4	692.88	1455.98	2.10

Table 6 CFR and surface roughness result in various cutting parameters on tool nose radii of 1.5mm

Cutting Parameter				Force		
Depth of Cut (μm)	Spindle Speed (rpm)	Feed Rate (mm/min)	Ra(nm)	Cutting Force (mN)	Thrust Force (mN)	CFR (Ft/Fc)
1	1000	5	7.5	260.15	356.28	1.37
1	2000	5	9.6	455.49	502.38	1.10
1	3000	5	18.0	771.65	707.20	0.92
1	4000	5	26.3	757.20	763.43	1.01
1	1000	15	28.7	609.70	896.89	1.47
1	1000	10	7.7	598.14	965.43	1.61
1	1000	1	45.9	974.58	1105.07	1.13
2	1000	5	34.6	704.00	457.60	0.65
3	1000	5	48.3	409.72	511.40	1.25
4	1000	5	11.0	997.85	1185.30	1.19

3.5.5 Summarized findings in surface generation

The results show that the surface roughness is sensitive to the depth of cut and spindle speed due to the swelling effect and BUE formed. This is because the temperature in the cutting zone is increased by increasing the depth of cut and cutting speed in diamond turning. The high working temperature leads to a thermal softening effect on the BMGs, and the softening will increase the plasticity of the BMG. So the swelling effect becomes serious at high cutting temperatures. In addition, the softening effect will increase the area between the work material and tool, and the BUE formed

on the tool will damage the machine surface.

The atomic structure for the machined BMG is still amorphous, and the best surface roughness achievement in SPDT BMG is 7.5 nm, under the optimum cutting parameters, with a feed rate in 5mm/min, spindle speed 1000 rpm and depth of cut of 1 μm. An optical microscope image for the optimum cutting condition is shown in figure 3.6. Figure 3.7 shows the surface profile for the machined BMG surface under the optimum cutting parameters. Based on the calculation for the theoretical roughness, the surface height is 0.0021 μm, but the machined surface height is 0.03 μm which is near 10 times higher than the calculated value. A swelling mark was found from the figure 3.7.

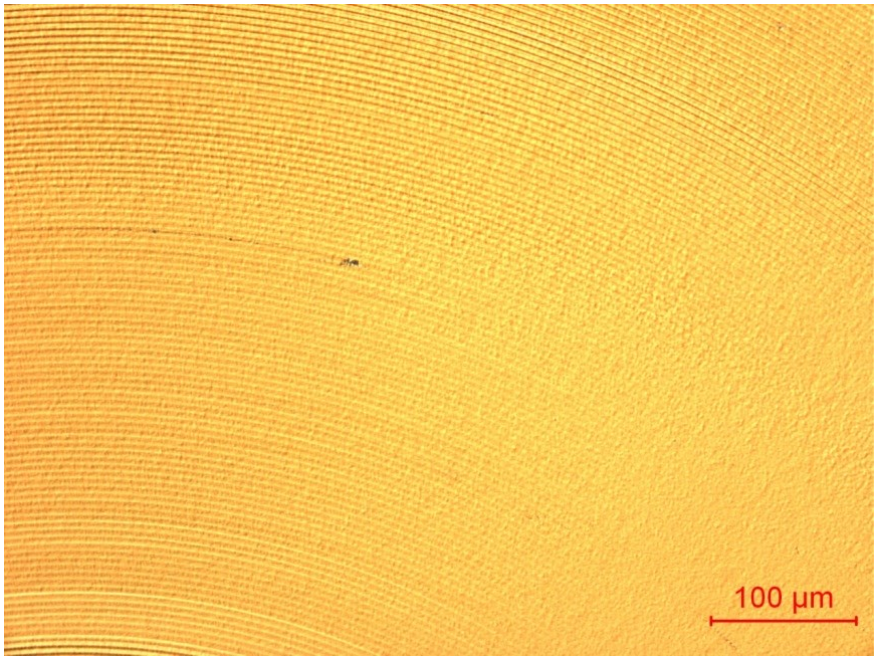

Figure 3.6 Optical microscope image with 20X magnification with optimum cutting condition

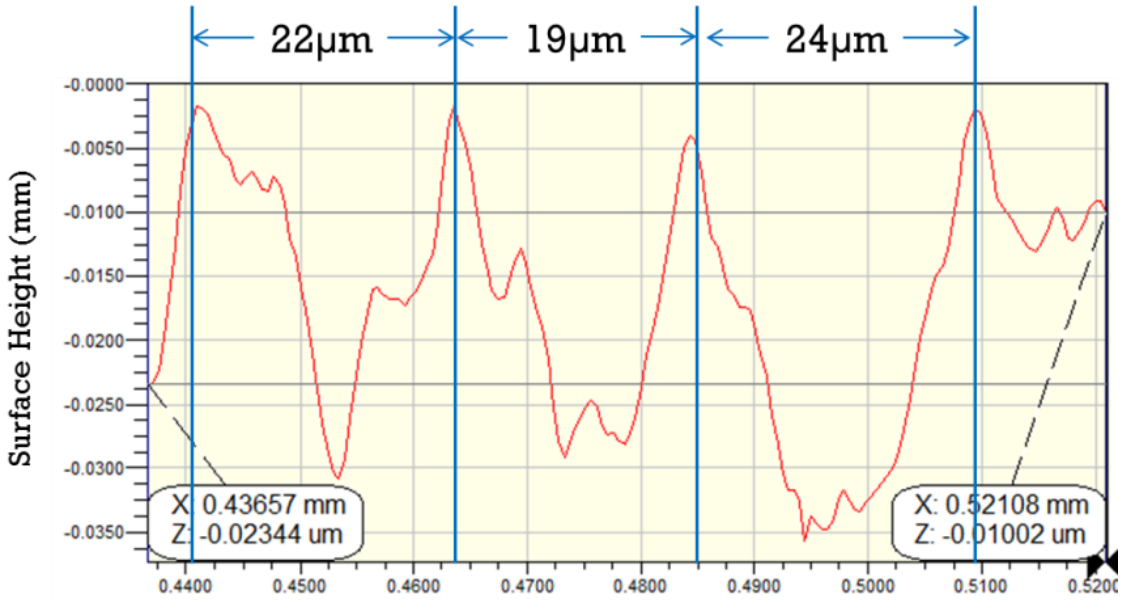

Figure 3.7 Surface profile data captured by Wyko

3.6 Tool wear investigation

Tool wear was evaluated in the diamond turning of BMG materials and the important findings are summarized as follows. First, the chips generated in diamond cutting can be welded to the cutting edge of the diamond tool during the material removal process. Figure 3.8 shows a scanning electron microscopy (SEM) image for the diamond tool which machined the BMG with a string of BMG chips welded to the tool tip after turning. The SEM micrograph of the diamond tool, with tool nose radii of 1.5 mm used after machining BMG, is shown in figure 3.9. The welded chips can be observed not only around the tool nose region and cutting edge, which are key areas in the material removal process in the secondary and tertiary deformation zones, but also in the cutting edge adjacent to the tool tip, an area not in physical contact with the

workpiece. The SEM index test result is shown in figure 3.10, which illustrates the built-up material on the cutting edge, and matches with the machined BMG composites. It confirms that the BUE is not caused by the specific elements in the BMG alloy, so the BUE cannot be reduced by changing the BMG composition.

Figure 3.11 is a graphical illustration of the built-up material formation at the tool edge in diamond cutting. As mentioned in the previous section, the increased cutting speed and depth of cut result in an increased temperature at the cutting zone. The BUE formed due to the high cutting temperature leads to super-plasticity in the BMG, and the contact between the BMG and tool tip is increased in the supercooled liquid region.

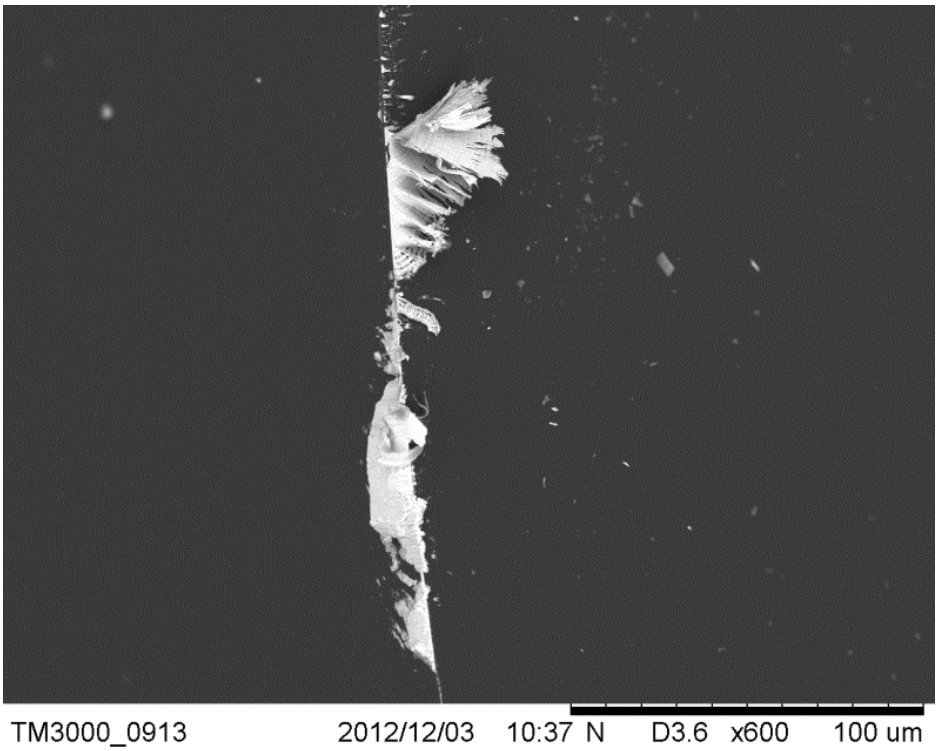

Figure 3.8 SEM image for diamond tool with tool nose radii 1.5mm

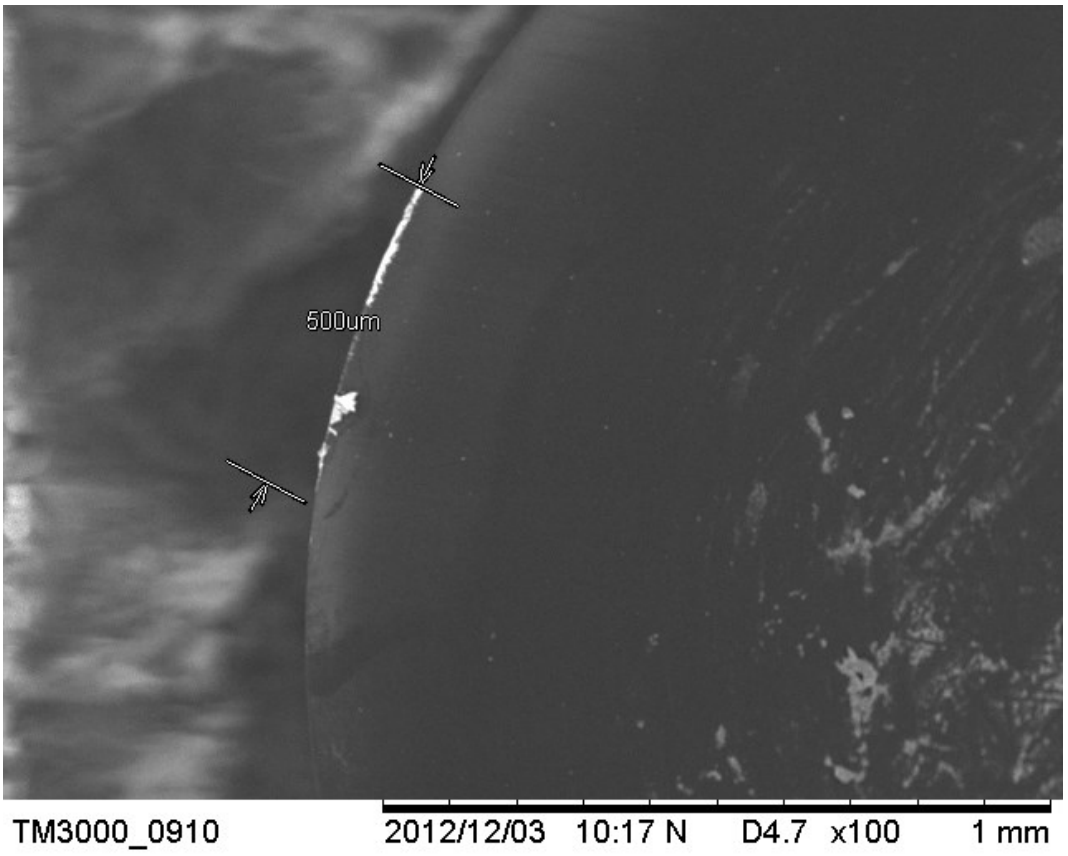

Figure 3.9 SEM image of Apex KC1.5mNEI tool after machining the BMG materials

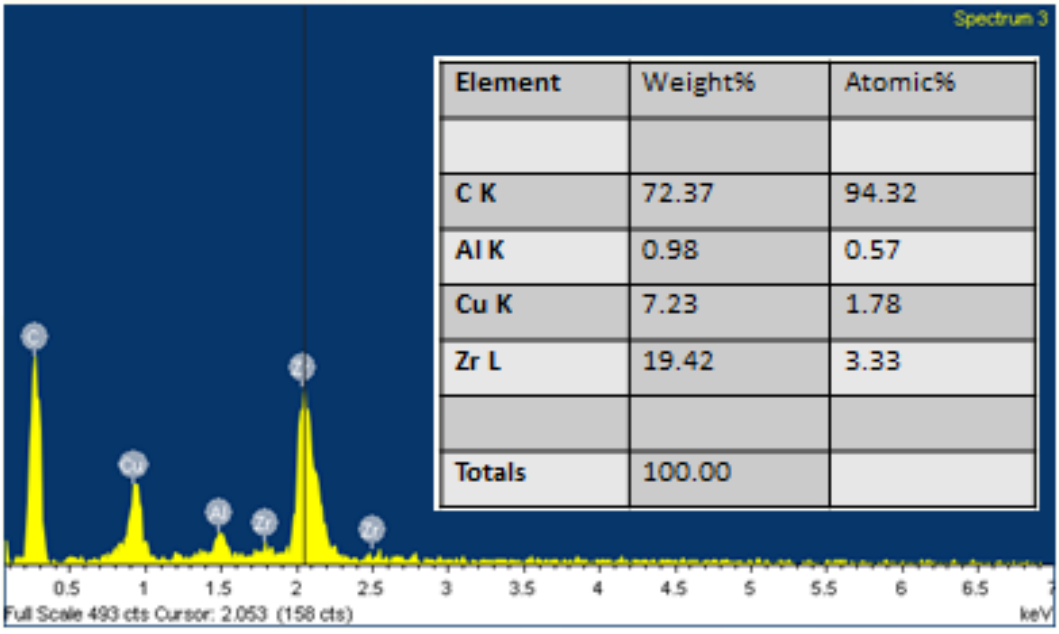

Figure 3.10 Result of SEM index test for the BUE

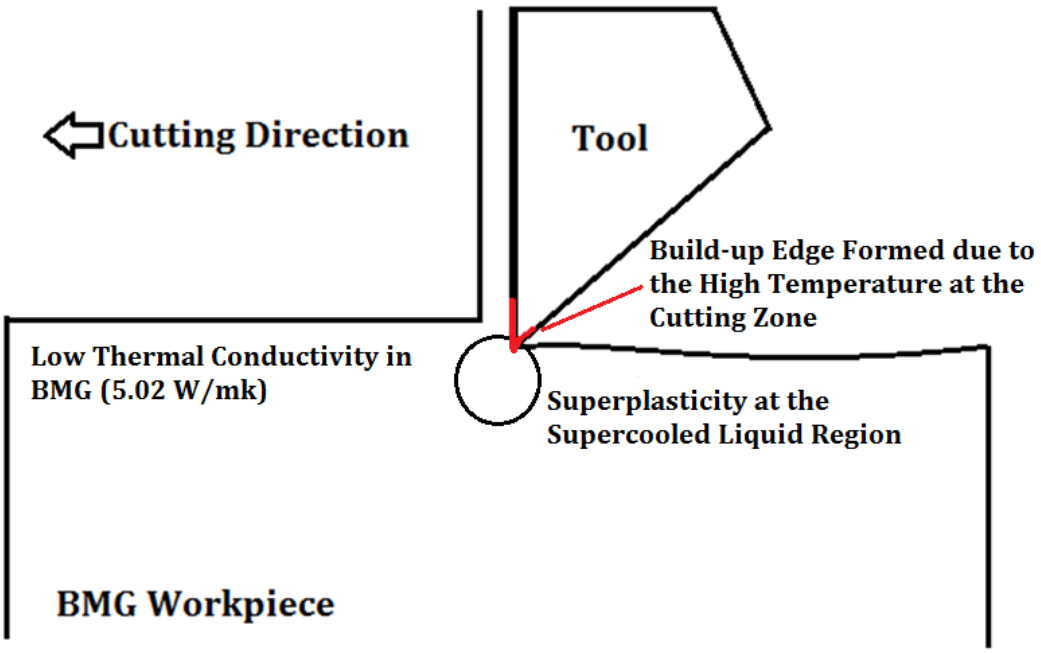

Figure 3.11 Graphical illustration of built-up material formation at tool edge in diamond cutting

3.7 Summary

The cutting characteristics of BMGs in the micro-cutting have been investigated in this chapter, including the microstructure change due to the machining, effect of the cutting parameters on the surface generation, and tool wear investigation. According to the XRD results, the atomic structure for the machined BMG is still amorphous in the diamond turning experiment.

The study on the effect on the cutting parameters on the surface generation have shown that the surface roughness is sensitive to the depth of cut and spindle speed due

to the swelling effect and built-up edge formed. Heat generation is believed to be achieved by the work done in plastic deformation and friction force. More heat energy is generated by increasing the depth of cut and cutting speed in diamond turning, and the temperature at the cutting zone is increased by the adiabatic system due to the low thermal conductivity of the BMGs. The high working temperature leads to a thermal softening effect on the BMGs, and the softening will increase the plasticity of the BMG. So the swelling effect becomes serious at high cutting temperatures. Besides, a built-up material formed on the diamond tool due to the thermal softening effecting in micro-cutting BMG, the SEM index test show that the compositions of the built-up material formed on the diamond tool match with the workpiece material. The built-up edge damage the machined surface because it increases the contact area between the work material and tool.

In addition, the best surface roughness achievement in SPDT BMG is 7.5 nm, under the optimum cutting parameters, with a feed rate of 5 mm/min, spindle speed 1000 rpm and depth of cut of 1 μm.

Chapter 4 Shear band morphology and nanocrystallization in micro-cutting of Zr-based bulk metallic glass

4.1 Introduction

Material behavior plays an important role in achieving stringent dimensional accuracy and stability of the machined surface due to the micrometer range of cut depths. There have been numerous studies of the cutting mechanism of single point diamond turning of non-ferrous materials, such as copper (Moriwaki, and Okuda, 1989), aluminum (Sugano and Takeuchi, 1987) and silicon (Nakasuji et al., 1990). Other than non-ferrous materials, bulk metallic glass has also been the subject of much research due to its excellent mechanical properties compared with traditional metals (Inoue, 2000). Bulk metallic glasses are alloys with an “amorphous” atomic structure, which results in the absence of crystallites, grain boundaries and dislocations (Sun and Wang, 2015; Ding et al., 2014; Shen et al., 2017). The amorphous structure provides unique properties including superior mechanical strain and hardness, excellent corrosion and wear resistance (Bakkal et al., 2004a), which lead to a potentially wide range of functional and high precision applications. However, BMG is a difficult to machine material due to its low thermal conductivity and high strength (Bakkal et al., 2004b).

Chapter 4 Shear band morphology and nanocrystallization in micro-cutting of bulk metallic glass

Some research works have been done for studying the machining mechanisms of BMGs to improve its machinability.

Bakkal et al. (2004c) reported that the cutting temperature in macro-machining Zr-based BMG can reacted to 2400-2700 K, which induced oxidation and crystallization of Zr-based bulk metallic glass. The unique lamellar chips were found in machining of bulk metallic glass. The lamellar chip formation is the integral results of the self-sustained limit-cycle phenomenon in stress, free volume and temperature in the primary shear zone (Jiang and Dai, 2009). Chen et al. (2017) reported the nano-crystallization phenomenon appeared at the machined surface in the micro-cutting of BMG, and, a mirror surface could not be achieved easily due to its viscous flow, the optimum surface roughness was reported as 100 nm.

The plastic deformation of amorphous alloys is generated due to the formation of highly localized shear bands in micro-cutting, which is induced by the serrated plastic flow (Chen, 1973). The initiation and the propagation of shear bands in Zr-based BMG under quasi-static and dynamic loading in compression have been investigated in depth (Liu et al., 2005). In addition, the effect of strain rate on the compressive failure strength was reported to decrease with an increase of strain rate (Li et al., 2003). It was reported in the literature that the plasticity of BMG is enhanced by the formation of multiple

shear bands in the process of quasi-static uniaxial compression testing (Liu et al., 2005). However, the nature of initiation and propagation of the shear bands of BMG under complex loading and boundary conditions during micro-cutting remain unclear. In addition, the presence of multiple shear bands in micro-cutting cannot be explained by the classical single-shear plane model for the micro-cutting of BMG.

The previous research on the microscopic material removal mechanisms in SPDT mostly focuses on the metallurgical properties and the machinability of crystalline materials, with little attention to the cutting mechanics of diamond turning amorphous metals such as BMG. However, the cutting characteristics in the micro-cutting of BMG have been studied. The study indicates that the surface roughness of a machined surface is sensitive to cutting speed therefore a relatively smooth surface can be obtained with low cutting speed, but no satisfactory explanation has been provided for this phenomenon (Chau et al., 2014). The nature of initiation and propagation of the multiple shear bands of BMG under complex loading and boundary conditions during micro-cutting remain unclear. The effect of the cutting speeds on the shear bands formation and propagation mechanisms in the micro-cutting of BMG have not been fully understood. To address the above issues, the morphological features of the primary deformation zone and their effects on surface roughness in the diamond cutting of Zr-

based BMG are investigated experimentally, and the crystallographic changes induced by the micro-cutting process at three different speeds are characterized through the study of high-resolution transmission electron microscopy in this study.

4.2 Experimental procedures

The material used for the experiment was $Zr_{55}Cu_{30}Ni_5Al_{10}$ amorphous alloy. Round bars of $Zr_{55}Cu_{30}Al_{10}Ni_5$ ingots 5mm in diameter and 70mm in length were prepared in arc melting furnace with copper mold under a high purity argon atmosphere. The amorphous nature of the fabricated BMG was verified by X-ray diffraction (RigakuSmartLab) with Cu-Kα radiation. The orthogonal micro-cutting tests of BMG were performed on a 4-axis ultra-precision machining system (Moore Nanotech 350FG, USA). The experimental setup is shown in figure 4.1a. The round bars of the BMG ingots were polished into a rectangular prism with 60 mm (length) x 1 mm (wide) x 4 mm (thick), and was mounted on a specially designed fixture for the micro-cutting. A monocrystal diamond tool with a 2-mm flat cutting edge, zero rake angle and 10° clearance angle was used in the straight cutting experiments. The tool moved in the Z direction with constant cutting speeds of 50 mm/min, 100 mm/min and 400 mm/min. The depth of cut was set at 7 μm, which allows a clear observation of shear bands formation in primary deformation zone in micro-cutting the BMG by SEM based on

the size of the deformation area. The cutting parameters are listed in table 7.

In the orthogonal micro-cutting test, the workpiece moved in the Z direction and the single point diamond tool was fixed in location. The diamond tool was quick-stopped at the center of the workpiece during orthogonal cutting; the chip was formed and remained attached to the workpiece surface after the tool retreated in the reverse cutting direction. The acceleration and deceleration of the machine tools is very crucial for the quick stop experiments. In the experiments, the experiment setup (Moore Nanotech 350) is working in fast move mode, the maximum allowable acceleration will be imposed on the slides. Although it is hard to exactly estimate the accurate acceleration and deceleration in the experiments, the sudden stop of the feeding slide can be indirectly validated by the experiment results of quick stop experiments, which might be attributed to the relative small cutting speed in the experiments.

These experiments were performed in a dry cutting condition to protect the chip morphology. In order to obtain the shear bands in the primary deformation zone after the micro-cutting, pre-machining was conducted on the surface parallel and perpendicular to the cutting direction by SPDT, which were labelled in figure 4.1a.

The serrated chips remained on the machined surface after the cutting process and were observed by scanning electron microscopy (Hitachi Electron Microscope

TM3000) along the normal direction of the side surface in order to examine the shear bands in the primary deformation zone and the chip morphology. 3D micrographs of the PDZ and machined surface at two different cutting speeds were further examined by an atomic force microscope (Park Systems XE-70 AFM). In addition, the surface roughness of the machined surface was determined by a 3D optical surface profiler (Zygo Nexview^{TM}). A field emission electron microscope (Jeol JEM-2100F STEM) was employed to investigate the microstructure changes in PDZ after the micro-cutting process. As figure 4.1b shown, the cross-section specimens of PDZ in the depth direction perpendicular to the machined surface were prepared by a focused ion beam (Quanta 200 3D DualBeam FIB) with surface coating protection by a sputter coater (Bal-tec SCD 005) using tungsten, with a thickness of 2 μm.

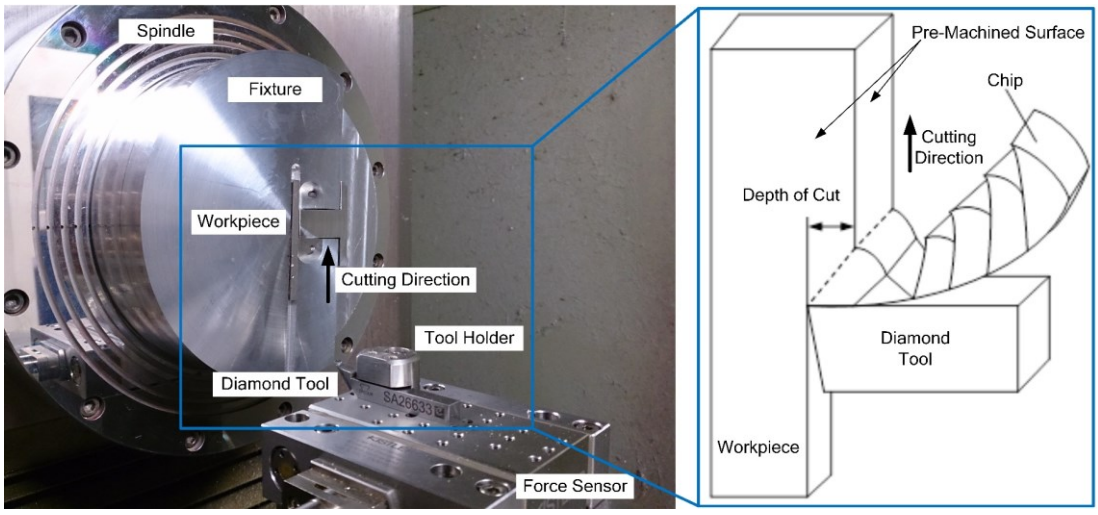

(a)

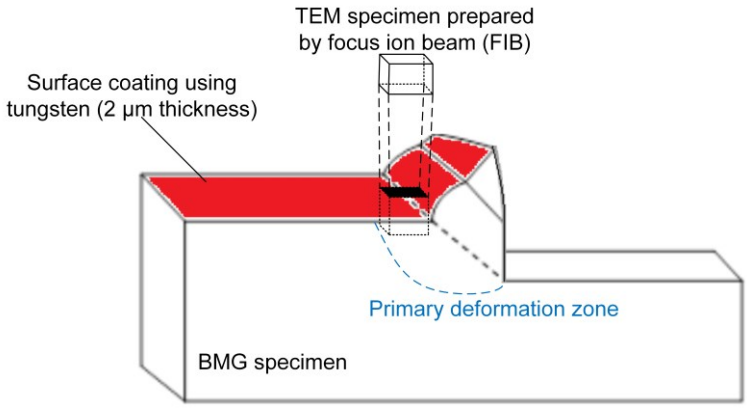

(b)

Figure 4.1 Experimental setup for (a) the straight cutting tests and (b) preparing the cross-section specimens of PDZ by FIB

Table 7 Cutting parameters of orthogonal micro-cutting

Parameters	Values
Cutting speed (mm/min)	50, 100, 400
Depth of cut (μm)	7
Tool type	Diamond tool
Rake angle of tool (°)	0
Clearance angle of tool (°)	10
Cutting environment	Drying cutting

4.3 Results and discussion

Figure 4.2(a) shows a scanning electron microscope micrograph of a continuous serrated chip generated in the straight cutting of the Zr-based BMG with the

diamond tool at 0° under a dry cutting condition. A series of slip-steps due to shear banding emerges along the cutting direction in the PDZ in micro-cutting BMG. The chip morphology in micro-cutting BMG is different from that appearing in crystalline metals, while the slip-steps cannot be obtained in micro-cutting crystalline metal, as shown in figure 4.2b (Wang et al., 2010). This formation and propagation of shear bands inside the PDZ generally cannot be obtained in machining crystalline materials. The formation of slip-steps revealed that the plastic deformation is highly localized within the PDZ in micro-cutting BMG. The plastic deformation behavior is fundamentally different between metallic glasses and crystalline materials due to the lack of long range order in metallic glasses. According to the free volume model developed by Spaepen (1977), when an external stress is applied and exceeds the activation energy for atomic jumping, the atoms jump into neighboring holes along the stress direction and create a free volume. With further atomic jumping, atomic flow and plastics flow in amorphous metals occurs. The increase in stress during micro-cutting promotes slip-steps and accommodates the plastic deformation in the cutting direction. When the accumulated stress reacts or excesses the yield stress of the work material, it will induce shear bands with a shear angle of 32°. The shear bands are either initiated at the free surface of the cutting specimen and then propagate to the cutting edge of the tool or are initiated at

the cutting edge of the tool and then propagate to the free surface in the PDZ, as shown in the enlarged view (yellow square) in figure 4.3 (a). The experimental results indicate that the amorphous alloy experiences deformation behavior in the micro-cutting process.

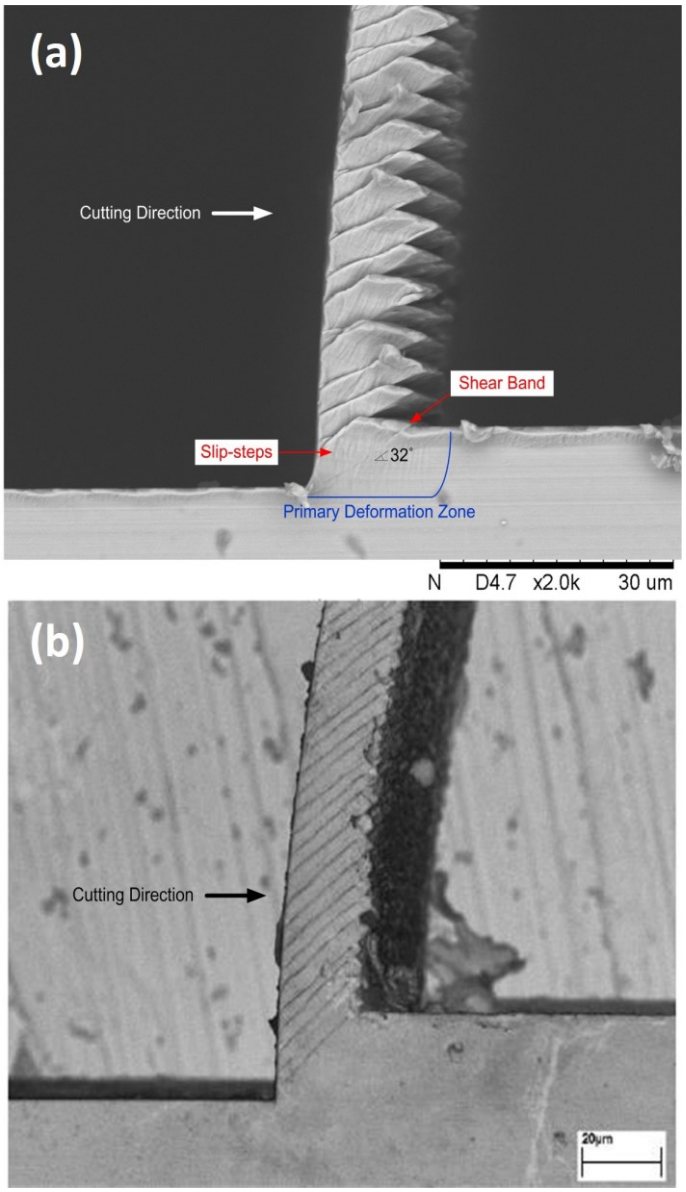

Figure 4.2 SEM micrograph of chip morphology in micro-cutting (a) Zr-based BMG and (b) cold-rolled brass with a diamond tool at a rake angle of 0° (Wang et al., 2010)

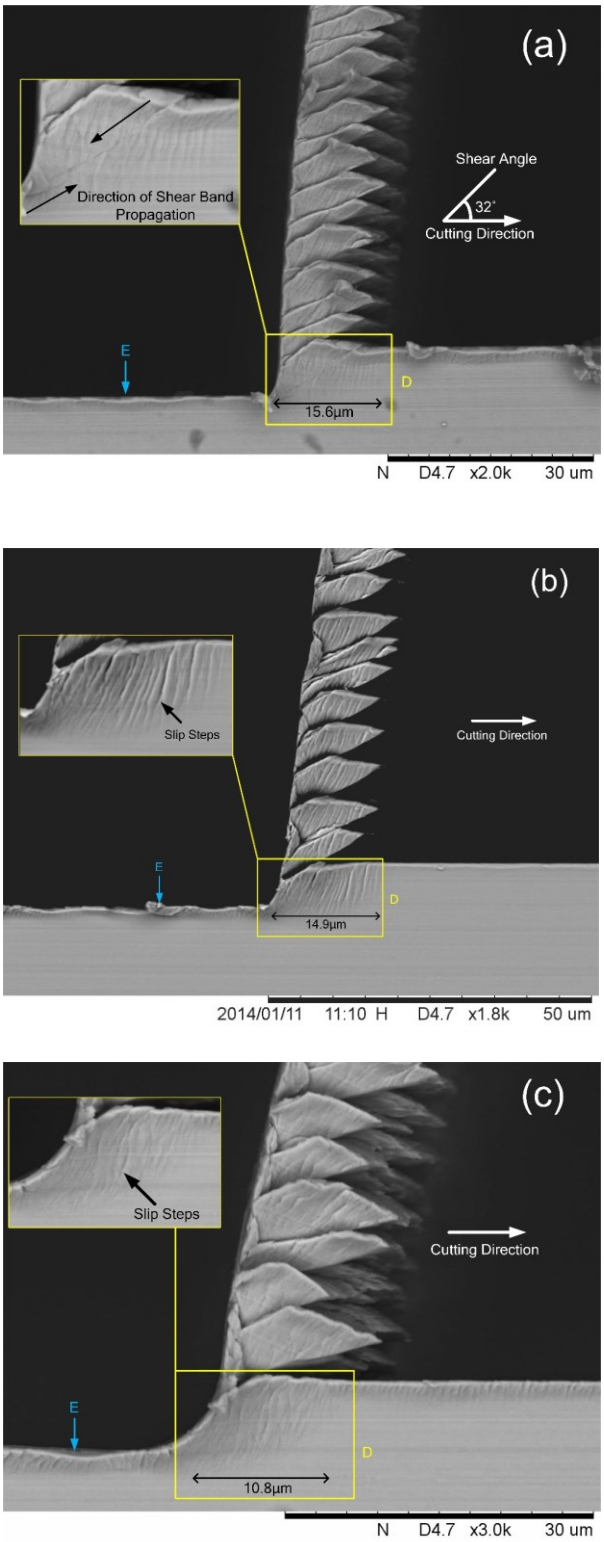

Figure 4.3. SEM images for primary deformation zone in straight cutting Zr-based BMG with cutting speed at (a) 50 mm/min, (b) 100 mm/min and (c)400 mm/min.

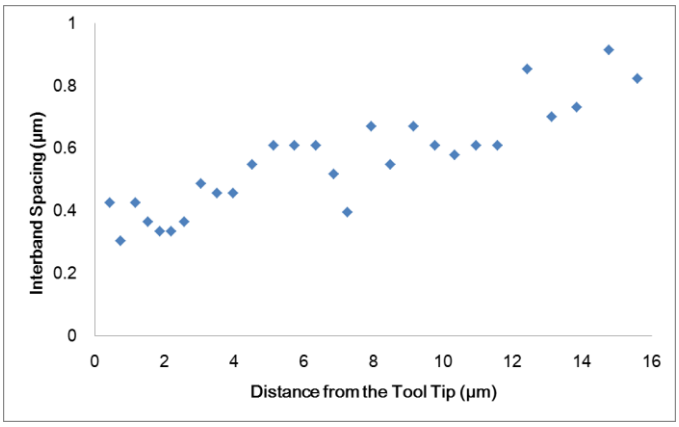

(a)

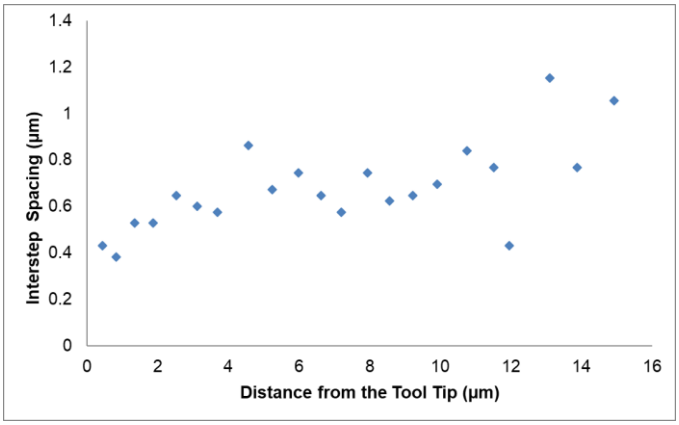

(b)

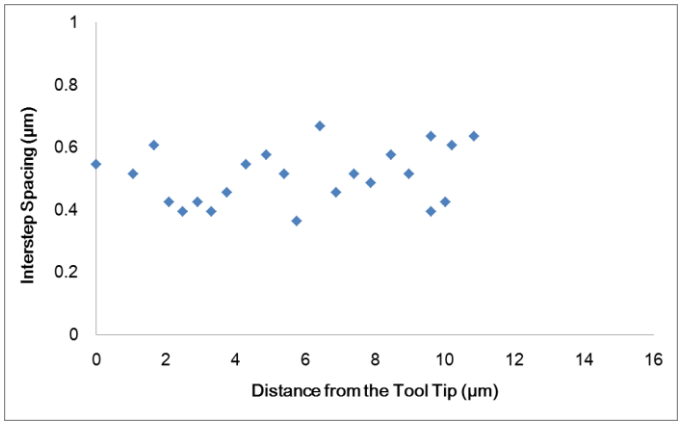

(c)

Figure 4.4. Variation of the inter-step spacing as a function of distance from the tool in straight cutting Zr-based BMG with cutting speed at (a) 50 mm/min, (b) 100 mm/min and (c)400 mm/min.

To observe the influences of cutting speed on surface roughness and the chip morphologies, the depth of cut was set at 7 μm, with cutting speeds of 50, 100 and 400 mm/min accordingly. Figure 4.3 shows the morphologies of the PDZ (site D) of the specimen after diamond cutting at the three different cutting speeds. The corresponding chip morphologies and formation of multiple slip-steps at different cutting speeds are visible in the SEM images. Serrated chips were observed at the three different cutting speeds, and the length of the slip-steps in the PDZ and the area of PDZ are shown in table 8. Figure 4.4 illustrates the inter-band spacing for the slip-steps formed in the PDZ as a function of the distance from the cutting tool tip at cutting speeds of 50 mm/min, 100 mm/min and 400 mm/min. For the test at a cutting speed of 50 mm/min, 100mm/min, the inter-step spacing increased when the distance between the tool tip and that inter-step spacing increased. The lowest value of the distance of the inter-step spacing in cutting speed of 50 mm/min was 0.3 μm and increased to 0.9μm over a distance of 15.6 μm. For the test at a cutting speed of 100 mm/min, the lowest value of the inter-step spacing was 0.4 μm and increased to 1.2 μm over a distance of 14.9 μm. For the test at a cutting speed of 400 mm/min, the inter-spacing showed considerable scatter which was consistent with the irregular shapes of the shear band formation. Furthermore, for sample 1, there was a linearly increase in spacing with an increase of

the distance from the tool tip. It was similar to the observation reported by Xie et al. (2008), in which the inter-spacing of the shear bands in $Zr_{41}Ti_{14}Cu_{12.5}Ni_{10}Be_{22.5}$ BMG under Vickers indentation was proportional to the distance from the tip. This result indicates that the formation of primary shear bands in a micro-cutting process is similar to that in the other indentation processes, in which the primary shear bands are firstly initiated at the region around the tool tip and then accommodate the plastic deformation in the cutting direction and appear as slip-steps in PDZ. On the contrary, for sample 3, irregular shapes and scatter spacing of the slip-steps were generated, illustrating the inhabitations of growth and propagation of the slip-steps within a short period by the local stress. However, the present work showed that the total length and the area of PDZ increased significantly by decreasing the cutting speed.

The enlarged view of the PDZ in figure 4.3(a) shows that the slip-steps are parallel to each other and fully developed with no intersect, at a cutting speed of 50 mm/min. Most of the slip-steps remain parallel to each other and fully developed when there are few irregular slip-steps can be found at a cutting speed of 100 mm/min. When the cutting speed increased from 100 mm/min to 400 mm/min, more irregular slip-steps can be found in PDZ, the slip-steps develop rapidly and irregularly within the PDZ due to the severe plastic deformation. At a low cutting speed, there is sufficient time for the

shear bands to release the built-up stresses and avoid crack formation. In contrast, the built-up stresses do not have sufficient time to relax at relativity high cutting speed, which leads to crack formation and a brittle fracture mode. Figure 4.5 shows the surface topologies and surface roughness of the machined surface. The arithmetic roughness of the machined surface was examined by the 3D optical surface profiler, as shown in table 8. The arithmetic roughness value, R_a, is the arithmetic average of the absolute values of the profile height deviations from the mean line, recorded within the evaluation length, and can expressed as equation 4.1. The Ra values were 13 nm, 25nm and 47 nm at cutting speeds of 50, 100 and 400 mm/min respectively. The R_a values were increased with increasing the cutting speed.

$$R_a = (1/L) \int_0^L |y - y_m| dL \quad (4.1)$$

where L = evaluation length,y = the profile height and y_m is the height of the mean line.

Table 8 Summary of shear bands transformation distance and interval

Sample ID	Cutting speed (mm/min)	Arithmetic roughness R_a (nm)	Length of primary deformtion zone (μm)	Area of primary deformtion zone (μm^2)	Number of slip-steps
1	50	15	15.6	127.3	28
2	100	25	14.9	113.6	23
3	400	43	10.8	95.8	23

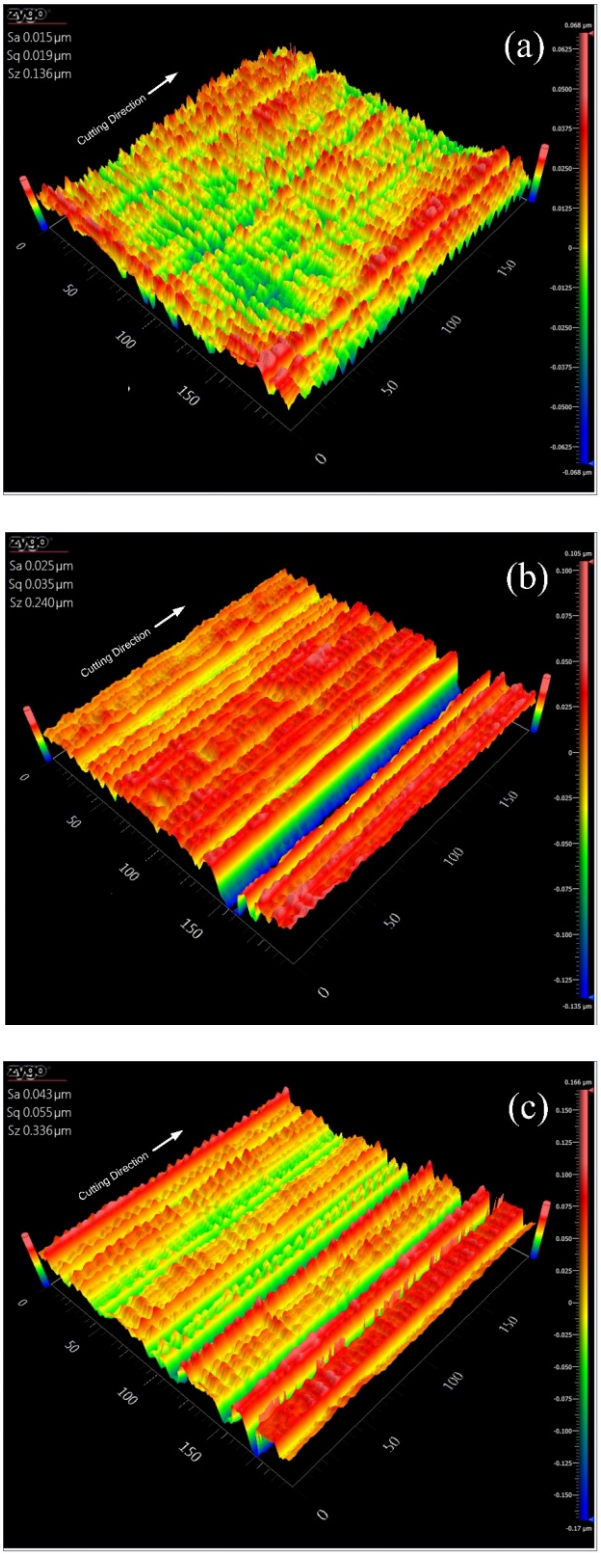

Figure 4.5 Surface topologies of Zr-based BMG after straight cutting (site E) in cutting speed (a)50 mm/min, (b) 100 mm/min and (c) 400 mm/min

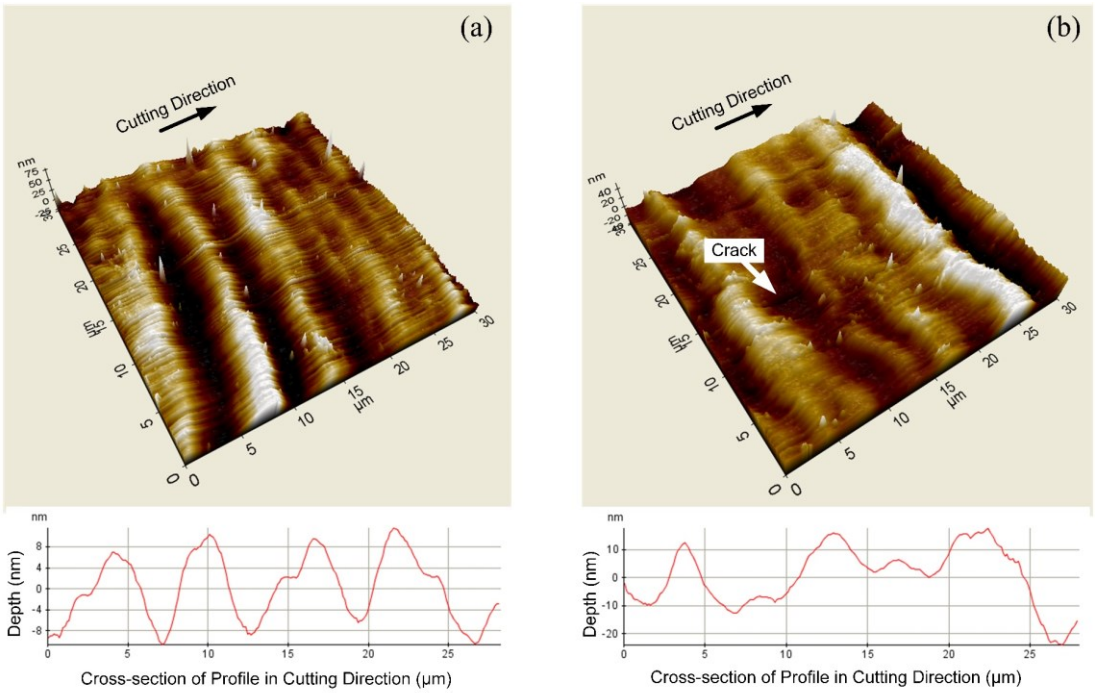

Figure 4.6 AFM images of machined surface of Zr-based BMG after straight cutting (site E) in cutting speed at (a)50 mm/min and (b) 400 mm/min

In order to compare the effect of different cutting speeds on the machined surface, the machined surface of the higher and lower cutting speeds (400 mm/min and 50 mm/min) in this study are examined by an Atomic Force Microscopy (AFM). The scan range was set at 30μm×30μm, and the result is shown in figure 4.6. The AFM images in figure 4.6(b) show the morphologies of the machined surface, in which some scratches were found on the machined surface due to the crack formation. The cross-sectional profiles show that the maximum peak to valley height value of sample 1 is

about 23nm while maximum peak to valley height value of sample 3 is over 35 nm. The AFM results show that the depth and the period of the grooves in the diamond-turned BMG sample 1 were more regular than those in sample 3. The high loading rate in the micro-cutting process cannot provide sufficient time for the slip steps nucleation and propagation, and the plastic strain cannot be released by the formation of slip step, the number of slip steps and the total length of the PDZ is decreased by increasing cutting speed. Irregular slip-steps can be found in PDZ due to the severe plastic deformation in higher cutting speed. The irregular shapes and scatter spacing of the slip-steps in cutting speed at 400mm/min inhibit the shear band propagation in PDZ, which generate a non-linear shear bad propagation in micro-cutting BMG. This non-linear shear band propagation leads to an irregular geometry shape which extends from the primary deformation zone to the area under the tool tip. An irregular and unpredictable profile of the machined surface resulted in the high-speed micro-cutting. The results suggest that the periodic grooves on the machined surface are associated with the serrated chips with regular slip-steps spacing, the formation of regular shear bands supporting the redistribution of the plastic strain and the prevention of crack formation.

The microstructural feature at the PDZ was analyzed by TEM. Figure 4.7 (a) and (b) show the cross-sectional transmission electron microscopy (XTEM) images and

selected area diffraction (SAD) patterns of the PDZ in sample 1 and sample 3 respectively. A homogenous maze contrast was observed, and no crystalline structure could be seen in figure 4.7(a). In figure 4.7(b), the XTEM image and the SAD pattern revealed that there were precipitations of nanocrystalline particles randomly distributed within the PDZ with an average size in a range of 10-15 nm. In contrast, figure 4.7(c) shows the HRTEM image of machined sample 1 containing shear bands (region 1), where the PDZ (region 2) and the SAD patterns indicate that the nanocrystals only grow inside the shear bands at low cutting speed, with an average size of 3-4 nm.

The local heating accompanies the severe localization of plastic flow into shear bands in the Zr-based metallic glass during deformation, which generates a temperature change from 278 K to more than 1273 K (Thurnheer et al., 2016). According to the molecular dynamic simulation, an increase of temperature in the shear bands of CuZr metallic glass is correlated positively with strain rate under tensile loading (Tang et al., 2018). However, the molecular dynamic simulation results showed that the cutting temperature of $Zr_{-50}Cu_{30}$ metallic glasses can reach to 600-700K in the nanoscale cutting process (Zhu et al., 2014). During the deformation process, the temperature was raised by localized adiabatic heating inside the shear bands, playing a crucial role in the nanocrystallization process (Lewandowski and Greer, 2006; Kim et al., 2002). The

temperature of the PDZ in the micro-cutting BMG could reach or exceed the transition temperature (T_g) due to the low thermal conductivity of the $Zr_{55}Cu_{30}Ni_5Al_{10}$ BMG, while the T_g of the $Zr_{55}Cu_{30}Ni_5Al_{10}$ BMG was 673 K (Vaillant et al., 2002). Thus, the nanocrystallization process can occur at the PDZ in the micro-cutting process.

The results show the mechanism of the formation of nanocrystalline particles with the propagation of primary and secondary shear bands within the PDZ in a micro-cutting process under various cutting speeds. Figure 4.8 shows a graphical illustration of the above-mentioned mechanism. It is noticeable that the shear band initiation and propagation of the micro-cutting process are highly related to the cutting speed. In the initial stage, a part of local stress would be released by the formation of slip-steps along the cutting direction (figure 4.8(a1) and (b1)). Once the remaining local stress accumulated to the yield point, then the shear band would be initialized and propagated in the PDZ. The results from the SEM images indicate that a relatively low speed in micro-cutting would benefit in regard to the formation of shear bands, because of the slight increase in the local stress at relatively low cutting speeds in micro-cutting, the local stress could be released by the full development of the slip-steps before the shear bands was initiated. At a lower cutting speed in micro-cutting BMG, it provided sufficient time to nucleate new slip steps from the tool tip to cutting direction, and the

fully developed slip steps could be observed at a larger PDZ area. The shear bands were rapidly initiated to accommodate the large inelastic strain due to a high rate of energy input. The number of slip steps and the PDZ area was relatively smaller in high speed cutting since the slip-steps in PDZ cannot be fully developed before the shear band initialed. With increase of cutting speed, the time is reduced for conducting the heat generated by cutting, and the temperature in the PDZ rises rapidly. The high rate of loading inhibits the formation of slip-steps which generate more heat and thereby raise the temperature in the PDZ due to the low thermal conductivity of BMG. The presence of nanocrystals outside the shear bands at higher cutting speed indicated that the large shear strain at high rate loading affects the amorphous matrix. Hence, the machining-induced nanocrystallization process is influenced by the cutting speed in micro-cutting BMGs.

By the precipitation of nanocrystals outside the shear bands at high speed cutting, the propagation of the shear band is suppressed by the nanocrystaline particles. Then, a new shear band would be initiated at an area near the previous corresponding shear bands. As illustrated in figure 4.8(b2), repeating the process during cutting process, the shear bands are propagated in a non-linear way due to the random distribution of nanocrystaline particles in the PDZ. This non-linear shear band propagation leads to an

irregular and unpredictable profile of the machined surface in high-speed micro-cutting, as shown in figure 4.6(b).

Furthermore, the elastic strain energy in the cutting direction can be absorbed by the formation of slip-steps at low cutting speed. Conversely, the high load rate does not provide sufficient time for the formation of slip-steps; thus, the elastic strain energy in the PDZ leads to material recovery in the region between the tool tip and material. Multiple intersecting residual shear bands in the form of wrinkles and microcracks can be observed on the machined surface in high-speed cutting, as shown in figure 4.6(b), which was a result of the high elastic energy stored in the PDZ. Therefore, a smoother surface with regular grooving can be obtained at a low cutting speed. This result also implies that the high loading rate in micro-cutting a BMG enhances the formation of nanocrystals on the machined BMG surface.

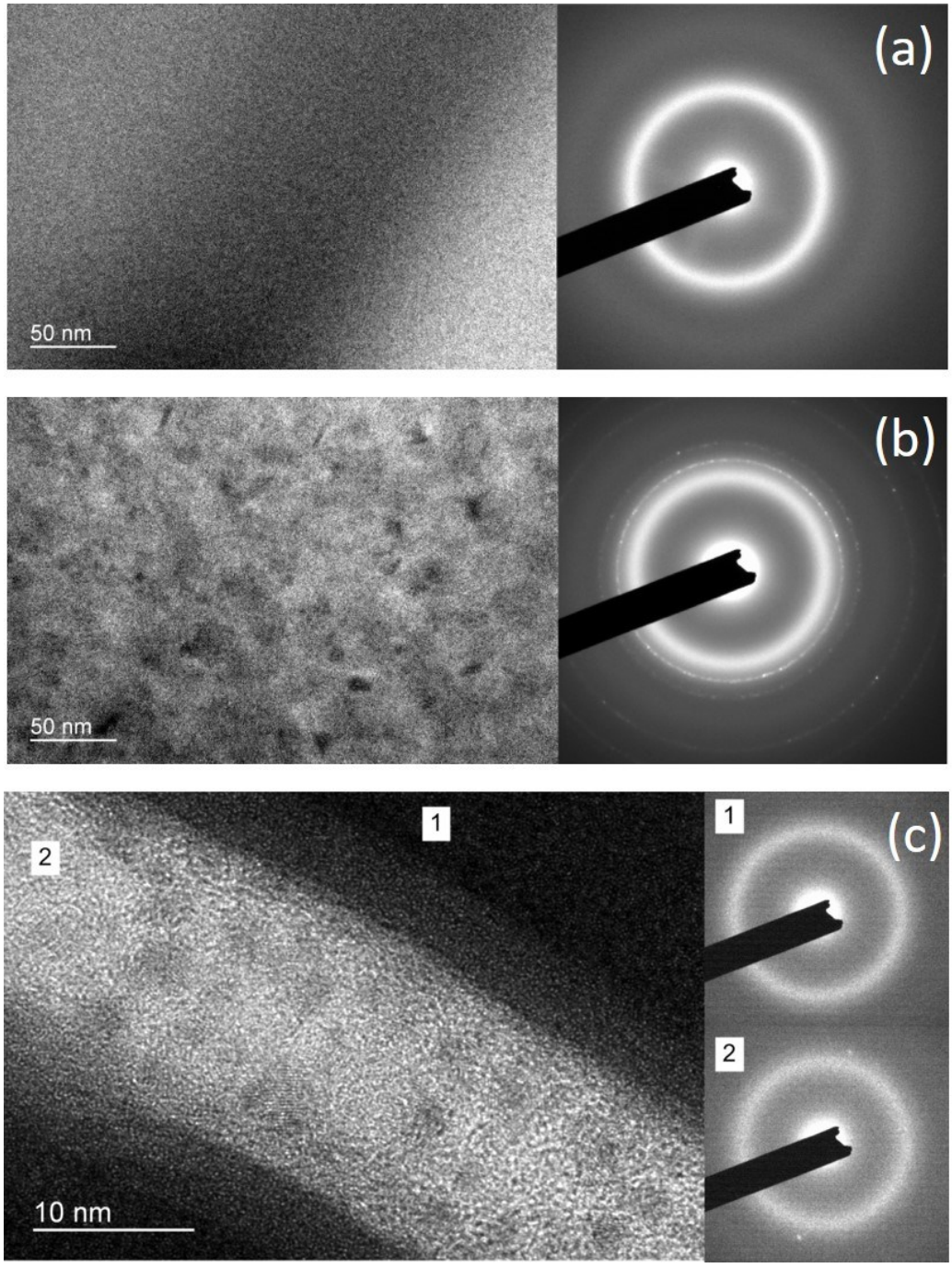

Figure 4.7 XTEM image of primary deformation zone in (a) sample 1 and (b) sample 2; (c) HRTEM image and SAD patterns of the shear bands formed in sample 1

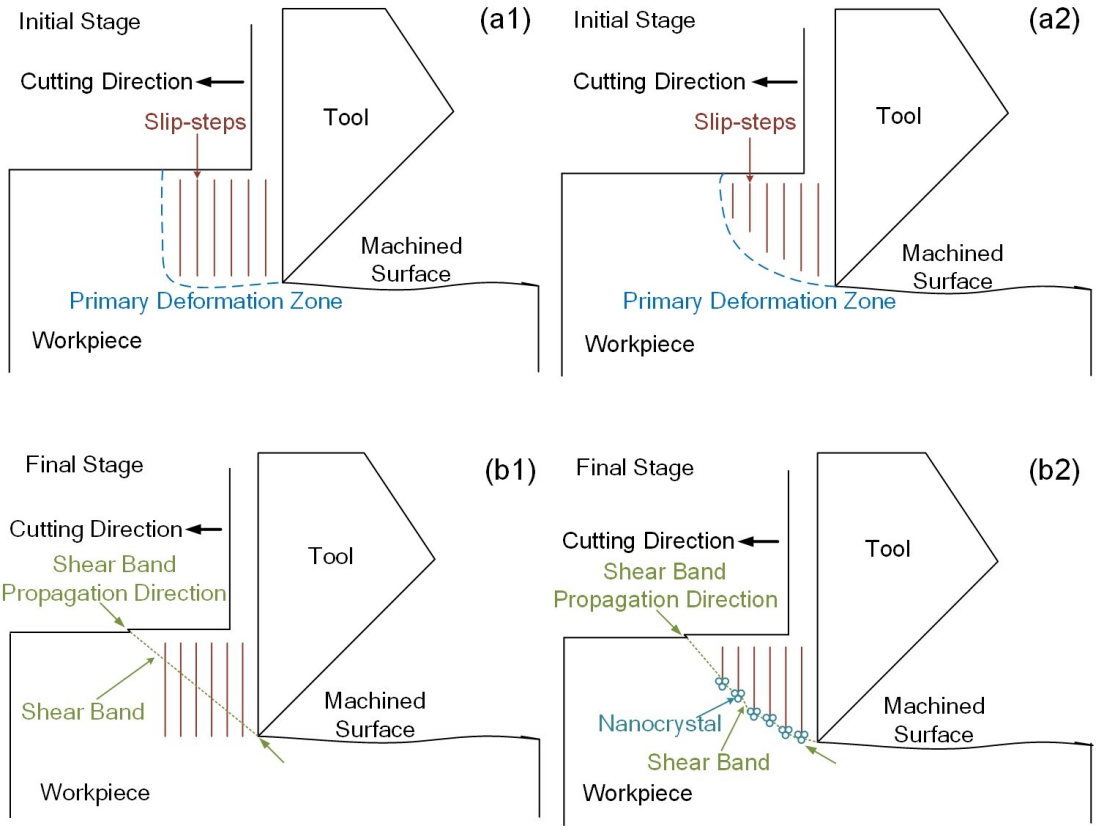

Figure 4.8 Graphical illustration of formation and propagation of shear band in microcutting Zr-based BMG. (a1) and (a2): The formation and propagation of primary shear bands at initial stage. (b1) and (b2): The formation and propagation of secondary shear bands at final stage. Note that for (a1) and (b1): cutting speed 50 mm/min, and for (a2) and (b2): cutting speed 400 mm/min

4.4 Conclusions

This study investigated the formation of multiple shear bands in the micro-cutting of a Zr-based BMG at two cutting speeds. Firstly, continuous serrated chips appear in straight cutting the Zr-based BMG with a diamond tool. When observing the

serrated chips, a series of slip-steps could be seen in the cutting direction at the PDZ and within the serration, while the slip-steps cannot be obtained in micro-cutting crystalline metal. The effects of the cutting speeds on the shear bands formation and propagation mechanisms in the micro-cutting of BMG have been observed. The observations shown the formation and propagation of shear bands in micro-cutting BMG are influenced by cutting speed, a higher cutting speed inhibits the growth and propagation of shear bands in the primary deformation zone.

Secondly, the effects of shear bands formation and propagation on the machined surface quality have been studied. A finer machined surface is associated with the serrated chips with regular slip-steps spacing, the formation of regular shear bands supports the redistribution of the plastic strain and the prevention of crack formation.

The TEM examination in the primary deformation under various cutting conditions revealed that the micro-cutting-induced nanocrystallization occurred in micro-cutting of BMG. Nanocrystalline practices were found inside the shear band at a cutting speed of 50 mm/min, while nanocrystals were seen outside the shear bands at a cutting speed of 400 mm/min. These results indicated that the formation of the nanocrystal in the micro-cutting process is influenced by the cutting speed.

The mechanism of the formation and propagation of shear bands in micro-cutting

Chapter 4 Shear band morphology and nanocrystallization in micro-cutting of bulk metallic glass

Zr-based BMG under various cutting speed was proposed. The high load rate inhibited the formation of the shear bands. The propagation of the shear bands was suppressed by the nanocrystalline practices in the PDZ. The interaction between the shear bands propagation and the formation of nanocrystalline practices can affect the surface generation in the micro-cutting of BMG. The non-linear propagation of the secondary shear band leads an irregular and unpredictable profile of the machined surface.

.

Chapter 5 Twinned-serrated chip formation with minor shear bands in ultra-precision micro-cutting of bulk metallic glass

5.1 Introduction

Bulk metallic glass exhibits of excellent performance, such as high strength and hardness, large elastic limit and superior resistance to wear and corrosion, as compared with traditional metals (Bakkal et al., 2004a). Due to its unique physical, chemical, and mechanical properties, it has received intensive and increasing interest. Machining is a commonly employed cost-effective process for generating a required shape, however, BMG is a difficult to machine material due to its low heat conductivity and high strength (Bakkal et al., 200b), which limit its applications.

To improve its machinability, research work has been carried out to study its machining mechanisms. Huang and Yan (2016) studied crystallization behavior at the workpiece surface layer of a Zr-based BMG during micro-electrical discharge machining, using X-ray diffractometer and laser micro-Raman spectroscopy. The surface crystallization layer was effectively removed by subsequent grinding using a sintered polycrystalline diamond. The combined machining process is a promising

method to fabricate micro-features on the BMG surfaces. Bakkal et al. (2004c) suggested that machining induced oxidation and crystallization of Zr-based bulk metallic glass, since the cutting temperature was very high, up to 2400-2700 K. Additionally, Jiang and Dai (2009) found that unique lamellar chips were formed in the machining of bulk metallic glass. The lamellar structures generated during chip formation are the combined results from the self-sustained limit-cycle phenomena in stress, free volume and temperature in the primary shear zone. Fujita (2005a) suggested that the slipping off generation mechanism of the lamellar chips was the reason for the excellent machinability in the turning of Zr-based BMG. However, Bakkal (2004a) proposed that the cyclic shear band formation would aggravate surface quality. In addition, the drilling performance of BMGs has been studied extensively, and Zhu et al. (2013) observed the serrated chip formation in drilling a Zr-based BMG. They found that the nano-crystals present in the drilling of Zr-based BMGs facilitated the chip serration formation. Bakkal (2005b) reported that drilling BMGs at high speed would yield a light emission and severe tool wear during chip formation. More importantly, it was found that there was a feasible spindle speed and feed rate for efficient of drilling BMGs. The serrated chip formation was s key characteristics in drilling BMGs.

Furthermore, ultra-precision micro-cutting has been well established for the

precision fabrication in mass production, providing sub-micrometric form accuracy and nanometric surface roughness (Zhang et al, 2015). As a potential material, much more attention has been initially paid to UPMC of BMG. Chen (2017) reported nano-crystallization and serrated chip formation of the BMG were frequently formed in UPMC. A mirror surface could not easily be achieved due to its viscous flow, and the lowest achievable surface roughness was only 100 nm. Han (2015) suggested that the serrated chips formation in the UPMC of BMG was due to the inhomogeneous localized maximum shear stress in nano-scratching.

As discussed above, current research work on machining of BMG reveals that the machined surface of BMG is usually characterized by crystallization and its chips are uniquely serrated in nature. Chip formation is an important indicator for surface quality and tool wear in machining (Huang and Yan, 2016). However, the intrinsic serrated chip formation mechanisms are not fully understood. Motivated by this, in this research, a series of orthogonal cutting tests were carried out to study the unique chip formation in UPMC of BMG. The chip morphologies were observed by a scanning electron microscope and the cutting forces were measured by a cutting force measurement system. In addition, the effects of tool rake angle on chip formation were determined. Furthermore, finite element modelling was employed for the orthogonal UPMC

simulation to reveal its intrinsic mechanisms, since it is a powerful tool which used to study complex cutting mechanisms (Chen et al., 2013; Özel, 2006; Mahnama and Movahhedy, 2010).

5.2 Experimental setup

The material bulk metallic glass, $Zr_{55}Cu_{30}Al_{10}Ni_5$, was used in this study. Round bars of $Zr_{55}Cu_{30}Al_{10}Ni_5$ ingots 5mm in diameter and 70mm in length were prepared in arc melting furnace with a copper mould. The amorphous structure of as-cast Zr-based BMG was characterized by X-ray diffraction (RigakuSmartLab), using CuKα radiation, as shown in figure 5.1. The physical properties of the bulk metallic glass ($Zr_{55}Cu_{30}Al_{10}Ni_5$) are listed in table 9, and effect of the temperature on the physical properties shown in table 9 are neglected in this study. The orthogonal UPMC tests of BMG were performed on a 4-axis ultra-precision machine Moore 350FG. Details experimental setup of the orthogonal UPMC are shown in figure 5.2. The round bars of the BMG ingots were polished into a rectangular prism with dimensions 60 mm (length) x 1 mm (wide) x 4 mm (thick), and the workpiece was mounted on a fixture for ultra-precision machining. In the UPMC test, the workpiece moved in the Z direction and the single point diamond tool was fixed. To measure cutting forces, a Kistler 9252A force

transducer was mounted between the tool shank and the tool fixture, with a pre-loaded force to sense the cutting forces. The signals of the cutting forces were recorded using a Tektronix TDS 774A digitizing oscilloscope after being pre-amplified by a charge amplifier. The sampling frequency was set at 1 MHz. And the chips' morphologies were observed by the scanning electron microscopy (Hitachi TM3000). The detailed cutting parameters are listed in table 10. The radius of the diamond tool, measured by an atomic force microscope, was 20 nm.

Table 9 Physical properties of bulk metallic glass at room temperature (300K)

Properties	Values
Density (kg/m^3)	8620
Hardness (HRC)	46
Elastic modulus (GPa)	85
Thermal conductivity (W/mK)	5.02
Specific heat capacity ($Jmol^{-1}K^{-1}$)	26.5
Poisson’s ratio	0.376
Linear thermal expansion ($10^{-6}/^oC$)	6.5

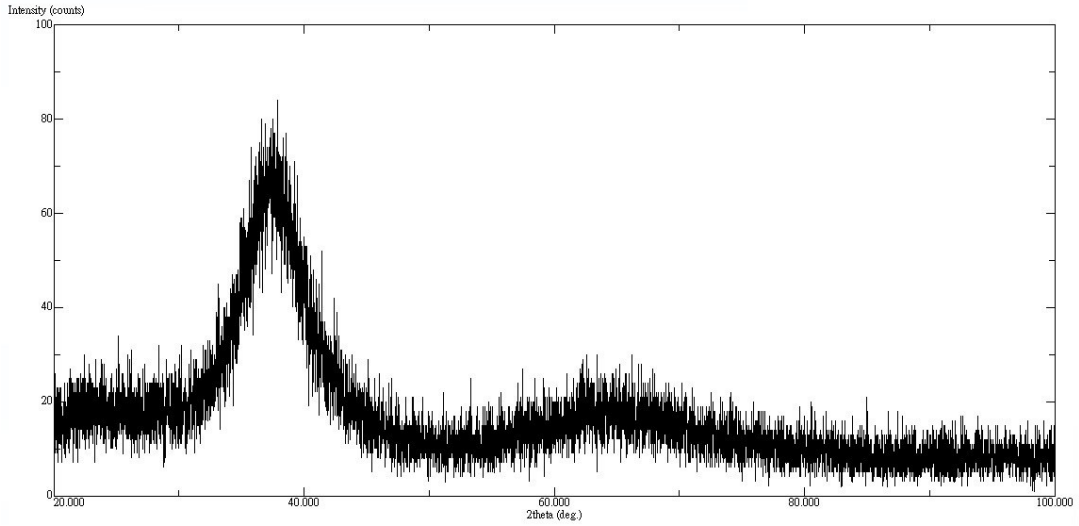

Figure 5.1 Characterization of as-cast $Zr_{55}Cu_{30}Al_{10}Ni_5$ bulk metallic glass by XRD

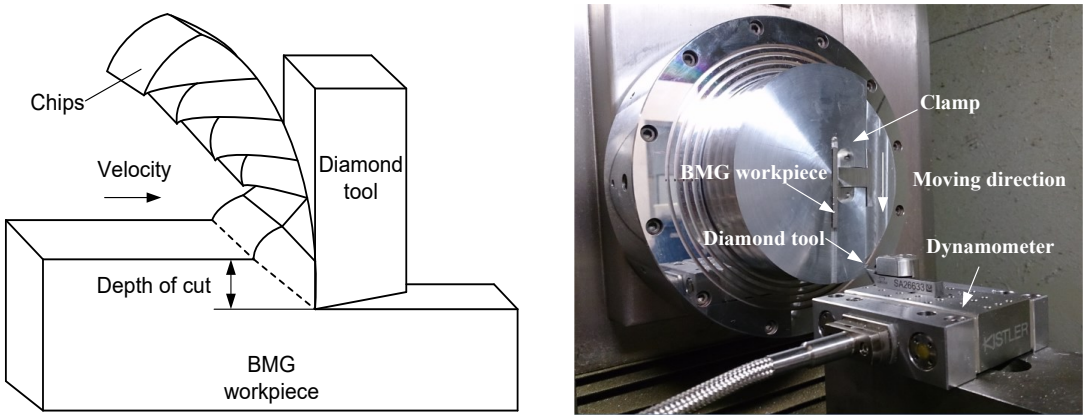

(a) Schematic of orthogonal UPMC (b) Equipment of orthogonal UPMC

Figure 5.2 Tests of UPMC for BMG

Table 10 Cutting parameters of UPMC

Parameters	Values
Cutting speed (mm/min)	100
Depth of cut (μm)	7
Tool type	Diamond tool
Rake angle of tool (°)	5, 0, -10, -25
Clearance angle of tool (°)	10
Cutting environment	Drying cutting

5.3 FEM in UPMC of BMG

To identify the material soft behavior due to the adiabatic effect in UPMC of BMG, FEM was employed to obtain information on the chip formation. In this study, the software ABAQUS 6.12 was used to simulate the orthogonal UPMC of BMG. To reflect the adiabatic effect in UPMC, the analysis step "Dynamic, Explicit, adiabatic" was selected in the software. The orthogonal FEM for the UPMC of BMG is shown in figure5.3. In the simulation, the part dimension was 90 μm x 30 μm, and the part was meshed with 24,800 elements, of bilinear quadrangular form with reduced integration and hourglass control: CPE4R. In order to improve the accuracy, the mesh in the cutting layer was refined. The tool was set as a rigid-body with 1200 elements. The boundary

conditions are shown in figure 5.3, the cutting tool is considered as fixed in x and y directions. The workpiece material is fixed at y direction and it is moved against the tool by applying a constant cutting velocity.

The FEM simulation in this study were performed on a desktop computer with 4-core Central Processing Unit (CPU), Intel® Core™ i7-5775C processor, 64GB Random Access Memory (RAM), and a Graphics Processing Unit (GPU), NVIDIA GeForce GT 730 GPU. Each cutting parameters were undergoing the FEM simulation in one times. It took approximately 72 hours for each model.

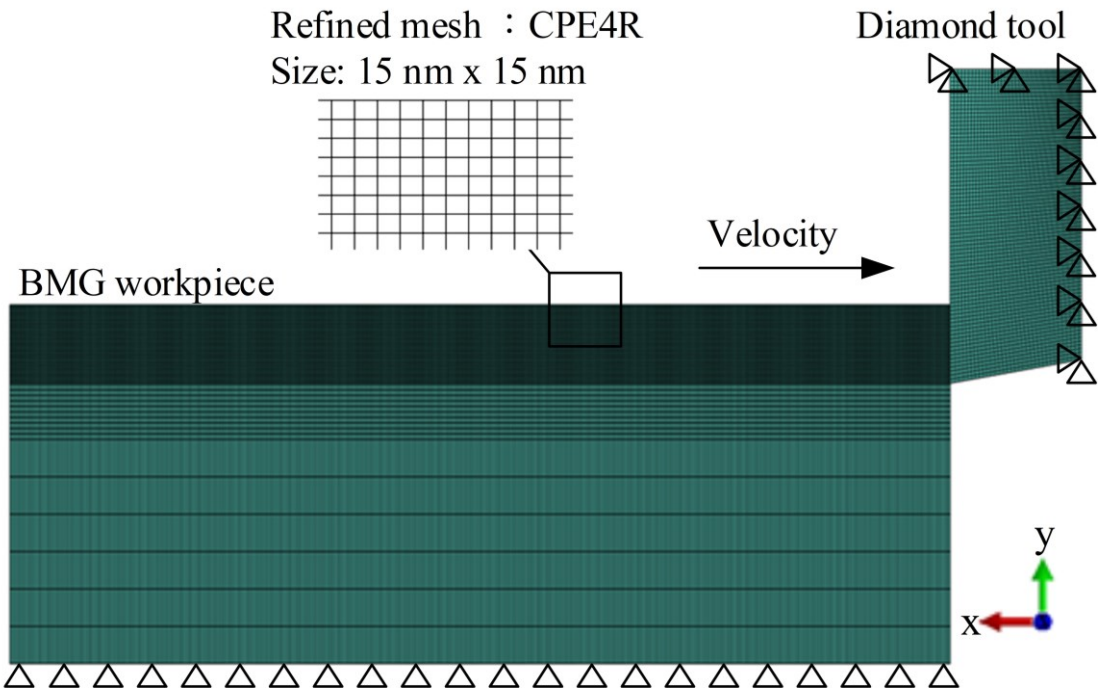

Figure 5.3 Orthogonal FEM in UPMC of BMG

5.4 Description of the Johnson-Cook material model

The Johnson-Cook constitutive model (Johnson and Cook, 1983) describes the flow stress of a material by considering the effects of strain hardening, strain-rate and thermal softening. This plasticity model is suitable in FEM simulation of materials at high strain rates and the cutting process. The Johnson-Cook model is found effective in modeling the cutting force, temperature and chip morphology in machining process (Vijay Sekar and Pradeep Kumar, 2011). In this study, the Johnson-Cook material law was adopted in the simulation of UPMC for BMG, and it was employed to study the phenomenon of BMG under the conditions of the large deformation, high strain rate and high temperature

The Johnson-Cook material model was the following equation:

$$\sigma_e = \left[\mathrm{A} + \mathrm{B}(\varepsilon_e^p)^n\right][1 + C ln\, \dot{\varepsilon}^*][1 - T^{*m})] \quad (5.1)$$

where σ is the equivalent stress, and ε is the equivalent plastic strain. $\dot{\varepsilon}^* = \frac{\dot{\varepsilon}}{\dot{\varepsilon}_{ref}}$ is the relative equivalent plastic strain rate. $T^* = \frac{T - T_{ref}}{T_m - T_{ref}}$ is the homologous temperature, T_m is the melting temperature., and $\dot{\varepsilon}_{ref}$ and T_{ref} are the reference strain rate and the reference deformation temperature. A, B, C, n and m are material constants. A is the yield stress of the material under reference conditions, B is the strain hardening constant,

n is the strain hardening coefficient, C is the strengthening coefficient of strain rate, and m is the thermal softening coefficient.

The equation is used to describe the relationship between the stress and strain of the material under quasi-static loading. The part $[1 + C ln \acute{\varepsilon}^*]$ in the equation is used to represent the effect of strain rate hardening, the coefficient C is an amplification factor. The part $[1 - T^{*m}]$ in the equation is used to describe the effect of thermal softening, where m is a reduction coefficient for the stress. The Johnson-Cook material model is material constitutive equation based on the experimental results.

The coefficient A, B, C, n and m in equation (5.1) can be determined by combining the quasi-static tests with the split Hopkinson pressure bar tests over a wide range of strain rates and temperatures.

5.5 Determination of the Johnson-Cook model parameters

The Johnson-Cook parameters of the Zr-based BMG were determined based on the deformation behavior of $Zr_{55}Cu_{30}Al_{10}Ni_5$ over a range of strain rates and temperature. Yin (2013) conducted a series of uniaxial compression experiments to determine the stress-strain relationship for $Zr_{55}Cu_{30}Al_{10}Ni_5$, with different temperature values at constant strain rate, and different strain rates under constant temperature. In

the current study, the reference strain rate, $\dot{\varepsilon}_{ref}$, and the reference temperature, T_{ref}, were taken as $1x10^{-3}$ s^{-1} and 300 K respectively.

5.5.1 Determination of the parameters A, B and n

First, the parameters *A, B* and *n* can be determined by ignoring the strain rate hardening and thermal softening effect. So the equation (5.1) can be simplified to the following:

$$\sigma_e = \left[\mathrm{A} + \mathrm{B}(\varepsilon_e^p)^n\right] \tag{5.2}$$

Equation (5.2) represents the yield strength at room temperature and the strain rate of *1/s*. The stress-strain curve under quasi-static tests was used to establish the yield stress (σ_s) of the Zr-based BMG, where $\sigma_e = A$. The second step for determining the parameters is changing equation (5.2) to a logarithmic form, as:

$$\ln\left(\sigma_e - \sigma_s\right) = \left[\ln\mathrm{B} + nln\varepsilon_e^p\right] \tag{5.3}$$

By substituting the flow stress and strain values at the reference strain rate, $1x10^{-3}$ s^{-1}, and the reference temperature, 300K, into equation (5.3), the material constants A, B and n were determined as 1702 MPa, 1381 MPa and 0.82 respectively based on the linear relationship between $\ln(\sigma - A)$ and $\ln\varepsilon$.

5.3.2 Determination of the parameter C

For determining material constant C, equation (5.1) can be given as the following at the deformation condition, $T = T_{ref}$ and $\dot{\varepsilon} = \dot{\varepsilon}_{ref}$:

$$\frac{\sigma_e}{\sigma_a} - 1 = C\ ln\dot{\varepsilon}^* \tag{5.4}$$

where σ_a is the stress at $T = T_{ref}$, $\dot{\varepsilon} = \dot{\varepsilon}_{ref}$ and C is the undetermined constant.

By substituting the stress values at three strain rates, $1x10^{-2}$, $1x10^{-3}$ and $1x10^{-4}$, at constant temperature, $T = T_{ref}$, into equation (5.4), the material constant C was determined as 0.032 using curve fitting.

5.5.3 Determination of the parameter m

For determining the material constant m, Equation (1) can be described as the following, at a constant strain rate, $\dot{\varepsilon} = \dot{\varepsilon}_{ref}$:

$$\frac{\sigma_e}{\sigma_b} = 1 - T^{m*} \tag{5.5}$$

By processing equation (9) in a logarithm transformation, equation (5.5) is modified as follows:

$$\ln(1 - \frac{\sigma_e}{\sigma_b}) = m\ lnT^* \tag{5.6}$$

where σ_b is the stress at $T = T_{ref}$ and $\dot{\varepsilon} = \dot{\varepsilon}_{ref}$

By substituting the stress values at three temperature, 678K, 698K and 718K, at constant strain rate, $\dot{\varepsilon} = \dot{\varepsilon}_{ref}$, into equation (5.6), the material constant m was determined as 6.88 using curve fitting. The Johnson-Cook parameters of BMG are listed in table 11.

Table 11 Johnson-Cook material constitutive model parameters of BMG

A (MPa)	B (MPa)	n	C	M	T_{ref} (K)	T_m (K)
1702	1381	0.82	0.032	6.88	300	932

5.6 Determination of the Johnson-Cook damage model parameters

To simulate the chip separation from the workpiece in UPMC, the Johnson-Cook failure model (Johnson and Cook, 1985) was applied. The Johnson-Cook failure model is based on the hypothesis that fracture occurs when the value of the plastic strain at the element integration point reaches a critical value. The failure is assumed to occur when the damage parameter D exceeds 1. The Johnson-Cook failure model can be written as follows:

$$\varepsilon_f = \left[D_1 + D_2 \exp\left(D_3\left(\frac{\sigma_m}{\sigma_{eq}}\right)\right)\right]\left[1 + D_4 In\left(\dot{\varepsilon_p}^*\right)\right][1 + D_5 T^*] \quad (5.7)$$

where ε_f is the equivalent strain at failure, D_1 to D_5 are the damage model constants, σ_m is the mean stress, σ_{eq} is the equivalent stress, and $\dot{\varepsilon}_p{}^* = \frac{\dot{\varepsilon}_p}{\dot{\varepsilon}_{ref}}$ is the relative equivalent plastic strain rate.

The damage parameter D is defined based on the cumulative law as follows:

$$D = \sum \frac{\Delta\varepsilon}{\varepsilon_f} \tag{5.8}$$

where $\Delta\varepsilon$ is the accumulated increment of the equivalent plastic strain. The value of JC damage parameters used for the present study are specified in table 12.

Table 12 Johnson-Cook damage model parameters of BMG

D_1	D_2	D_3	D_4	D_5
-0.09	2.5	-0.5	0.002	2

5.7 Determination of the thermal-mechanical behavior of BMG in UPMC

To reflect the real thermal-mechanical behavior of BMG in UPMC, a scientific thermal-mechanical model needs to be established. The heat in the shear band zone

generated by the deformation of BMG cannot be transferred effectively due to the low heat conductivity and high strain rate in UPMC, so, an adiabatic model was established in the simulation. Adiabatic thermal-stress analysis is typically used to simulate high strain rate processes involving large amounts of inelastic strain, where the heating of the material caused by its deformation is an important effect because of temperature-dependent material properties. An increase in temperature is calculated directly at the material integration points according to an increase in the adiabatic thermal energy caused by inelastic deformation; temperature is not a degree of freedom in the simulation. No allowance is made for heat conduction in an adiabatic analysis. In the adiabatic analysis, plastic straining gives rise to a heat flux per unit volume of:

$$r^{pl} = \eta\sigma : \dot{\varepsilon}^{pl} \tag{5.9}$$

where r^{pl} is the heat flux that is added into the thermal energy balance, η is the user-specified inelastic heat fraction, σ is the stress, and $\dot{\varepsilon}^{pl}$ is the rate of plastic straining.

The heat equation solved at each integration point is

$$\rho c(\theta)\dot{\theta} = r^{pl} \tag{5.10}$$

where ρ is the material density and $c(\theta)$ is the specific heat.

A realistic reflection of the coupling contact features between the tool and chip interface can guarantee the simulation accuracy. The modified Coulomb friction model was been used in the simulation and the average value of the friction coefficient was set to be 0.2.

5.6 Twinned-serrated chip formation

Figure 5.4 shows the evolution process of the twinned shear in one serrated chip, with the stress and temperature of the primary shear band in the UPMC of BMG. In figure 5.4a, the stress and temperature of the primary shear band began to increase due to the material deformation in the shear zone. As shown in figure 5.4b, the heat of deformation cannot be transferred effectively and the temperature in the adiabatic shear band reached a peak under the feed movement of the tool, so the chip began to flow because of the material thermal softening effect, and the stress in the adiabatic shear band fell rapidly. The stress in the shear band is much less than outside, while the temperature shear band is much higher than outside. At the same time, a serrated chip began to form. An interesting phenomenon was observed and the twinned minor shear appeared in figure 5.4c. Subsequantly, the twinned minor shear zone blended together with the first serrated chip due to the compression stress in the cutting direction through

the tool. Then the second cycle of serrated chip began to form.

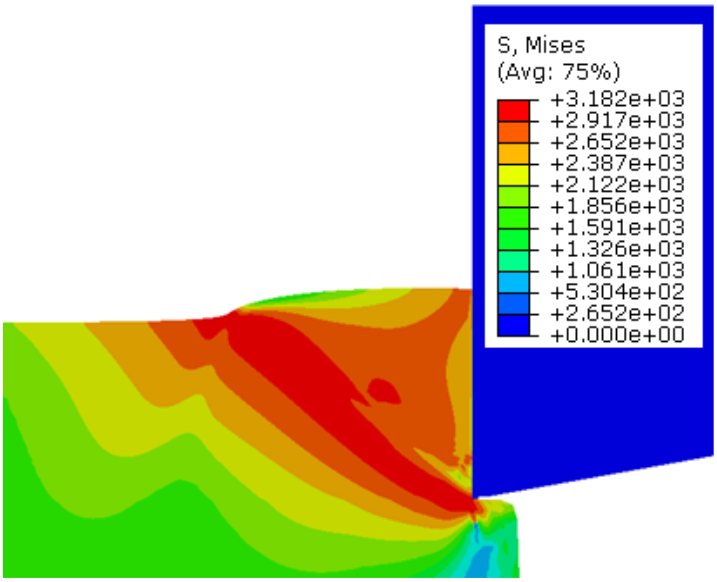

(a1) Stress distribution

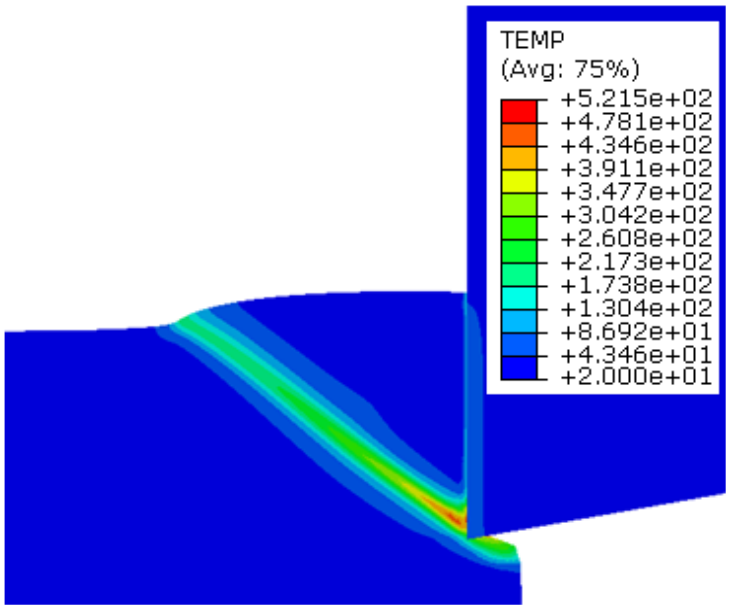

(a2) Temperature Distribution

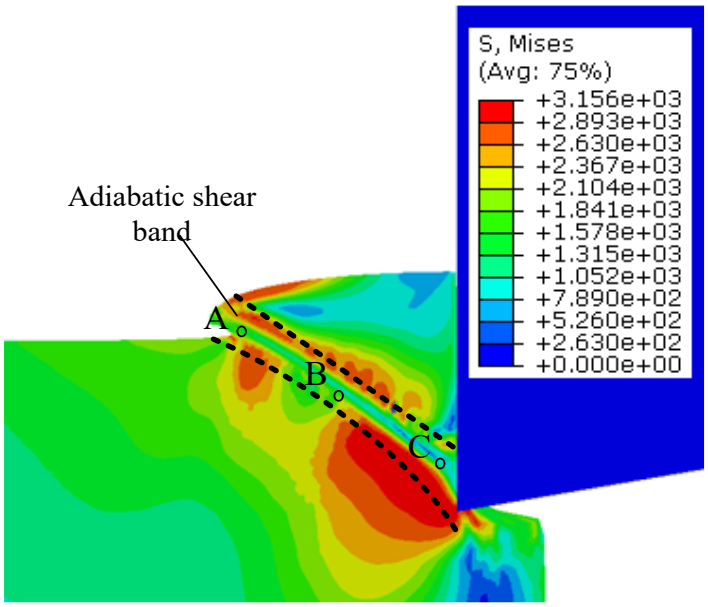

(b1) Stress distribution

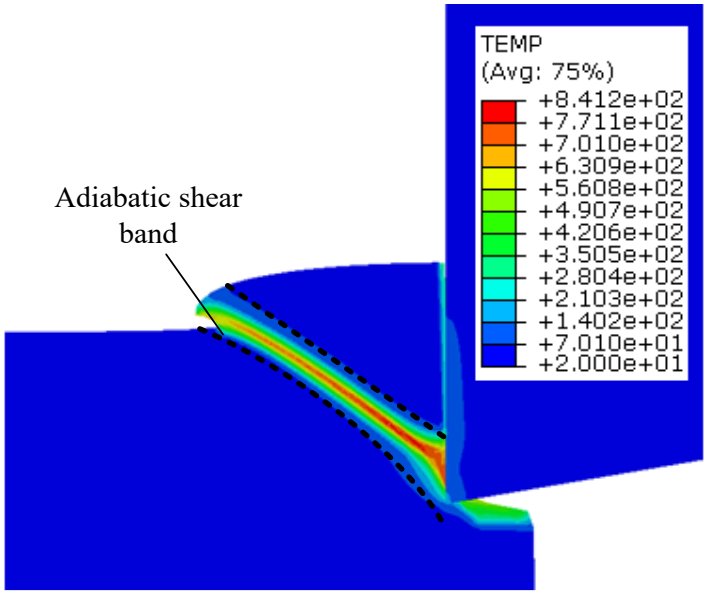

(b2) Temperature distribution

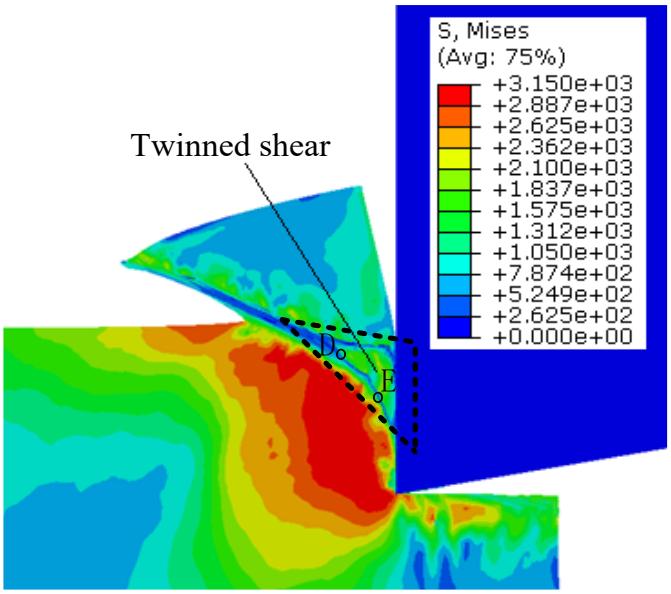

(c1) Stress distribution

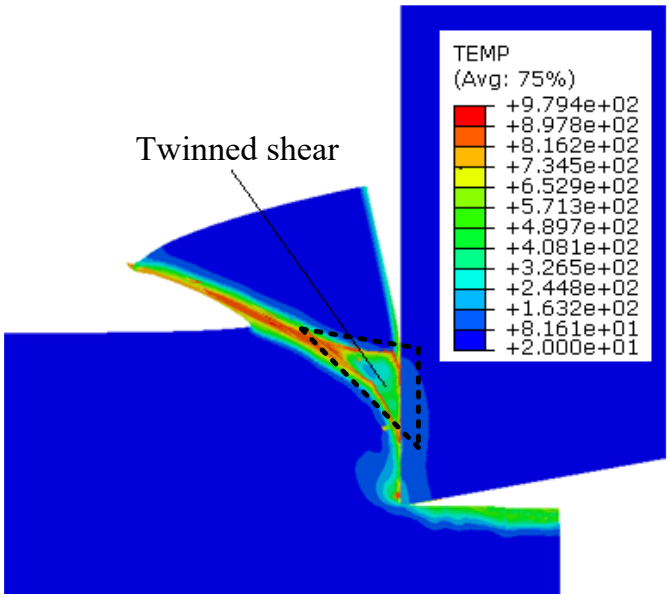

(c2) Temperature Distribution

Figure 5.4 Simulation results on the formation of twinned serrated chip with the change of stress and temperature in shear bands of BMG (UPMC: Rake angle 0 ˚, cutting speed 100 mm/min)

To reveal the change of stress and temperature at the shear band in UPMC of BMG, the points A, B and C in the primary adiabatic shear band, and the points D and E in the twinned shear band were examined. The locations of the five points are shown in figure 5.5. Figure 5.6 shows the changes in stress and temperature at the five points A, B, C, D and E during the formation of one serrated chip. It can be clearly seen that there are three stages in the formation cycle of one serrated chip: Elastic deformation, plastic deformation and shear-fracture. During the three stages, the stress and temperature of the five points in the shear band began to increase, then the stress reached a peak and the material began to soften and flow. Locations A, B and C in the primary shear band began to shear first, then the stress decreased rapidly and the temperature reached a peak. Whereafter, D and E began to shear and twinned shear occurred, then the temperature at D, E reached peaks, and the whole cycle of the serrated chip finished. From the change tendency of the stress and temperature at the five points, it fully proved that twinned shear in one cycle of each serrated chip existed.

The primary cutting force curve of BMG in the simulation and experiment are shown in figure 5.6, where it can be seen clearly that the cutting force fluctuates with the formation of the serrated chips. Differing from the common cutting forces featuring orderly separated zigzag shapes observed in diamond cutting of other materials, the

cutting forces shown in figure 5.7 are characterized by the twinned minor shear phenomenon in each cycle of serrated chip formation, which indicates a different material removal mechanism. Specifically, in the diamond cutting of BMG, each zigzag cycle includes two separate crests, namely a big crest followed by a small one, which indicates that each chip formation for BMG has a two-step cutting behavior.

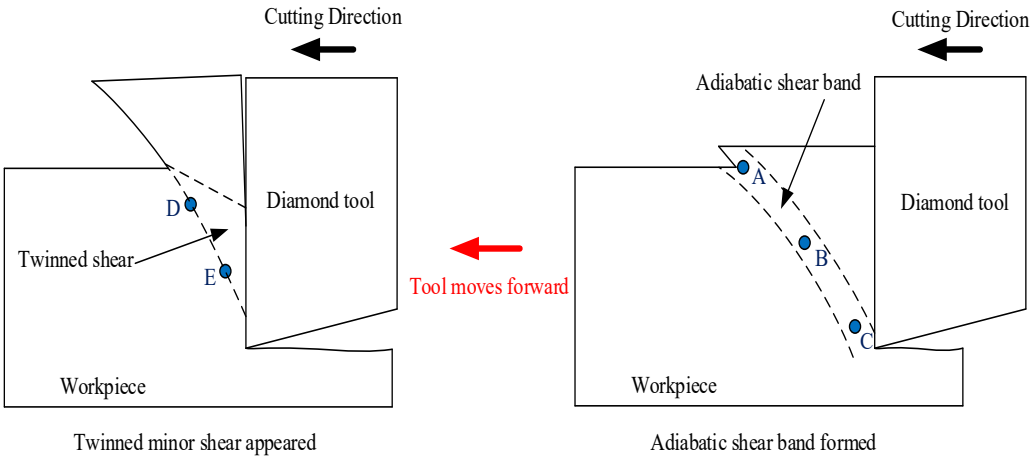

Figure 5.5 Equivalent points in the formation of one serrated chip

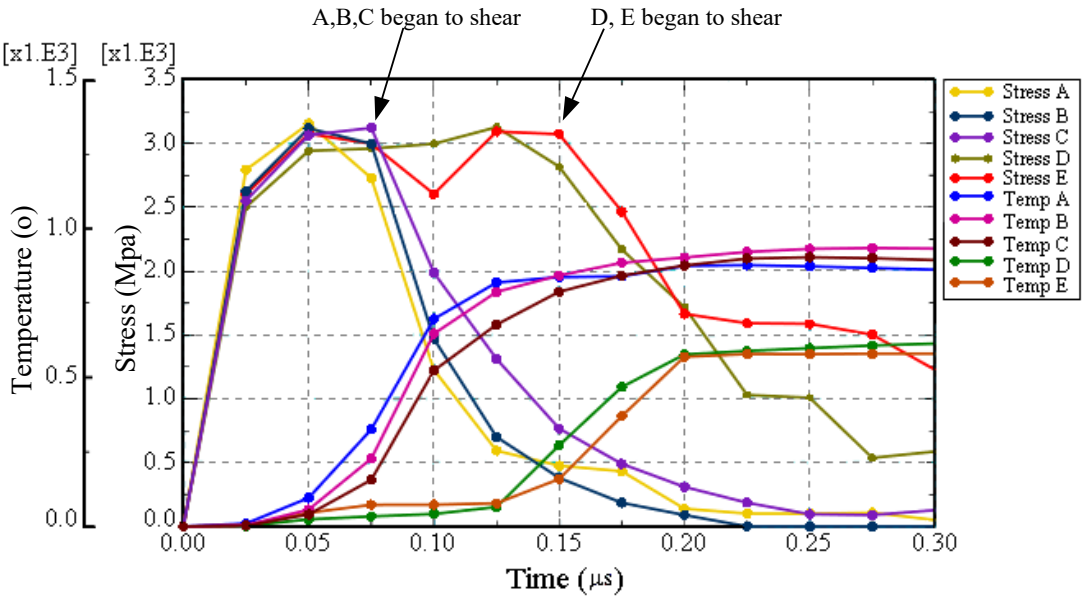

Figure 5.6 Change of stress and temperature at element A, B and C in the adiabatic shear band during the formation of one serrated chip

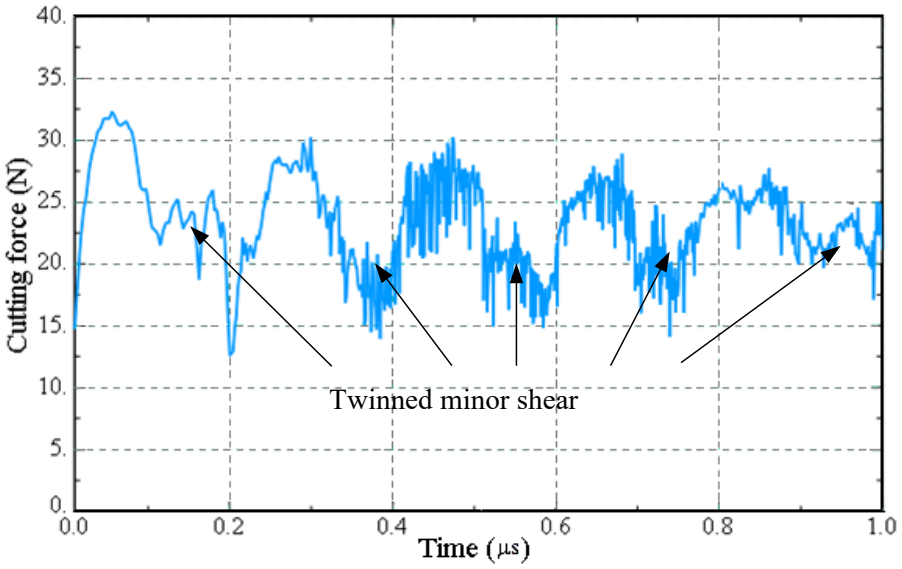

(a)

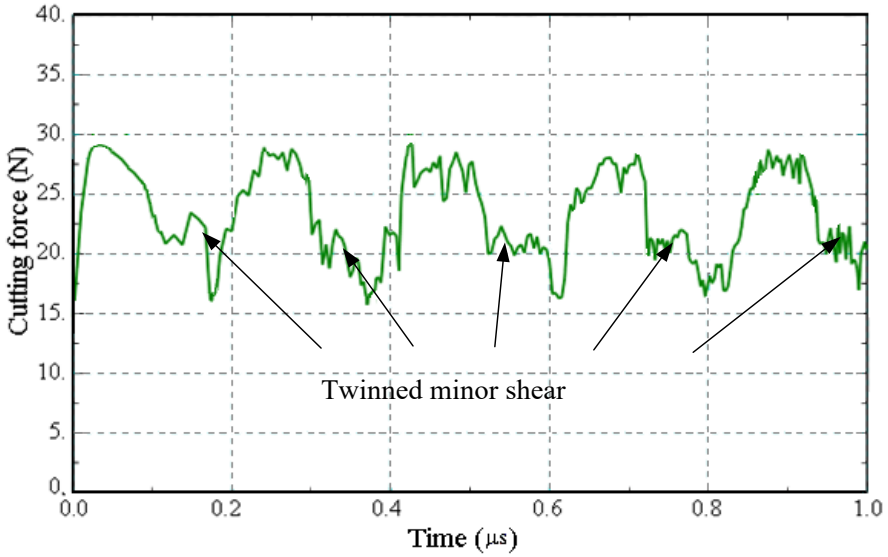

(b)

Figure 5.7 (a) Simulation result and (b) experiment result on the cutting forces under cutting condition at tool rake angle at 0°, cutting speed at 100 mm/min, and depth of cut of 7μm

5.7 Material removal mechanism

To further determined the unique material removal process in the diamond cutting of BMG, the chip formation process was also observed and simulated, as shown in figure 5.9. Figure 5.9 shows the generated and simulated serrated chip morphologies in diamond cutting of BMG under different rake angles. It should be noted that the original chip formed in the diamond cutting test was a continuous curled chip. Since the cutting distance in the test was relatively long compared to the simulation, the long continuous

curled chip rolled up as a spiral. When the chip length increased, the outer curvature of the spiral decreased in the zoom-in view. As a result, the magnified view of the chip near the primary deformation zone in SEM appeared straightened, as shown in figure 5.8. referring to figure 5.9, the chips of BMG feature the twinned shear band, namely a big zigzag followed by a small one, which explains the twinned minor shear phenomenon shown in figure 5.7. A good consistency between the experimental and simulated results also validates the simulation as well reflecting the chip formation process. From the simulated heat distribution results, serrated chips are caused by the adiabatic effect due to the low heat conductivity. Both the experimental and simulation results indicate that a second shearing process is generated in the chip formation process, which cause a small zigzag shape following the big one and leads to the cutting force fluctuations during each serrated chip formation cycle.

In addition, figure 5.9 shows that the serrated chip very clearly under rake angles of 0°, -10° and 25°, while the serrated chip is inconspicuous at a rake angle of 5°. It can be inferred that a negative rake angle will increase the serration level of the chips. In addition, from figure 5.9, it can also be seen that a twinned minor shear phenomenon exists in the cycle of each serrated chip. The larger the negative rake angle, the more obvious the twinned shear and the serration level of the chips can be observed.

Therefore, the results of chip comparison proved that the extent of serrated chip is very sensitive to the rake angle.

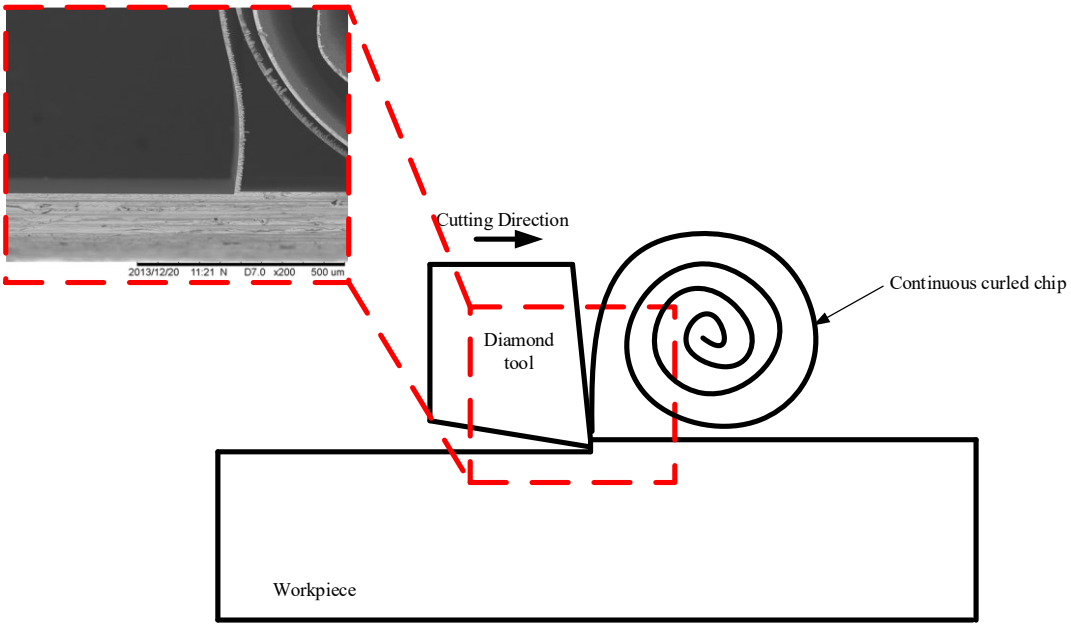

Figure 5.8 The formation mechanism of the spiral chips.

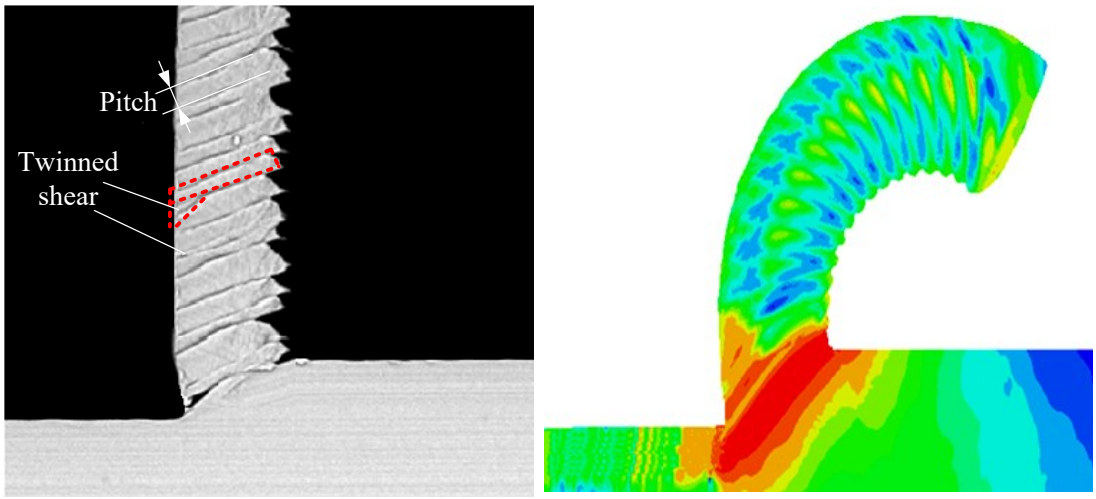

(a1) Chip of test (a2) Chip of simulation

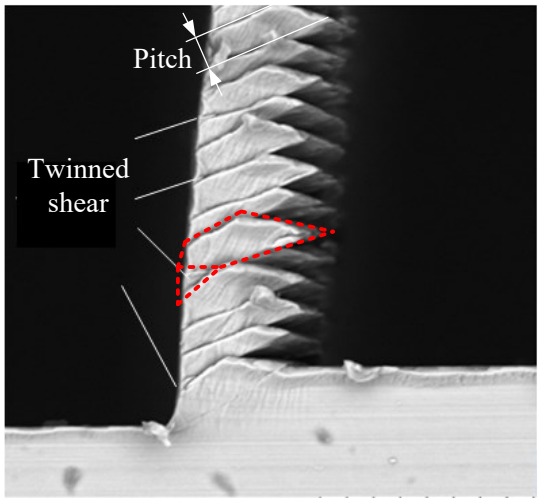

(b1) Chip of test

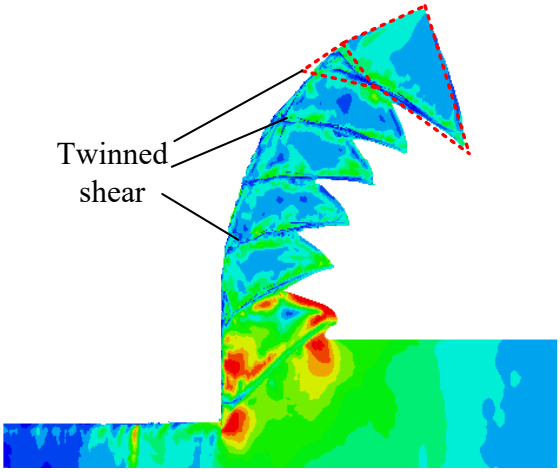

(b2) Chip of simulation

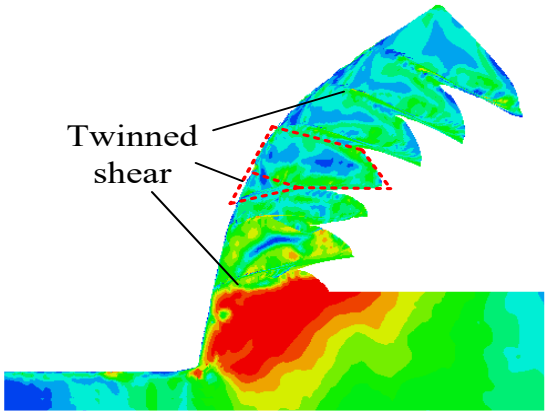

(c1) Chip of test

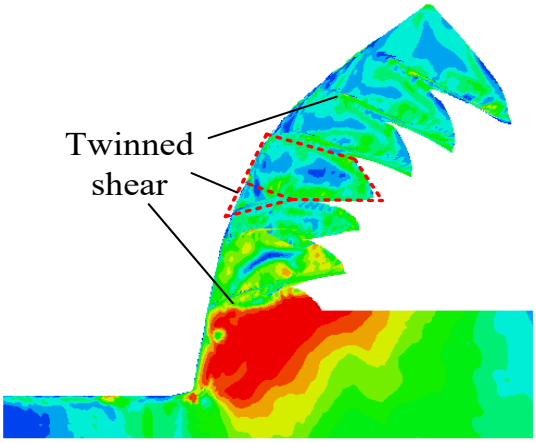

(c2) Chip of simulation

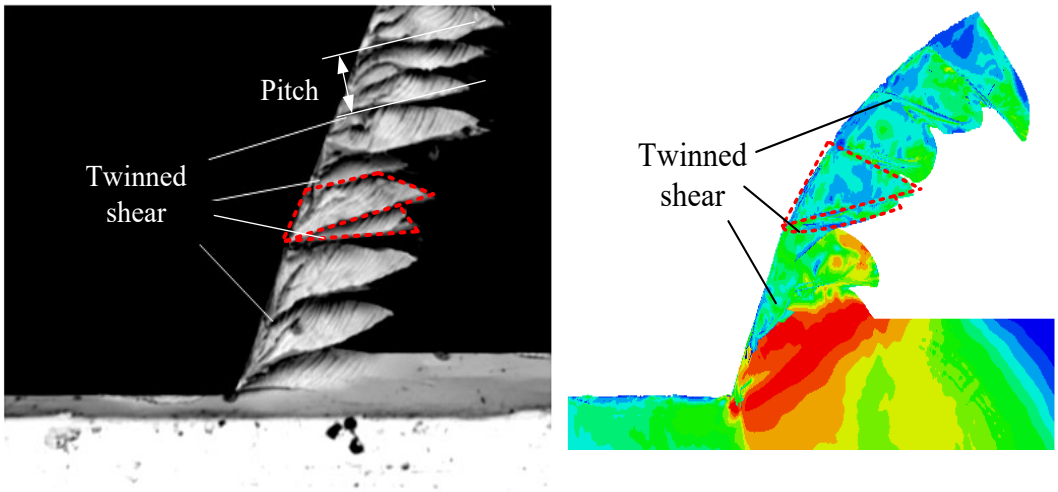

(d1) Chip of test (d2) Chip of simulation

Figure 5.9 Comparison of chips between experiment and simulation in ultra-precision turning of BMG at different rake angles: (a) 5 ˚, (b) 0 ˚, (c) -10 ˚, (d) -25 ˚, with cutting condition at a cutting speed of 100 mm/min, and depth of cut of 7μm

Figure 5.10 is the evaluation model of the extent of the serrated chip of BMG. Table 13 shows the effects of rake angle on the main cutting force and the pitch of the serrated chip in simulations and tests of BMG. The simulation results agree with the experiment results very well. From table 13, the average value and amplitude of the cutting force increased when the tool rake angle changed from positive to negative, and the pitch of the serrated chip also has the same characteristic. So, the results proved that a negative rake angle will increase the extent of the serration.

In addition to the cutting speed at 100 mm/min, the experiment results adopted

different cutting speeds at 200 and 400 mm/min. Similar twinned-serrated chips were also observed at 200 and 400 mm/min using the -10° tool rake angle, as shown in figure 5.11 (a) and (b), which indicates that the chip formation mechanism can mostly be attributed to inherent material the properties. A lower cutting depth at 1 μm was also adopted in the experiments to observe the chip formation, as shown in figure 5.11 (c). In this case, even though the chips are characterized as snatchy shape compared with the larger cutting depths, the twinned chips can also be clearly observed. Based on the simulation results, the serrated chips are mostly caused by the adiabatic effect due to the low heat conductivity.

Table 13 Effect of rake angle on cutting force and the pitch of the serrated chip

	Pitch		Average cutting force		Amplitude of the cutting force	
Rake angle	Simulation	Test	Simulation	Test	Simulation	Test
5	2.35μm	2.64μm	20.1N	24.91N	8.81N	7.26N
0	3.32μm	3.56μm	23.7N	27.22N	15.93N	11.87N
-10	6.17μm	6.81μm	27.3N	34.09N	16.24N	12.18N
-25	7.05μm	7.33μm	32.6N	38.59N	17.06N	13.23N

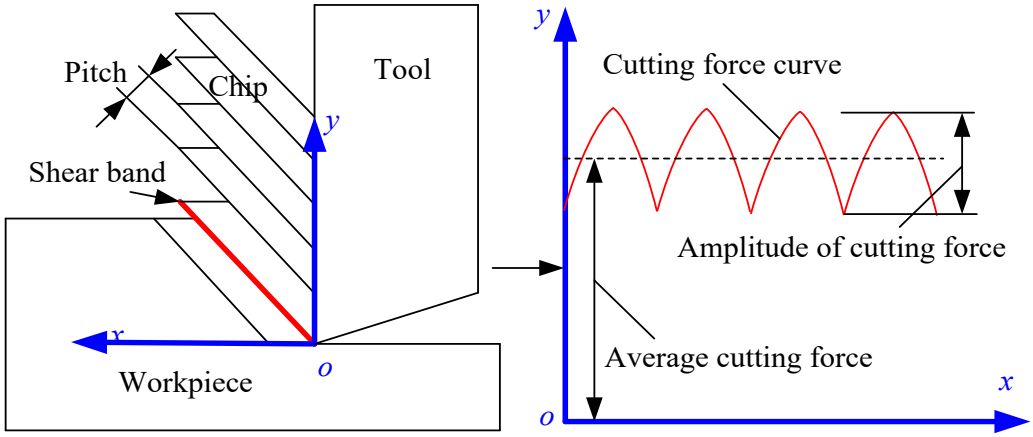

Figure 5.10 Evaluation model of the extent for the serrated chip of BMG

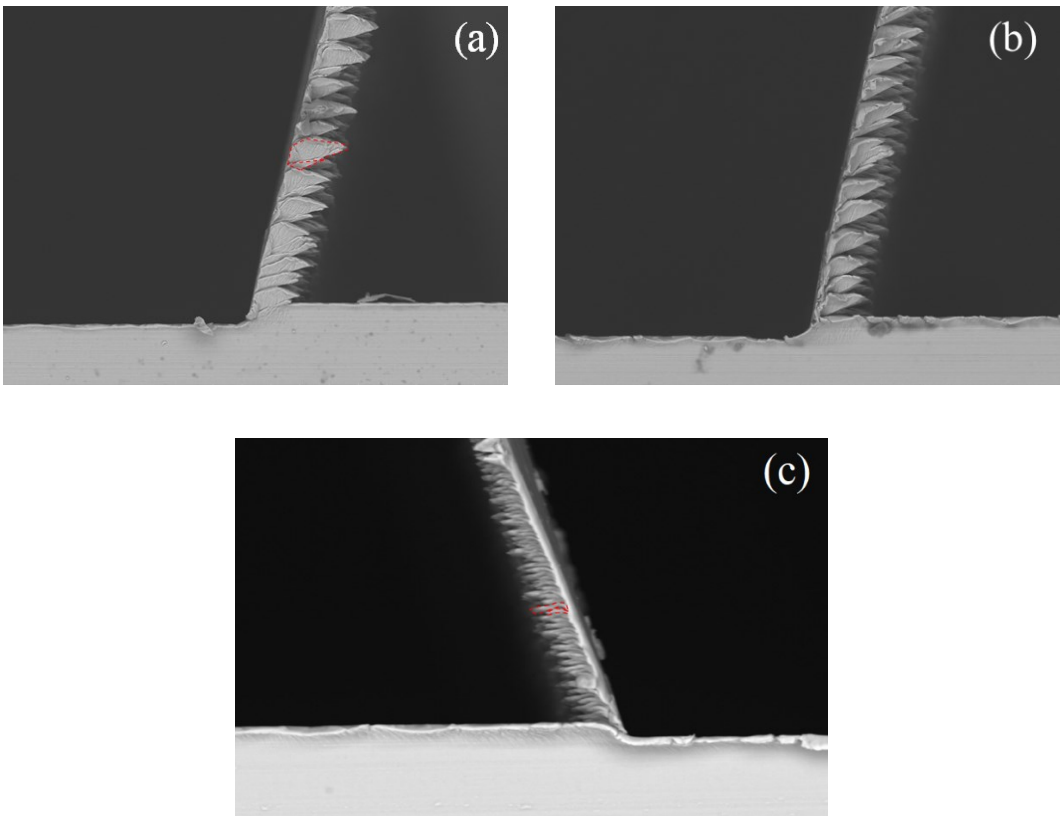

Figure 5.11. The SEM image of the chip formation with tool rake angle in -10° under cutting conditions in (a) the cutting speed at 200 mm/min and depth of cut in 7μm; (b)

the cutting speed 400 mm/min and depth of cut in 7μm; (c) the cutting speed at 100 mm/min and cutting depths at 1 μm

5.8 Conclusions

To investigate the cutting mechanisms of serrated chip formation in ultra-precision micro-cutting of bulk metallic glass, a series of UPMC tests was carried out and the cutting process was simulated by the finite element method. The unique twinned-serrated chip formation process in the diamond cutting of BMG was first observed and simulated, and its effects on the chip formation and cutting force oscillations were also analyzed in order to learn the to determine the material removal mechanism of BMG. The changes of temperature and stress in the cutting zone were examined based on an adiabatic model for calculating the temperatures in the shear band according to the increase of the adiabatic thermal energy caused by the inelastic deformation.

The material removal process of BMG is characterized as a twinned minor shear phenomenon in each cycle of each serrated chip formation. The primary shear band is formed mostly due to the material thermal softening effect, and the stress in the adiabatic shear band falls rapidly. The twinned minor shear zone blends together with the primary serrated chip due to the compression in cutting direction through the tool.

The proposed adiabatic model can well simulate the chip formation process of BMG, and verifies that the chip formation includes three separate stages: namely elastic deformation, plastic deformation and shear-fracture. Each stage occurs along with the change of temperature and stress.

Serrated chips are caused by the adiabatic effect due to the low heat conductivity. Both the experimental and simulation results indicate that a second shearing process is generated in the chip formation process, which results in a small zigzag shape, following the big one, and leads to cutting force fluctuations during each serrated chip formation cycle.

The average value and amplitude of the cutting force increases when the tool rake angle is changed from positive to negative, and the pitch of the serrated chip also has the same effect. So, the results proved that a negative rake angle will increase the extent of the serration.

Chapter 6 Conclusions and future work

6.1 Overall conlusions

An theoretical and experimental investigation into the factors affecting the surface roughness in ultra-precision diamond turning was conducted.It was found that the surface roughness of SPDT BMGs was affected by both material and process factors. In general, the process of cutting Zr-based BMGs can improve the surface quality by reducing the spindle speed and applying a critical depth of cut. This is because the process factors affect the material factors due to the glass properties of BMG, and a high cutting speed and depth of cut will lead to an increased swelling effect of the machined workpiece surface and built-up edge on the diamond tool. The cutting temperature can react to the glass transition temperature of BMGs due to the low thermal conductivity of BMGs. An adiabatic system occurs between the cutting edge and workpiece surface, which lead to BUE formation on the diamond tool and increased swelling effect of the machined surface due to the glass properties of BMGs. The BUE will damage the machined surface. The mechanics involved in the forming of the BUE in machining BMG are proposed.

To investigate the effect of the cutting speed on the multiple shear bands formation and the machining induced crystallization effect in the micro-cutting BMG. Straight cutting experiments of a Zr-based BMG were conducted, and continuous serrated chip

were observed at different cutting speeds. A series of slip-steps were found in the primary deformation zone and within the serrations in the diamond cutting of BMGs, and the shear bands propagation mechanism was influenced by the cutting speed. The observations of the influence of the cutting speed on the formation and propagation of shear bands suggested that a higher cutting speed can inhibit the growth and propagation of shear bands. Micro-cutting-induced nanocrystallization occurred through the TEM investigation. Micro-cutting at high cutting speed contributed to the formation of much more substantial nanocrystals dispersing in the entire PDZ in comparison to that at low speed cutting, as the low-speed cutting process only induced nanocrystals within the shear bands. A finer machined surface can be obtained when the shear bands in the PDZ are fully developed, since it helps to release the built-up stress and avoided cracks forming. It provided evidence that the surface integrity of BMGs in diamond cutting is sensitive to the cutting speed due to the formation of nanocrystals and shear bands.

To investigate the material removal mechanisms of the serrated chip formation in micro-cutting cutting of BMGs, a series of UPMC tests were carried out and the cutting process simulated by the finite element method. The unique twinned-serrated chip formation process in diamond cutting of BMG was first observed and simulated, and its effects on the chip formation and cutting force oscillations were also analyzed in

order to learn the to determine the material removal mechanism of BMGs. The primary shear band in the PDZ is mostly formed due to the material thermal softening effect and the stress in the adiabatic shear band falls rapidly. The twinned minor shear zone blends together with the primary serrated chip due to the compression in cutting direction through the tool. In addition, both the experimental and simulation results revealed a small zigzag shape, following the big one, in the chip formation process is caused by the formation of secondary shear band, which leads to cutting force fluctuations during each serrated chip formation cycle. The average cutting force and the pitch of the serrated chip increased when the tool rake angle decreased from positive to negative. This result indicates that the extent of the serrations can be increased by applying a negative tool rake angle during the micro-cutting of BMGs.

In response to the limitations of the existing research on cutting mechanics of bulk metallic glasses in the field of ultra-precision machining, this research study has contributed to the understanding on the cutting mechanics of SPDT BMGs in that (i) revealing the surface generation under particular cutting conditions, which providing a comprehensive understanding of the cutting characteristic in SPDT of BMGs; (ii) a new insight into the mechanism of shear band formation and propagation in SPDT, by firstly revealing the multiple shear bands formation and the interaction between the primary and secondary shear bands in the primary deformation zone in the micro-cutting of

BMGs; (iii) revealing the micro-machining-induced nanocrystallization and their effect on the surface generation in the SPDT of BMGs; (iv) FEA modelling of the chip formation in SPDT of BMGs is realized for the first time, revealing the mechanism of generating twinned-serrated chips in SPDT of BMG, the simulation and experimental results indicate that negative rake angle is a more favorable condition for generating twinned-serrated chips in SPDT of BMGs.

6.2 Suggestions for future research

In this thesis, a theoretical and experimental framework is established for the analysis the cutting mechanic in SPDT of bulk metallic glasses, which takes into consideration the surface generation, microstructure change of BMGs and chip formation. Novel experimental and modelling techniques are proposed to study the cutting mechanics and chip formation in the micro-cutting of BMGs. Based on the findings from the present study, there are some suggestions for future research as below:

(i) The effect of cutting speed on the multiple shear bands formation and propagation in the micro-cutting of BMGs are revealed. Future work can be employing a high-speed camera in the micro-cutting experiments under different cutting conditions, which can characterize deformation behavior in terms of the evolution of shear bands localized in the primary deformation zone. This will further

information for the material removal mechanism of BMGs in the micro-cutting process.

(ii) Future work can be conducted on the micro-machining of BMGs with the applying the tool-tip vibration-assisted technique to reduce the formation of built-up material on cutting tool. According to the experimental results and proposed theory in this thesis, the built-up edge formed on the tool and the swelling on the machined surface is caused by the adiabatic system between the workpiece surface and the tool-tip. The temperature in the cutting zone can be reduced by effective cooling. The imposed tool-tip vibration will help to reduce the cutting temperature by reducing the contact time between the workpiece and cutting tool, which can increase the cooling time and the amount of cooling agent get into the cutting zone.

References

Acharya A. and Bassani J. L., “Lattice incompatibility and a gradient theory of crystal plasticity,” Journal of the Mechanics and Physics of Solids, Vol. 48, pp. 1565-1595 (2000).

Argon A. S., “Plastic deformation in metallic glasses,” Acta Metallurgica, Vol. 27, pp. 47-58 (1979).

Bakkal M., Shih A. J. and Scattergood R. O., “Chip formation, cutting forces, and tool wear in turning of Zr-based bulk metallic glass,” International Journal of Machine Tools Manufacture, Vol. 44, pp. 915–925 (2004a).

Bakkal M., Shih A. J., Scattergood R. O. and Liu C. T., “Machining of a Zr–Ti–Al–Cu–Ni metallic glass,” Scripta Materialia, Vol. 50, pp. 583–588 (2004b).

Bakkal M., Shih A. J., McSpadden S. B. and Liu C. T., “R.O. Scattergood, Light emission, chip morphology, and burr formation in drilling the bulk metallic glass,” International Journal of Machine Tools and Manufacture, Vol. 245, pp. 741–752 (2005a).

Bakkal M., Liu C. T., Watkins T. R., Scattergood R. O. and Shih A. J., “Oxidation and crystallization of Zr-based bulk metallic glass due to machining,” Intermetallics, Vol. 12, pp.195 (2004c).

References

Bakkal M., Shih A. J., McSpadden S. B. and Scattergood R. O., “Thrust force, torque, and tool wear in drilling the bulk metallic glass,” International Journal of Machine Tools and Manufacture, vol. 45 pp. 863–872 (2005b).

Bengus V. Z., Tabachikova E. D., Shumilin S. E., Golovin Y. L., Makarov M. V., Shibov A. A., Miskuf J., Csach K. and Ocelik V., “Some peculiarities of ductile shear failure of amorphous alloy ribbons,” International Journal of Rapid Solidification, Vol. 8, pp21-31 (1993).

Black J. T., “On the fundamental mechanism of large strain plastic deformation”, Journal of Engineering for Industry, pp.507-526 (1971).

Burnham, M. W., “The mechanics of micromachining”, Proceedings of Society of Photo-Optical Instrumentation Engineers 0093; Advances in Precision Machining of Optics, San Diego, United States, pp.38-45 (1976).

Ceretti E., Fallbohmer P., Wu W. T. and Altan T., “Application of 2-D FEM to chip formation in orthogonal cutting”, Journal of Materials Processing Technology, Vol. 59, pp. 169-180 (1996).

Chau S. Y., To S., Chan K. C. and Cheung C. F., “Cutting characteristics of zirconium based bulk metallic glasses in ultra-precision diamond turning,” Proceedings of the 4th International Conference on Nanomanuufacturing: Bremen, Gemary (2014).

Chen H. S., “Plastic flow in metallic glasses under compression”, Scripta. Materialia, Vol. 7, pp. 931-936 (1973).

Chen H.S. and Turnbull D., "Evidence of a glass-liquid transition in a gold-germanium-silicon alloy," The Journal of Chemical Physics, Vol. 48, pp. 2560-2571 (1968).

Chen H. S. and Turnbull D., "Formation, stability and structure of palladium-silicon based alloy glasses," Acta Metallurgica, Vol. 17, pp. 1021-1031(1969).

Chen H. S., "Glassy metals," Reports on Progress in Physics, Vol. 43, pp. 353–432 (1980).

Chen G., Ren C., Zhang P., Cui K. and Li Y., “Measurement and finite element simulation of micro-cutting temperatures of tool tip and workpiece,” International Journal of Machine Tools and Manufacture, Vol. 75, pp. 16–26 (2013).

Chen X, Xiao J., Zhu Y., Tian R., Shu X. and Xu J., “Micro-machinability of bulk metallic glass in UPMC,” Materials and Design, Vol. 136, pp. 1–12 (2017).

Cheung C. F. and Lee W. B., Surface generation in ultra-precision diamond turning: modelling and practices, Professional Engineering (2003).

Cheung C. F. and Lee W. B., “Study of factors affecting the surface quality in ultra-precision diamond turning,” Materials and manufacturing processes, Vol.15, no.4, pp.481-502 (2000).

References

Cheung C. F., To S. and Lee W. B., “Anisotropy of surface roughness in diamond turning of brittle single crystals,” Material and Manufacturing Processes, Vol. 17, pp. 251–267 (2002).

Choi Y. H., Xu D. H., and Johnson W. L., "Ni-based bulk metallic glass formation in the Ni-Nb-Sn and Ni-Nb-Sn-X (X = B,Fe,Cu) alloy systems," Applied Physics Letters, Vol. 82, pp. 1030-1032 (2003).

Cohen M. H. and Turnbull D., “Metastability of amorphous structures”, Nature, Vol.203, pp. 964 (1964).

Daniel M., “Liquidmetal Design Guide 5.0”, Liquidmetal, [Online]. Available: https://www.liquidmetal.com/liquidmetal-design-guide-5-is-now-available/ (7 Nov 2019).

Dehey P., Sietsma J. and Vandenbeukel A., “Creation of free volume in amorphous Pd40Ni40P20 during high temperature deformation,” Materials and Science Engineering: A, Vol. 226, pp. 336-340 (1997).

Degarmo E. P., Black J. T. and Kohser R. A., Materials and processes in manufacturing, Ninth edition, Wiley (2003).

Elliott S. R., Physics of amorphous materials, Longman London (1984).

Evans C., “Cryogenic diamond turning of stainless steel,” Annals of the CIRP, Vol. 40, pp.571-582 (1991).

References

Fang F. Z., Wu H., Zhou W. and Hu X. T., "A study on mechanism of nano-cutting single crystal silicon," Journal of Materials Processing Technology, Vol. 184, pp. 407- 410 (2007).

Fang N., "Slip-line modelling of machining with a rounded-edge tool – Part I: new model and theory," Journal of the Mechanics and Physics of Solids, Vol.51, pp. 715-742 (2003a).

Fang N., "Slip-line modelling of machining with a rounded-edge tool – Part II: analysis of the size effect and the shear strain-rate," Journal of the Mechanics and Physics of Solids, Vol.51, pp. 743-762 (2003b).

Fang N. and Dewhurst P., "Slip-line modeling of built-up edge formation in machining", International Journal of Mechanical Sciences, Vol. 47, pp. 1079-1098 (2005).

Fleck N. A., Muller G. M., Ashby M. F. and Hutchinson J. W., "Strain gradient plasticity: theory and experiments", Acta Metallurgica et Materialia, Vol. 42, pp. 475-487 (1994).

Fleck N. A. and Hutchinson J. W., "A phenomenological theory for strain gradient effects in plasticity," Journal of the Mechanics and Physics of Solids, Vol. 41, pp. 1825-1857 (1993).

Fujita K., Morishita Y., Nishiyama N., Kimura H. and Inoue A., "Cutting characteristics of bulk metallic glass," Material Transactions, Vol.46, pp.2856-2863 (2005).

References

Furukawa Y. and Moronuki N., “Effect of material properties on ultra-precise cutting processes,” Annals of the CIRP, Vol. 37, pp.113-116 (1988).

Gao H., Huang, Y., Nix W. D. and Hutchinson J. W., “Mechanism-based strain gradient plasticity – I. Theory,” Journal of the Mechanics and Physics of Solids, Vol. 47, pp. 1239-1263 (1999).

Guo Y. B., “A FEM study on mechanisms of discontinuous chip formation in hard turning,” Journal of Materials Processing Technology, Vol. 155-156, p. 1350-1356 (2004).

Guo Y. B. and Chou Y. K., “The determination of ploughing force and its influence on material properties in metal cutting,” Journal of Materials Processing Technology, Vol.148, pp. 368-375 (2004).

GschneidnerJr K. A., Pecharsky V. K., and Tsokol A. O., "Recent developments in magnetocaloric materials," Reports on Progress in Physics, Vol. 68, pp. 1479-1539 (2005).

Han D. X., Wang G., Li J., Chan K. C., To S., Wu F. F., Gao Y. L. and Zhai Q. J., “Cutting characteristics of Zr-based bulk metallic glass,” Journal of Materials Science and Technology, Vol. 31, pp. 153–158 (2015).

References

He G., Loser W., Eckert J., and Schultz L., "Enhanced plasticity in a Ti-based bulk metallic glass-forming alloy by in situ formation of a composite microstructure," Journal of Materials Research, Vol. 17, pp. 3015-3018 (2002).

Huang H. and Yan J., “Microstructural changes of Zr-based metallic glass during microelectrical discharge machining and grinding by a sintered diamond tool,” Journal of Alloys and Compounds, Vol. 688, pp. 14–21 (2016).

Inoue A., “Stabilization of metallic supercooled liquid and bulk amorphous alloy,” Acta Materialia, Vol. 48, pp. 279-306 (2000).

Inoue A. and Takeuchi A., “Recent development and application products of bulk glassy alloys,” Acta Materialia, Vol. 59, pp. 2243-2267 (2011).

Inoue A., Kita K., Zhang T., and Masumoto T., "An amorphous $La_{55}AI_{25}Ni_{20}$ alloy prepared by water quenching," Materials Transactions, Vol. 30, pp. 722-725 (1989).

Inoue A., Nakamura T., Sugita T., Zhang T., and Masumoto T., "Bulky La-Al-Tm (Tm = transition-metal) amorphous-alloys with high-tensile strength produced by a high-pressure die-casting method," Materials Transactions, Vol. 34, pp. 351-358 (1993).

Inoue A., Nakamura T., Nishiyama N., and Masumoto T., "Mg-Cu-Y bulk amorphous-alloys with high-tensile strength produced by a high-pressure die-casting method," Materials Transactions Japan Institute of Metals, Vol. 33, pp. 937-945 (1992).

Inoue A., Shen B.L., Koshiba H., Kato H. and Yavari A.R., "Cobalt-based bulk glassy alloy with ultrahigh strength and soft magnetic properties," Nature Materials, Vol. 2, pp. 661–663 (2003).

Inoue A., Zhang T., andMasumoto T., "Production of amorphous cylinder and sheet of La55Al25Ni20 Alloy by a metallic mold casting method," Materials Transactions, Vol. 31, pp. 425-428 (1990).

Ikawa N., Donaldson R. R., Komanduri R. W., Konog, Aachen T. H., Mckeown P.A., Moriwaki T. and Stowers I. F., “Ultraprecision metal cutting—the past, the present and the future,” Annals of the CIRP – Manufacturing Technology, Vol. 40, pp.587-594 (1990).

Iwata K., Osakada K. and Terasaka Y., “Process modeling of orthogonal cutting by therigid-plastic finite element method,” ASME Journal of Engineering Materials and Technology, Vol. 106, pp. 132-138 (1984).

Jiang M. Q. and Dai L. H.,” Formation mechanism of lamellar chips during machining of bulk metallic glass,” Acta Materialia, Vol. 57, 2730–2738 (2009).

Johnson R. and Cook W. K., “A constitutive model and data for metals subjected to large strains high strain rates and high temperatures,” In Proceeding of the 7th International Symposium on Ballistics: Hague, Netherlands, pp. 541–547 (1983).

References

Johnson R. and Cook W. K., “Fracture characteristics of three metals subjected to various strains, strain rates, temperatures and pressures,” Engineering Fracture Mechanics, Vol. 21, pp. 31-48 (1985).

Johnson G. R. and Cook W. H., “Fracture characteristics of three metals subject to various strains, strain rates, temperatures and pressures,” Engineering Fracture Mechanics, Vol. 21, pp. 31-48 (1985).

Kakino, Y., “Analysis of the mechanism of orthogonal machining by the finite element method,” Journal of the Japan Society for Precision Engineering, Vol. 37, pp. 503-508 (1971).

Kim D. H., Bae D. H., Lim H. K., Kim S. H., and Kim W. T., "Mechanical behavior of a bulk Cu-Ti-Zr-Ni-Si-Sn metallic glass forming nano-crystal aggregate bands during deformation in the supercooled liquid region," Acta Materialia, Vol. 50, pp. 1749-1759 (2002).

Kim J. J., Choi Y., Suresh S. and Agron A. S., “Nanocrystallization during nanoindentation of a bulk amorphous metal alloy at room temperature,” Science, Vol. 295, pp. 654-657 (2002).

Kim K. W., Lee W. Y. and Sin H. C., “A finite element analysis of machining with the tool edge considered,” Journal of Materials Processing Technology, Vol. 86, pp. 45-55 (1999b).

References

Kim K. W., Lee W. Y. and Sin H., “A finite element analysis for the characteristics of temperature and stress in micro-machining considering the size effect”, International Journal of Machine Tools and Manufacture, Vol. 39, pp. 1507-1524 (1999a).

Kim Y. C., Kim D. H., and Lee J. C., "Formation of ductile Cu-based bulk metallic glass matrix composite by Ta addition," Materials Transactions, Vol. 44, pp. 2224-2227 (2003).

Kim Y. C., Na J. H., Park J. M., Kim D. H., Lee J. K., and Kim W. T., "Role of nanometer-scale quasicrystals in improving the mechanical behavior of Ti-based bulk metallic glasses," Applied Physics Letters, Vol. 83, pp. 3093-3095 (2003).

Klement J. W., Willens R. H., and Duwez, P. "Non-crystalline structure in solidified gold–silicon alloys," Nature, Vol. 187, pp. 869-870 (1960).

Komanduri, R., Chandrasekaran, N. and Raff, L. M., “Effect of tool geometry in nanometric cutting: a molecular dynamics simulation approach,” Wear, Vol. 219, pp. 84-97 (1998).

Komanduri R., Chandrasekaran N. and Raff L. M., “M.D. simulation of nanometric cutting of single crystal aluminum – effect of crystal orientation and direction of cutting,” Wear, Vol. 242, pp. 60-88 (2000).

References

Kui H. W., Greer A. L., and Turnbull D., "Formation of bulk metallic glass by fluxing," Applied Physics Letters, Vol. 45, p. 615 (1984).

Kumar G., Tang H. X. and Schroers J., “Nanomoulding with amorphous metals,” Nature, Vol. 457, pp. 868–872 (2009).

Lee W. B., To S. and Cheung C. F., “Effect of crystallographic orientation in diamond turning of copper single crystal,” Scripta Materialia, Vol. 42, no. 10, pp. 77-87 (2000).

Lee W. B. and Zhou M., “A theoretical analysis of the effect ofcrystallographic orientation on chip formation inmicromachining,” Internatinal Journal of Machine Tools and Manufacture, Vol. 33, pp. 39–447(1993).

Lewandowski J. and Greer A., “Temperature rise at shear bands in metallic glasses,” Nature Materials, Vol. 5, pp.15-18 (2006).

Liang Y., Moronuki N., and Furakawa Y., “Calculations of the effect of matrial anisotropy on microcutting processes,” Precision Engineering, Vol. 16, no. 2, pp. 132-138 (1994).

Li H., Subhash G., Gao X. L., Kecskes L. J. and Dowding R. J., “Negative strain rate senitivity and compoditional dependence of fracture strength in Zr/Hf based bulk metallic glasses, ” Scripta. Materialia, Vol. 49, pp. 1087-1092 (2003).

References

Li S., Zhao D. Q., Pan M. X., and Wang W. H., "A bulk metallic glass based on heavy rare earth gadolinium," Journal of Non-Crystalline Solids, Vol. 351, pp. 2568-2571 (2005).

Liu L. F., Dai L. H., Bai Y. L., Wei B. C. and Eckert J., "Behavior of multiple shear bands in Zr-based bulk metallic glass," Materials Chemistry and Physics, Vol. 93, pp. 174-177 (2005).

Liu L. F., Dai L. H., Bai Y. L. and Wei B. C., "Initiation and propagation of shear bands in Zr-based bulk metallic glass under quasi-static and dynamic shear loading," Journal of Non-Crystalline Solids, Vol. 351, pp. 3259-3270 (2005).

Liu K. and Melkote S. N., "A strain gradient based finite element model for micro/meso-scale orthogonal cutting process," Proceedings of 2004 Japan-USA Symposium on Flexible Automation, Denver, Colorado (2004).

Lu J., Ravichandran G. and Johnson W. L., "Deformation behavior of $Zr_{41.2}Ti_{13.8}Cu1_{2.5}Ni_{10}Be_{22.}$bulk metallic glass over a wide range of strain-rates and temperatures," Acta Materialla, Vol. 51, pp. 3429-3443 (2003).

Nakasuji T., Kodera S., Matsunaga H., Ikawa N. and Shimada S., "Diamond turning of brittle materials for optical components," Annals of the CIRP – Manufacturing Technology, Vol. 39, pp. 89-92 (1990).

References

Mahnama M. and Movahhedy M. R., “Prediction of machining chatter based on FEM simulation of chip formation under dynamic conditions,” International Journal of Machine Tools and Manufacture, Vol. 50, pp. 611–620 (2010).

Martienssen W. and Warlimont H., Springer Handbook of Condensed Matter and Materials Data, Springer (2005).

Marusich T. D. and Ortiz M., “Modelling and simulation of high speed machining,” International Journal of Numerical Methods in Engineering, Vol. 38, pp. 3675-3694 (1995).

Merchant M. E., “Mechanics of the metal cutting process. I: orthogonal cutting and a type 2 chip,” Journal of Applied Physics, Vol. 16, p.267-275 (1945).

Mitsui K., Sato H. and Takenaka N., “Frequency characteristic of cutting process identified by an in-process measurement of surface roughness,” Annals of the CIRP, pp.67-71 (1978).

Moriwak T. I. and Okuda K., “Machinability of copper in ultra-precision micro diamond cutting,” Annals of the CIRP – Manufacturing Technology, Vol. 38, pp. 115-118 (1989).

Muhammad A., Zhang X., Mustafizur R. and Senthil K., “A predictive model of the critical underformed chip thickness for ductile-brittle transition in nano-machining of brittle material,” International Joural of Machine Tools and Manufacture, Vol.64, pp. 114-122 (2013).

Nieh T. G. and Wadsworth J., “Homogeneous deformation of bulk metallic glasses”, Scripta Materialia, Vol. 54, pp. 387–392 (2006).

Okuda, K., Tanaka, T. and Nunobiki, M. “107 Study on surface integrity of magnesium alloys in ultra-precision diamond cutting,” Proceedings of International Conference on Leading Edge Manufacturing in 21st century : LEM21, pp.33-38 (2003).

Özel T., “The influence of friction models on finite element simulations of machining,” International Journal of Machine Tools and Manufacture, Vol. 46, pp. 518–530 (2006).

Peker A. and Johnson W. L., "A highly processable metallic-glass - Zr41.2Ti13.8Cu12.5Ni10.0Be22.5," Applied Physics Letters, Vol. 63, pp. 2342-2344 (1993).

Rakotomolala R., Joyot P. and Touratier M., “Arbitrary Lagrangian-Eulerian thermomechanical finite-element model of material cutting,” Communications in Numerical Methods in Engineering, Vol. 9, pp. 975-987 (1993).

References

Recht R. F., “A dynamic analysis of high speed machining,” ASME Jounal of Engineering for Industry, Vol. 107, pp. 309-315 (1985).

Recht R. F., “Catastrophic thermoplastic shear”, Journal of Applied Mechanics, pp. 189-193 (1964).

Sato M., Kato K. and Tuchiya K., “Effect of material and anisotropy upon the cutting mechanism,” Transaction of the Japan Institute of Metals, vol. 9, pp.530-536 (1978).

Shaw M. C., Metal cutting principles, 3rd edition, MIT Press, Cambridge, MA (1954).

Sekhon G. S. and Chenot S., “Numerical simulation of continuous chip formation during non-steady orthogonal cutting,” Engineering Computations, Vol. 10, pp. 31-48 (1993).

Shirakashi T. and Usui E., “Simulation analysis of orthogonal metal cutting process,” Journal of the Japan Society for Precision Engineering, Vol. 42, pp. 340-345 (1976).

Shen T. D., Harms U., and Schwarz R. B., "Bulk Fe-based metallic glass with extremely soft ferromagnetic properties," Materials Science Forum, Vol. 386-388, pp. 441-446 (2002).

Shi, J. and Liu, C. R., “The influence of material models on finite element simulation of machining,” ASME Journal of Manufacturing Science and Engineering, Vol. 126, pp.849-857 (2004).

References

Silva M. B. da and Wallbank J., "Cutting temperature: prediction and measurement methods—a review," Materials processing technology, Vol.88, pp.195-202 (1999).

Spaepen F., "A microscopic mechanism for steady state inhomogeneous 5ow in metallic glasses," Acta Materialia, Vol. 25, pp.407–415 (1977).

Sugano T. and Takeuchi K., "Diamond turning of an aluminum alloy for mirror," Annals of the CIRP – Manufacturing Technology, Vol. 36, pp. 7-20 (1987).

Sze Y. K., "The effect of preferred orientation in the single point diamond turning of polycrystalline materials", M. Phil. Thesis, The Hong Kong Polytechic University (2006).

Tai T. P., Yang Y. C., Hwong Y. C. and Ku C. H., "A new concept of cutting marks formation in metal cutting vibration,"Proceedings of 20th International Machine Tool Designs and Research Conference, London: The Macmillan Press Ltd, pp. 449-456 (1980).

Trent M. and Wright P. K., Metal cutting, Fourth edition, Butterworth-Heineman (2000).

Tang C., Yi J., Xu W. and Ferry M., "Temperature rise in shear bands in a simulated metallic glass," Physical Review B, Vol. 98, pp. 224203-224208 (2018).

Taniguchi N., "Current status in, and fure trends of, ultraprecision machining and ultrafine materials processing," Annals of CIRP, Vol. 32, pp. 573-603 (1983).

Thurnheer P., Haag F.and Löffler J.F., “Time-resolved measurement of shear-band temperature during serrated flow in a Zr-based metallic glass,” Acta Materialia, Vol. 115, pp.468-474 (2016).

Toropov A. and Ko S. L., “Prediction of tool-chip contact length using a new slip-line solution for orthogonal cutting,” International Journal of Machine Tools & Manufacture, Vol. 43, pp. 1209-1215 (2003).

To S., Lee W. B., Chan C. Y., “Ultraprecision diamond turningof aluminium single crystals,” Journal of Material Processing Technology, Vol. 63, pp. 157–162 (1997).

Tresoff, J., “New empirical model for the structural properties of silicon,” Physical Review Letters, Vol. 56, pp. 632-635 (1986).

Ueda K. and Manabe K., “Chip formation mechanism in microcutting of an amorphous metal,” Annals of the CIRP, Vol.41, no.1, pp.129-132 (1992).

Ueda N., Matsuo T. and Hoshi T., “An investigation of some shear angle theories,” Annals of the CIRP, Vol. 35, pp.27-30 (1986).

Vaillant M. L., Keryvin V., Rouxel T. and Kawamura Y., “Changes in the mechanical properties of a Zr55Cu30Al10Ni5 bulk metallic glass due to heat treatments below 540 C,” Scripta Materialia, Vol. 47, pp.19-23(2002).

References

Vijay Sekar K. S. and Pradeep Kumar M., “Finite element simulations of Ti6Al4V titanium alloy machining to assess material model parameters of the Johnson-Cook constitutive equation,”. Journal of the Brazilian Society of Mechanical Sciences and Engineering,” Vol.33, pp.203-211 (2011).

Wang C., Ding F., Tang D., Zheng L., Li S. and Xie Y., “Modeling and simulation of the high-speed milling of hardened steel SKD11 (62 HRC) based on SHPB technology,” International Journal of Machine Tools and Manufacture, Vol. 108, pp. 13–26 (2016).

Wang H., To S., Chan C.Y., Cheung C.F. and Lee W.B., “A study of regularly spacing shear bands and morphology of serrated chipfprmation in microcutting process, ” Scripta. Materialia, Vol. 63, pp. 227-230 (2010).

Wang. H., To S., Chan C.Y., Cheung C.F. and Lee W.B., “Elastic strain induced shear bands in the microcutting process”, International Journal of Machine Tools & Manufacture, Vol.50, pp. 9-18 (2010).

Wang W. H., Wang Z. X., Zhao D. Q., Pan M. X., Okada T., and Utsumi W., "Formation and crystallization of CuZrHfTi bulk metallic glass under ambient and high pressures," Journal of Physics-Condensed Matter, Vol. 15, pp. 5923-5932 (2003).

Warburg E., "Magnetische Untersuchungen," Annalen der Physik, Vol. 249, pp. 141-164 (1881).

References

Xie H., Lin J., Li Y., Yan W., Hodgson P. and Wen C., “Plastic deformation in $Zr_{41}Ti_{14}Cu_{12.5}Ni_{10}Be_{22.5}$ bulk metallic glass under Vickers indentation, ” Journal of Alloys and Compounds, Vol. 461, 173-177 (2008).

Yin W., “Compressive behavior of bulk metallic glass under different conditions — Coupled effect of temperature and strain rate”, PhD Thesis, The University of North Carolina at Charlotte (2013).

Yi S., Park T. G., and Kim D. H., "Ni-based bulk amorphous alloys in the Ni-Ti-Zr-(Si,Sn) system," Journal of Materials Research, Vol. 15, pp. 2425-2430 (2000a).

Yi S., Park T. G., and Kim D. H., "Development of new Ni-based amorphous alloys containing no metalloid that have large undercooled liquid regions," Scripta Materialia, Vol. 43, pp. 109-114 (2000b).

Yu P., Guo S.F. and Wang J.F., “The structural evolution and mechanical properties of a Zrbased bulk metallic glass during superplastic gas pressure forming,” Materials & Design, Vol. 37, pp. 510–514 (2012).

Zhang S.J., To S., Wang S.J., Zhu Z.W., “A review of surface roughness generation in ultra-precision machining,” International Journal of Machine Tools and Manufacture, Vol. 91, pp. 76–95 (2015).

References

Zhang T., Inoue A., and Masumoto T., "Amorphous Zr-Al-Tm (Tm = Co, Ni, Cu) Alloys with Significant Supercooled Liquid Region of over 100-K," Materials Transactions, Vol. 32, pp. 1005-1010 (1991).

Zhu J., Kim H. J. and Kapoor S. G., "Microscale drilling of bulk metallic glass," Journal of Micro and Nano-Manufacturing, Vol. 1, pp. 041004 (2013).

Zhu P. Z., Qiu C., Fang F. Z. Yuan D. D and Shen X. C., "Molecular dynamics simulations of nanometric cutting mechanisms of amorphous alloy," Applied Surface Science, Vol. 317, pp. 432–442 (2014).

Zienkiewicz, O. C., The Finite Element Method in Engineering Science, 2nd ed., London: McGraw-Hill (1971).